Influence of the surface composition and morphology on the reflectivity of diagnostic mirrors in a fusion reactor

Maria Matveeva

Member of the Helmholtz Association

Energie & Umwelt / Energy & Environment
Band / Volume 261
ISBN 978-3-95806-051-7

JÜLICH FORSCHUNGSZENTRUM

Schriften des Forschungszentrums Jülich
Reihe Energie & Umwelt / Energy & Environment Band / Volume 261

Forschungszentrum Jülich GmbH
Institute of Energy and Climate Research
Plasma Physics IEK-4

Influence of the surface composition and morphology on the reflectivity of diagnostic mirrors in a fusion reactor

Maria Matveeva

Schriften des Forschungszentrums Jülich
Reihe Energie & Umwelt / Energy & Environment Band / Volume 261

ISSN 1866-1793 ISBN 978-3-95806-051-7

Bibliographic information published by the Deutsche Nationalbibliothek.
The Deutsche Nationalbibliothek lists this publication in the Deutsche
Nationalbibliografie; detailed bibliographic data are available in the
Internet at http://dnb.d-nb.de.

Publisher and Distributor: Forschungszentrum Jülich GmbH
Zentralbibliothek
52425 Jülich
Tel: +49 2461 61-5368
Fax: +49 2461 61-6103
Email: zb-publikation@fz-juelich.de
www.fz-juelich.de/zb

Cover Design: Grafische Medien, Forschungszentrum Jülich GmbH

Printer: Grafische Medien, Forschungszentrum Jülich GmbH

Schriften des Forschungszentrums Jülich
Reihe Energie & Umwelt / Energy & Environment, Band / Volume 261

D 61 (Diss. Düsseldorf, Univ., 2014)

ISSN 1866-1793
ISBN 978-3-95806-051-7

The complete volume is freely available on the Internet on the Jülicher Open Access Server (JuSER)
at www.fz-juelich.de/zb/openaccess.

Table of contents

Kurzfassung

Für den erfolgreichen Betrieb von Fusionsexperimenten und zukünftigen Fusionsreaktoren ist der Einsatz von Diagnostiken für die Kontrolle des Fusionsplasmas unabdingbar. Diese Diagnostiken messen die Lichttransmissivität des Plasmas und benötigen metallische Spiegel. Für die Entwicklung und den erfolgreichen Betrieb dieser Spiegel muss die Wechselwirkung des Plasmas mit deren Oberflächen untersucht und verstanden werden.

In dieser Arbeit wird der Einfluss des Plasmas auf diese metallische Spiegel untersucht. Plasmaexposition der Spiegel führt zu einer Änderung der Morphologie und Zusammensetzung der Oberfläche. Um diese Effekte zu bestimmen werden in dieser Arbeit eine Reihe von Experimenten in den beiden Tokamakexperimenten TEXTOR und DIII-D durchgeführt. Vorcharakterisierte metallische Spiegel werden während der Plasmaoperation (TEXTOR) und während der thermo-oxidativen Wandkonditionierung (DIII-D) exponiert. Die Spiegelproben werden *post-mortem* mittels Oberflächen- und optischen Analysetechniken charakterisiert. Um die beobachteten Oberflächenänderungen zu verstehen, werden die Wechselwirkungen von Ionen und Oberflächen mit SDTrimSP simuliert. Die für die Modifikationen der Oberflächenmorphologie unter dem Beschuss von hochenergetischen Teilchen verantwortlichen Prozesse, wie z.B. die Oberflächenerosion und die Schichtbildung, werden untersucht.

Die Messungen zeigen, dass die gerichtete Reflektivität der Spiegel sehr stark von der Oberflächenrauigkeit abhängt. Die Rauigkeit nach der Plasmaexposition wiederum ist abhängig von der kristallinen Struktur des Materials, da Körner mit unterschiedlicher kristalliner Orientierung unterschiedliche Zerstäubungsraten aufweisen. Eine Vergrößerung der Oberflächenrauigkeit resultiert aus der inhomogenen Zerstäubung eines polykristallinen Materials und führt zu einem signifikanten Abfall der gerichteten Reflektivität aufgrund von diffuser Beugung des einfallenden Lichtes. Unter Nettoerosionsbedingungen zeigen Spiegelbeschichtungen mit Kristalliten im Nanometerbereich ein ähnliches Verhalten wie polykristalline Materialien, während Einkristallspiegel eine signifikant geringere Aufrauung bedingt durch die einheitliche Zerstäubungsrate aufweisen und somit deren Reflektivität besser erhalten bleibt.

Die Spiegelreflektivität ist auch von der Oberflächenzusammensetzung abhängig, welche durch Plasma-Wand-Wechselwirkungen verändert werden kann. Die Dicke der betroffenen Oberflächenschicht ist bedingt durch das Gleichgewicht zwischen Erosion, Deposition, Teilchenimplantation, Diffusion und chemischen Reaktionen. Zum Beispiel ist auf Spiegeln, die in TEXTOR exponiert wurden, Carbidbildung zu beobachten, welche zu einer Reduktion der Oberflächenreflektivität führt. Die resultierende Tiefenverteilung der Kohlenstoffatome ist unabhängig von der Spiegeltemperatur und deutet auf eine sehr langsame Volumendiffusion des Kohlenstoffs hin. Somit kann die Volumendiffusion auf der Zeitskala des Experimentes vernachlässigt werden, wenn man die Diffusionstiefen mit den Ionenimplantationstiefen oder der Dicke der erodierten Schicht vergleicht. Die Bildung von Carbiden und Oxiden verlangsamt die Volumendiffusion und verhindert somit ein tieferes Eindringen von Fremdatomen in die Oberfläche. Die Ergebnisse von Messungen und Simulationen deuten stark auf ein dynamisches Gleichgewicht zwischen physikalischen und chemischen Prozessen hin. Das Gleichgewicht resultiert in ähnlich dicken Carbid-Schichten auf allen Molybdän-Spiegeln, unabhängig von der auftreffenden Teilchenfluenz und Probentemperatur.

Das Gleichgewicht zwischen Erosions- und Depositionsprozessen auf der Spiegeloberfläche ist stark von den Plasmaparametern abhängig. Nettoerosionsbedingungen sind für metallische Spiegel von Vorteil, da diese nicht zum Wachstum undefinierter Schichten führen. In dieser Arbeit wird gezeigt, dass das Gleichgewicht zwischen Erosion und Deposition zu einer Nettoerosion durch gezielten Gaseinlass nahe der Spiegeloberfläche während der Plasmaexposition verschoben werden kann.

Diese Arbeit erweitert das aktuell gültige Verständnis der Plasma-Wand-Wechselwirkungsprozesse auf die Reflektivität von metallischen, plasmaexponierten Spiegeln. Die Resultate dieser Arbeit wurden für große Fusionsexperimente, wie z.B. ITER, extrapoliert. Um optimale Betriebsbedingungen für diagnostische Spiegel in Fusionsexperimenten und in -reaktoren zu erreichen und zu erhalten, sollten die Spiegel unter Nettoerosionsbedingungen betrieben werden. Da Nettoerosionsbedingungen nicht garantiert werden können, sollten zudem Methoden zur Depositionsreduktion entwickelt und Möglichkeiten für die *in-situ* Spiegelreinigung und für Kalibrationsmessungen bereitgestellt werden.

Abstract

Plasma-surface interactions in fusion devices represent a critical issue for the design and operation of diagnostic systems based on transmission of light signals from plasma where metallic mirrors will be used as first plasma-viewing elements.

In this work, the behavior of metallic mirrors is investigated with respect to the influence of plasma-induced changes of surface morphology and composition on the surface reflectivity. The work is based on the series of dedicated experiments performed in tokamaks TEXTOR and DIII-D, in which pre-characterized metallic mirrors were exposed during the plasma operation (TEXTOR) and during the thermo-oxidative wall conditioning (DIII-D). The morphology, composition and optical properties of the mirror surfaces are analyzed *post-mortem*. To understand the observed surface modifications, ion-surface interactions are modelled with the SDTrimSP code. The processes responsible for modifications of the surface morphology and composition under energetic particles bombardment, the surface erosion and formation of deposited layers, are investigated.

Measurements show that the specular reflectivity of a mirror strongly depends on the surface roughness. The surface roughness after a plasma exposure depends on the crystalline structure of the material due to the fact that grains with different crystalline orientations have different sputtering rates. An increase of the surface roughness resulting from non-homogeneous sputtering of a polycrystalline material leads to a significant drop of the specular reflectivity due to diffuse scattering of the incident light. It is shown that under net erosion conditions coatings with nano-sized crystallites demonstrate a similar behaviour compared to polycrystalline materials. On the contrary, single crystalline mirrors are sputtered uniformly, thus show significantly less roughening and preserve the reflectivity better.

The mirror reflectivity depends also on the surface composition, which can be changed due to plasma-surface interactions. The thickness of the affected surface layer depends on the balance between the processes of erosion, deposition, particle implantation, diffusion, and chemical reactions. For instance, carbide formation is observed on mirrors exposed in TEXTOR, thus contributing to the decrease of the surface reflectivity. The independence of the resulting depth distributions of carbon atoms from the mirror temperature suggests that the volume diffusion of carbon is very slow and can be neglected when comparing the diffusion depth with the ion implantation depth or the thickness of the eroded layer within the time scale of the experiment. It is shown that formation of carbides and oxides slows down the volume diffusion and prevents deeper penetration of impurity atoms into the surface. Measurements and modelling give a strong indication of a dynamic equilibrium established between the different physical and chemical processes involved. This equilibrium results in similar thicknesses of carbide layers formed on all molybdenum mirrors independent on the incident particle fluence and sample temperature.

The overall balance between erosion and deposition processes on the mirror surface depends strongly on plasma parameters. Net erosion conditions are beneficial for metallic mirrors since such conditions do not lead to an unpredictable layer growth. It is demonstrated in this work that the balance between erosion and deposition can be shifted towards net erosion by means of intentional injection of gaseous species in the vicinity of the mirror surface during the plasma exposure.

This work extends the current understanding of the influence of plasma-surface interaction processes on the reflectivity properties of metallic mirrors exposed to plasma. The results

presented in this work are analysed and extrapolated with respect to their relevance to large scale fusion devices such as ITER. To allow and maintain the optimal operation of diagnostic mirrors in reactor scale fusion devices, operation of mirrors under net erosion conditions is recommended. Since net erosion conditions cannot be guaranteed, deposition mitigation techniques need to be developed and means for *in-situ* mirror cleaning and calibration measurements have to be provided.

Introduction

Currently available world energy resources are based mostly on fossil fuels. However, it becomes evident that these resources will soon become insufficient to cover constantly growing world energy demands [UN documents]. New energy sources have to be found. Nuclear fusion is one of the promising alternatives offering a clean and safe energy source for the future. However, the controlled thermonuclear fusion reaction represents a very complex scientific and technological task. More than 50 years ago L.A. Artsimovich, the Soviet physicist and academician under whose guidance a thermonuclear fusion reaction was produced in the laboratory for the first time, said the following:

> *"... The solution of the problem of thermonuclear fusion will require a maximum concentration of intellectual effort and the mobilization of very appreciable material facilities and complex apparatus. This problem seems to have been created especially for the purpose of developing close cooperation between the scientists and engineers of various countries"* *

More than 25 years later, in 1985, the joint project ITER was started with an aim to demonstrate the scientific and technological feasibility and economical effectiveness of a controlled thermonuclear reaction for peaceful purposes. Presently, ITER is the world's second largest non-commercial international project after the International Space Station and a continuous effort of scientific and technological research from the European Community, Russia, Japan, the U.S.A, China, and since recently, India and South Korea.
The idea of energy production by nuclear fusion is based on the processes happening in the stellar core. These processes are the fusion of light atomic nuclei and the release of the difference in binding energies of reactants and reaction products in the form of the kinetic energy of particles. Fusion reaction can happen only when two reactant nuclei approach each other to a distance where repulsive electrostatic forces are overcome by nuclear attraction (the distances $\sim 10^{-14}$ m). The nuclear reaction underlying the controlled nuclear fusion feasible on earth is the following:

$$D + T \rightarrow {}^{4}He\ (3.5\ MeV) + n\ (14.1\ MeV). \tag{0.1}$$

The first generation of future fusion reactors will be based on this so-called D-T reaction, because it has the largest cross section at the lowest energy of colliding particles [Wesson 2004]. The cross-section of the D-T reaction is still much smaller than the cross-section of elastic Coulomb collisions between D and T nuclei, therefore the reacting medium has to be confined and heated up to allow frequent collisions and high energies of colliding particles. Ultimately, the produced fusion power output should be sufficiently large to compensate the input power used for heating and control of the reacting medium. These high temperature conditions of the reacting medium correspond to some hundreds millions kelvin, under which the reactants, D and T atoms, exist in the ionized state known as the plasma state of matter. The reaction products of the D-T reaction are an α-particle (helium nucleus) and a neutron. The kinetic energy of neutrons can be converted into heat and then into electricity using

* L. A. Artsimovich, Overview paper for the United Nations Second Conference on the Peaceful Uses of Atomic Energy (1958) [IAEA 1958]

conventional steam technologies. The α-particles, in turn, could deliver their energy to the reacting medium (plasma), thus compensating the energy losses and helping to make the fusion process self-sustaining.

One of the necessary conditions for the use of nuclear fusion as a future energy source for base electricity production is the wide availability of fuel. Deuterium and tritium required for the fusion reaction must be readily available in appropriate quantities. Deuterium is sufficiently contained in sea water. The amount of tritium in nature is scarce, however neutrons appearing as a result of the fusion reaction can be used for *in-situ* tritium production in reactions with lithium, which is widely available in nature.

The fusion plasma has to be confined; otherwise, plasma will expand reaching the surrounding walls, cool down and disappear. The so-called *"fusion triple product"* quantifies the confinement criterion for D-T plasma with the confinement time τ_E, plasma density n_0 and temperature T to achieve a positive energy balance [Wesson 2004]:

$$n_0 \cdot T \cdot \tau_E > 5 \cdot 10^{21}\ keV \cdot s \cdot m^{-3}. \tag{0.2}$$

This minimal required value of the triple product corresponds to plasma densities of the order of 10^{20} m^{-3} and temperatures of about 10 keV.

In magnetic confinement fusion devices a superposition of magnetic fields is used to restrain and control the plasma. Charged particles (ions and electrons) experience the Lorentz force and move helically along the magnetic field lines, thus being confined in the perpendicular to the field line direction. Toroidal geometry provides closed magnetic field lines and prevents parallel losses of particles. In tokamaks, the internal plasma current is produced and is used to generate the helical component of the magnetic field necessary for stable plasma equilibrium (Figure 0.1). This can be contrasted to another toroidal magnetic confinement system, stellarator [Piel 2010], in which the magnetic field is produced entirely by external coils of very complex geometries with a negligible current flowing through the plasma itself. The tokamak concept is presently the most advanced alternative on the way to fusion energy production. Tokamak ITER is designed to reach the ratio of the fusion power produced to the heating power applied, factor Q, equal to 10 and demonstrate the long-pulse operation (~ 400 s) [Mukhovatov 2003].

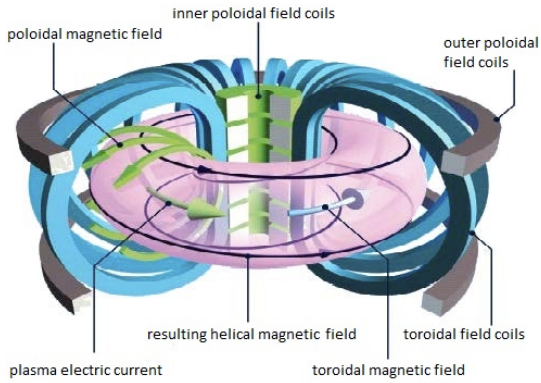

Figure 0.1. Scheme of a tokamak. Curtesy – EFDA [www.efda.org].

Efficient energy and particle exhaust from the plasma is required to extract the produced fusion power, thus implying a certain level of plasma-wall contact. Plasma impact onto a

material surface may lead to various adverse effects with respect to both wall material integrity and plasma performance. In ITER and to even larger extent in future fusion reactors, neutrons produced in fusion reactions will create additional damage in wall materials. Off-normal events (disruptions and vertical displacements) and transients (edge localized modes) increase the intensity of plasma-wall interactions (PWI) tremendously. Therefore, investigations of PWI processes and control of off-normal and transient events represent a hot topic of fusion research.

Irrespectively of the underlying concept, future fusion reactors will require a set of diagnostic tools to monitor and control the plasma. Many of diagnostic setups are sensitive to the harsh plasma environment and therefore have to be protected from electromagnetic radiation, as well as particle fluxes from plasma. In particular, optical and laser diagnostics will use metallic mirrors to guide the light from plasma to the measuring equipment located farther away. The very first mirrors of such diagnostics will be installed in the line-of-sight with plasma. Degradation of the mirror surface due to energetic particle bombardment from plasma may affect the reliability of the transmitted signals measured by diagnostics. In this context, studies of the performance of metallic mirrors in a fusion reactor are of significant importance.

The understanding of physical and chemical processes taking place in the case of metallic mirrors exposed to plasma and the knowledge on how these processes influence the mirror performance are essential and highly required in order to find possible methods of preserving optical properties of mirrors installed in a diagnostic duct of a fusion reactor. Gaining the corresponding knowledge and understanding represents the goal of the work presented in this thesis.

In this thesis metallic mirrors are investigated experimentally in tokamaks TEXTOR and DIII-D with respect to their performance under conditions of material erosion and deposition. Corresponding modifications of composition and structure of the mirror surface are investigated by means of different surface analysis techniques and modelling and related to the changes of reflectivity properties of mirrors.

Earlier investigations demonstrated that materials with an ordered structure are the best candidates for mirrors under erosion conditions since they are sputtered uniformly. Experiments confirm that single crystal (SC) molybdenum mirrors and mirrors coated by films with small crystallite structure demonstrate significantly better resistance to the impact of the environment of modern fusion devices in comparison to polycrystalline (PC) mirrors [Konovalov 2001, Litnovsky 2007b]. In this thesis, single crystal (SC) mirrors and mirrors with nano-structured coatings of different materials are investigated under erosion conditions in different tokamaks. Simulations with the SDTrimSP code are applied to interpret the experimental observations.

Deposition of impurities on the mirrors surface is known to affect the mirror reflectivity significantly. In this thesis, the possibility of mitigation of impurity deposition by means of gas feeding in the vicinity of mirrors is examined. Gas injection experiments performed in the scrape-off layer (SOL) plasma of the TEXTOR tokamak a presented. A stationary 1-D model of the SOL plasma is used to simulate the physical processes caused by the gas injection [Marchuk 2007].

Wall conditioning is used in fusion devices to achieve a better PWI control. Due to radioactivity of tritium, its accumulation inside the reactor must be limited for safety reasons. De-tritiation is thus required to release the tritium fuel that will be accumulated in the walls of a reactor device during plasma operation. Thermo-oxidative wall conditioning is considered as one of possible techniques for the de-tritiation of in-vessel components. This method implies baking of the vacuum vessel in an oxygen-containing atmosphere at elevated temperatures [Davis 2009]. Degradation of diagnostic mirrors during such conditioning procedure represents a concern. In the frame of this thesis, the effect of thermo-oxidation on

mirrors made from different materials is addressed in the experimental study performed in the DIII-D tokamak.

The thesis is structured as follows:

- In chapter 1 some details about plasma-wall interaction processes in fusion devices are given followed by a brief description of physical and engineering requirements for diagnostic mirrors in a fusion reactor.
- In chapter 2, the definition of the mirror reflectivity and the basics of light reflection from metals are given.
- Chapter 3 focuses on physical processes affecting properties of mirrors exposed to plasma; in particular, the optical reflectivity of metallic mirrors is addressed.
- Chapter 4 summarizes different surface characterization techniques, which were used in this work for analysis of mirror properties.
- In chapter 5 the setup and conditions of experiments in tokamaks TEXTOR and DIII-D are described. Here also main experimental results are presented that include optical observations, microscopy and surface composition measurements, as well as reflectivity measurements on exposed mirrors.
- Chapter 6 is dedicated to the detailed analysis of the mirror performance under tokamak conditions. Exposure conditions are quantified based on plasma parameter measurements in each particular experiment. Plasma induced surface modification is addressed with respect to exposure under erosion dominated conditions, gas injection as a deposition mitigation technique and wall-conditioning in oxygen atmosphere. Conclusions based on the observed mirror performance are supported with additional measurements and modelling.
- Chapter 7 summarizes the results of analysis presented in chapter 6 with respect to the physical processes involved and their influence on reflectivity properties of metallic mirrors.
- In chapter 8 conclusions and recommendations towards high performance operation of first mirrors in ITER are given.

Chapter 1. Diagnostic mirrors for a fusion reactor

1.1 Plasma-wall interactions in tokamaks

The problem of plasma-wall interactions remains one of the most critical topics of the present fusion research [Samm 2005]. Plasma confinement is not perfect and particles are continuously expelled from the confined region to the walls of the reactor vessel. Efficient energy and particle exhaust from the plasma is required to extract the produced fusion power; however it also imposes serious constraints on the choice and engineering design of plasma-facing materials and components (PFCs) with respect to their lifetime, thermal, electrical and mechanical properties. Plasma impact onto a material surface may lead to mechanical damage of wall components due to erosion, melting and evaporation processes, as well as to plasma contamination due to impurity production. Released impurities returning to a surface lead to further degradation of material properties due to formation of deposited layers and material mixing effects, alloying and other processes. In ITER and to even larger extent in future fusion reactors, neutrons produced in fusion reactions will create additional damage in wall materials.

The standard approach to protect the main wall of the device from plasma is to limit the plasma contact to specially designed wall elements. Ions moving along field lines diffuse radially outwards and finally reach the last closed magnetic flux surface (LCFS), i.e. the magnetic flux surface that touches the limiting surface protruding into the plasma the most. In the region between the LCFS and the main wall, in the so-called scrape-off layer (SOL), magnetic field lines are open, i.e. they end at the limiting surfaces. Particles that enter the SOL continue their motion along the field lines and reach one of the limiting surfaces. The LCFS can be defined either by inserting solid wall elements into plasma (limiter configuration, Figure 1.1a) or applying special magnetic field configurations acting to divert the plasma (divertor configuration, Figure 1.1b). In the divertor configuration, solid surfaces in contact with plasma (target plates) are moved away from the LCFS so that plasma-surface interactions take place farther away from the plasma core, which is beneficial for impurity screening. In addition, closed divertor configuration favours better exhaust control and allows operating the device in the so-called high confinement mode (H-mode) characterized by reduced radial transport of plasma towards the wall.

ITER will be a divertor machine. It was designed to use the initial material mix of beryllium (Be), tungsten (W) and carbon fibre composite (CFC) for plasma-facing components and switch to carbon-free configuration using tungsten divertor target plates in the D-T phase of operation to avoid strong tritium co-deposition with carbon. However, at present the possibility of skipping the first carbon divertor and starting with full-W divertor and Be first wall already in the initial phase of ITER operation is discussed. The behaviour of such a material combination under tokamak environment is still an open issue, which is being extensively studied in the JET tokamak in the frame of the ITER-Like Wall (ILW) project

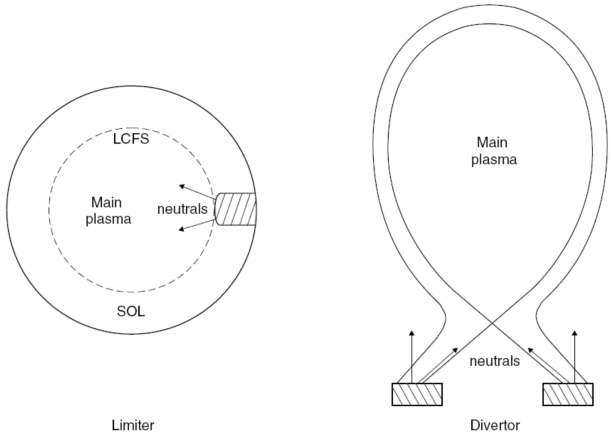

Figure 1.1. Limiter (a) and divertor (b) configuration in a tokamak [Stangeby 2000]

1.2 Diagnostic mirrors in ITER

ITER will be an experimental machine that is expected to provide reactor relevant burning plasma environment and better understanding of physical processes involved. Therefore there is an acute need in extensive diagnostics of plasma and related fusion products to control and understand the plasma performance [Costley 2001]. The ITER design relies on a solid basis of experimental results and sophisticated modelling. However, there are still a number of issues for which the experimental database is less robust or which are critical on the basis of extrapolation from present day fusion devices. In particular, the design of diagnostics for ITER has to be compatible with the harsh environment caused by the long pulse operation and the high levels of neutron production [ITER 1999]. Because of severe neutron environment, all the optical and laser diagnostic systems of ITER will have to use optical periscope-like systems to transfer the signals from plasma beyond the neutron shielding (Figure 1.2). Such diagnostics account for approximately one half of the total number of foreseen diagnostics in ITER and will have to use metallic mirrors as their first plasma-viewing optical elements, which is due to high levels of radiation from plasma leading to inadmissible absorption and radiation-induced luminescence in refractive light-guiding components (e.g. windows). These mirrors, in turn, will be also subjected to high fluxes of charged and neutral particles originating from plasma, high levels of electromagnetic radiation, intensive neutron fluxes. As a result, the surface of metallic mirrors will suffer erosion and/or deposition, particle implantation and other adverse effects, which will change their optical and polarization characteristics, affecting the entire performance of the respective diagnostic systems and possibly leading to their shutdown [ITER ITA 2006].

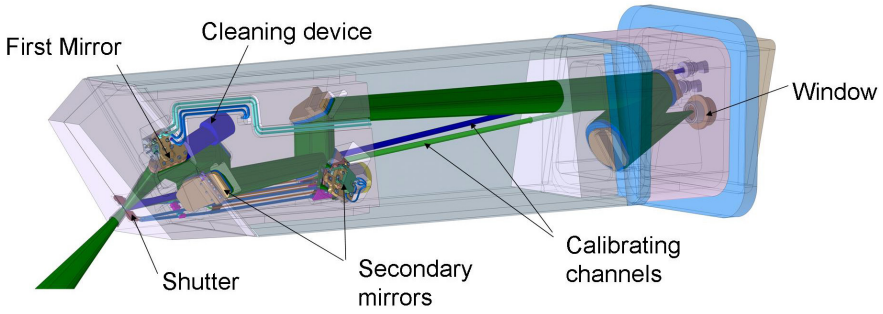

Figure 1.2. An example of an optical diagnostic system: core charge exchange resonance spectroscopy (cCXRS) observation system with mirrors, optical paths and port plug components (cCXRS reference design) [Krasikov 2012].

The performance of first diagnostic mirrors, i.e. mirrors placed in the direct line-of-sight with plasma, has been studied in various plasma devices since several years, and such investigations are still ongoing. Experiments with diagnostic mirrors performed in tokamaks TEXTOR [Wienhold 2005], JET [Rubel 2010], T-10 [Vukolov 2004], DIII-D [Litnovsky 2008] and Tore Supra [Lipa 2006, Gil 2007], as well as in the LHD stellarator [Voitsenya 2005] demonstrated that the behaviour of first diagnostic mirrors depends on their position within the vacuum vessel. It turned out that mirrors placed in the divertor region (LHD), close to the graphite limiter (T-10), in the scrape-off layer (SOL) plasma (TEXTOR), along the outer wall (JET), and in diagnostic ducts (JET, LHD and T-10) were coated with deposited layers formed by materials eroded from the walls, mainly carbon [Litnovsky 2007a]. Only mirrors located close to plasma and fully open to fluxes of charge exchange atoms (CXA) and ions during the glow discharge cleaning (GDC) (LHD and Tore Supra) were clean, but damaged by bombarding particles. These results indicate that erosion of mirrors may be predominant at the inner, high-field side of the vacuum vessel, while deposition of atoms of different origins prevails elsewhere: in ports, near limiters and, in case of divertor machines, in the divertor. Due to significant differences in conditions (e.g. particle fluxes and exposure times) compared to ITER, these experiments cannot be used for direct extrapolation of experimental results towards ITER. Moreover, the performance of mirrors in ITER will depend not only on their position within the vacuum vessel, but also on the surrounding wall materials, vacuum quality, as well as size, geometry and other parameters of diagnostic ducts.
The optical diagnostic systems in ITER will work in a very wide wavelength range from 2.3 nm (the Main Plasma Impurity Monitor) up to about 100 μm (the Polarimeter System). About 80% of first mirrors will have to transfer the light with wavelengths of 250 – 2500 nm [Sugie 2007]. The size of mirrors also varies significantly: e.g., the Polarimeter system will use retroreflectors with mirror diameter 3.7 cm; the Core Thompson Scattering (CTS) diagnostics will need circular mirrors 35 cm in diameter; and the Main Plasma Impurity Monitor will require a 60 cm x 2 cm cylindrical mirror.
Experiments [Rubel 2009, Litnovsky 2009] and modelling [Kotov 2011b] indicate that mirrors positioned with a large view angle to plasma are likely to be under erosion conditions. Mirrors installed inside diagnostic ducts will be protected from direct plasma exposure and may suffer from net impurity deposition, as well as mirrors in the divertor where much higher impurity fluxes have to be expected. B2-EIRENE simulations [Kotov 2011b, Behrisch 2003] demonstrate that the D(T) incident fluxes up to 10^{20} $m^{-2}s^{-1}$ can be expected at the outer midplane wall of ITER. For mirrors protected from the direct plasma impact, CXA will contribute the most to erosion. The CXA fluxes to first mirrors in ITER are estimated to

be ~10^{17} $m^{-2}s^{-1}$ for mirrors in diagnostic blocks of the first wall and 10^{17} - 10^{19} $m^{-2}s^{-1}$ for mirrors in divertor cassettes [Costley 2001]. Due to plasma cooling near upper ports where gas inlets for core fueling are located, gross wall erosion is expected to have its minimum there [Kotov 2011b]. Correspondingly, gross erosion of mirrors placed at the entrance to the upper port should be about 500 times reduced compared to mirrors in equatorial ports.

Due to the broad energy distribution of CXA having energies from few eV up to several keV, their interaction with materials cannot be adequately simulated in experiments using mono-energetic ion beams only. Since most of CXA will have energies of few tens to few hundreds of eV [Behrisch 2003], experiments in tokamak plasmas with Maxwellian type ion energy distributions appear to be essentially more relevant. For instance, typical ion impact energies onto test limiters in tokamak TEXTOR are about 150 - 250 eV for plasma ions and 300 - 500 eV for impurity species such as carbon, boron and oxygen.

Chapter 2. Optical properties of metallic mirrors

In this chapter optical properties of metallic mirrors are introduced and definition of the mirror reflectivity is given. A brief overview of classical optics and light reflection from metals describes the physics necessary for understanding of the mirror properties and measuring techniques addressed in the thesis.

2.1 Light reflection in geometrical optics

In physical optics light is represented by an electromagnetic wave and its interaction with condensed matter is understood as the interaction between the electric field of the wave and electrons in the material. Geometrical optics represents a very good approximation for the propagation of light of a wavelength much smaller than the size of structures with which the light interacts. This approximation, however, fails to account for such effects as light interference and diffraction. In geometrical optics the abstraction of light rays is used to describe how the light propagates in a medium characterized by the refractive index n defined as the ratio of the phase velocity of light in vacuum to the phase velocity of light in the medium. Light rays follow rectilinear paths in homogeneous media and can bend or split at an interface between two media (Figure 2.1). By the specular reflection law, the reflection angle θ_R is equal to the angle of incidence θ_i. The reflectivity R of the medium is defined as the ratio of intensities of reflected and incident rays. For several stacked material layers, i.e. deposited layers on the mirror surface, reflection and refraction take place at all interfaces between each two media and for light propagation in both directions. The total reflected and transmitted signals represent therefore a superposition of multiple light rays that travelled different distances through the media. It has to be noted that in the case of non-ideal surfaces part of the light is diffusely reflected, i.e. scattered in all directions. Specular and diffuse reflectivities will be addressed in more detail in section 2.3.

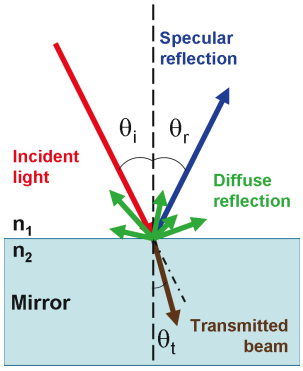

Figure 2.1. Behaviour of light at an interface between two media with refractive indices n_1 and n_2. Symbols θ_i, θ_r, and θ_t indicate the angles of incidence, specular reflection and transmission correspondingly.

2.2 Interaction of electromagnetic waves with medium

For a monochromatic electromagnetic wave of an angular frequency ω incident on a homogeneous isotropic medium characterized by a dielectric constant ε, permeability μ and conductivity σ, the electric field E in the medium satisfies the wave equation (2.1) that can be derived from Maxwell equations [Born&Wolf]:

$$\nabla^2 E + \hat{k}^2 E = 0, \tag{2.1}$$

where the wave number $\hat{k}$ is defined as

$$\hat{k}^2 = \mu\omega^2\hat{\varepsilon}, \tag{2.2}$$

where the complex dielectric constant $\hat{\varepsilon}$ is introduced:

$$\hat{\varepsilon} = \varepsilon + i\frac{\sigma}{\omega}. \tag{2.3}$$

Equations (2.1) and (2.2) are valid for both non-conducting and conducting media. The phase velocity $\hat{v}$ and the refractive index $\hat{n}$ are, in general, complex and can be defined in both cases as

$$\hat{v} = \frac{c}{\sqrt{\mu\hat{\varepsilon}}}, \qquad \hat{n} = \frac{c}{\hat{v}} = \frac{c}{\omega}\hat{k}. \tag{2.4}$$

For a non-conducting medium, the response to an external electromagnetic field is determined by the behaviour of electrons in the valence band. Since $\sigma = 0$, $\hat{\varepsilon}$ is represented by the standard material dielectric constant ε, and the wave number $\hat{k}$ is, to a good approximation, also real, except for frequencies that are close to a resonance [Born&Wolf].
In the case of a conducting medium, the conduction band electrons are not bound to the atoms and are free to move in an external electromagnetic field, leading to attenuation of the wave as it propagates through the medium. Both $\hat{\varepsilon}$ and $\hat{k}$ are complex. The complex refractive index $\hat{n}$ is usually written as follows:

$$\hat{n} = n + i\kappa, \tag{2.5}$$

where *n*, the real part, is responsible for the light refraction thus indicating the phase velocity of the light in the medium, and κ, the imaginary part called the extinction coefficient, defines the light absorption. This can be seen from the solution of equation (2.1) which is a plane, time-harmonic wave with the electric field strength and intensity expressed as follows:

$$\begin{aligned} E &= E_0 e^{-\frac{\alpha x}{2}} e^{i(kx-\omega t)}, \\ I &= I_0 e^{-\alpha x}, \end{aligned} \tag{2.6}$$

where the real wave number k and absorption coefficient α at the wavelength of light in vacuum λ_0 are given by

$$k = \frac{2\pi}{\lambda_0} n, \qquad \alpha = \frac{4\pi}{\lambda_0}\kappa. \tag{2.7}$$

The skin depth, the distance at which the intensity of the electromagnetic wave will be attenuated by a factor 1/e, can be then expressed as

$$\delta = \frac{1}{\alpha} = \frac{\lambda_0}{4\pi}\frac{1}{\kappa}. \tag{2.8}$$

For most metals and light waves at optical frequencies, the skin depth is of the order of 50 nm. An example of the wavelength dependence of the skin depth for molybdenum is shown in Figure 2.2.

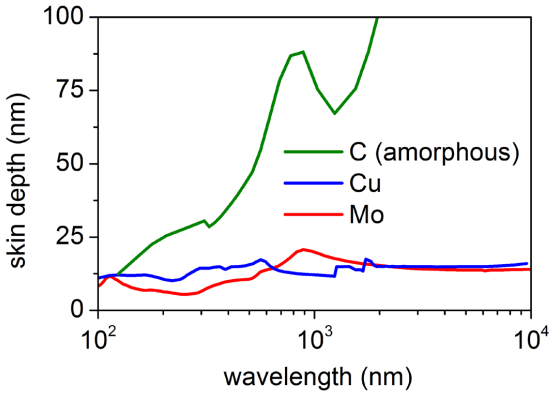

Figure 2.2. The skin depth as a function of the wavelength, as calculated from the extinction coefficient data from [Palik].

2.3 Reflectivity of polarized light

The reflection and transmission of light depends on polarization of the incident ray. For the specular reflection under the assumption of linear, homogeneous and isotropic media, the reflection coefficients for light components with different polarizations are given by the Fresnel's formulas:

$$R_p = \frac{\tan^2(\theta_i - \theta_t)}{\tan^2(\theta_i + \theta_t)}, \tag{2.9}$$

$$R_s = \frac{\sin^2(\theta_i - \theta_t)}{\sin^2(\theta_i + \theta_t)}, \tag{2.10}$$

where R_p and Rs define the reflection coefficients for the light components with polarizations parallel and perpendicular to the plane of incidence.
The reflectivity R observed for a natural (unpolarised) light containing an equal mix of s- and p-polarisations is given by

$$R = \frac{R_s + R_p}{2} \tag{2.11}$$

The difference between R_s and R_p vanishes in the case of perpendicular incidence ($\theta_i = 0$), and the reflectivity of the medium becomes equal to

$$R = \frac{(n_1 - n_2)^2}{(n_1 + n_2)^2} \tag{2.12}$$

where the light comes from the medium with the refractive index n_1 to the medium with the refractive index n_2.
Because of the flatness of reflectivity at small incident angles (Figure 2.3), it is often sufficient to adopt this formula also for angles below 10 degrees.

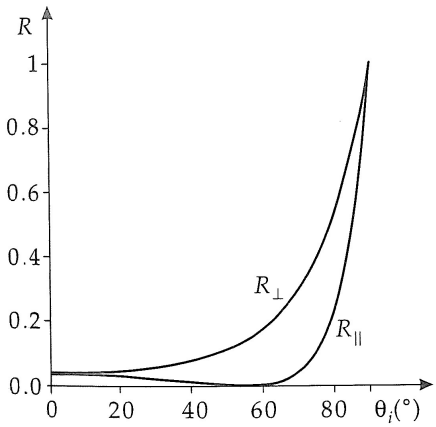

Figure 2.3. Dependence of reflection coefficients on state of polarization and incidence angle for a glass-air interface [Benenson 2002].

2.4 Specular and diffuse reflectivity

When surface roughness is not negligible, i.e. has the scale compared to the wavelength of the incident light, part of the light bounces off the surface in all directions (Figure 2.1). Thus the light reflected from a rough mirror surface consists of two components: specular reflected light and diffusely reflected (scattered) light with randomly oriented rays [Benenson 2002]. The most common description of the angular distribution of diffusely reflected light is the reflection of light with equal luminance in all directions (Lambertian reflectance). Alike the reflectivity definition given in section 2.1, the specular (R_{spec}) and diffuse (R_{dif}) reflectivities are defined as the ratios of intensities of specularly and diffusely reflected ligth to the intencity of the incident light. The total reflectivity (R_{tot}) is the summ of the two components:

$$R_{tot} = R_{spec} + R_{dif} \tag{2.13}$$

Surface roughness influences the specular reflectivity in a way as described by the Bennett formula [Bennett 1961] (reflectivity at normal incidence):

$$R_{spec} = R_0 \cdot e^{-(4\pi\sigma)^2/\lambda^2} \tag{2.14}$$

,

where λ is the wavelength of the incident light and R_0 represents the specular reflectivity of a material with ideally smooth surface, or, in other words, a material with the root-mean-square (RMS) roughness $\sigma = 0$. The RMS roughness is expressed as follows:

$$\sigma = \sqrt{\frac{1}{N} \cdot \sum_{i=1}^{N} z_i^{\,2}} \,, \tag{2.15}$$

where N is the number of discrete, equally spaced point measurements of the surface elevation z_i with respect to the mean level of the surface (Figure 2.4) [Bennett 1999].

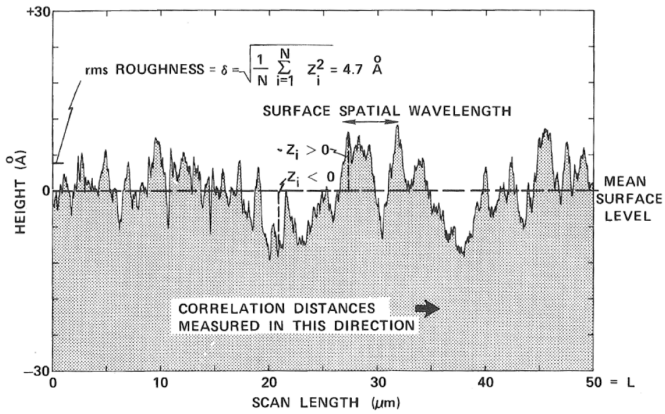

Figure 2.4. Scematic representation of a rough surface showing statistical parameters [Bennett 1999].

According to equation (2.14), surface roughness affects the reflectivity in the UV and visible wavelength ranges stronger, while R_{spec} is less sensitive to surface roughness in the IR range of the spectrum. It has to be noted, however, that the applicability of the Bennett formula is limited to wavelengths that are much longer than the surface roughness, such that the contribution of the diffuse reflectivity to the total can be basically neglected. According to Bennett, this quantitatively means that λ has to be about 100 times longer than σ (see figure 3 in [Bennett 1961]). The results of corresponding analyses of the reflectivity spectra measured during this work will be discussed in section 6.2.3.

Chapter 3. Processes affecting the mirror properties

Mirrors exposed to plasma undergo bombardment by plasma and impurity particles originating from erosion of wall materials at different locations within the device. Impurity particles eroded from plasma-facing components and transported to the mirror can be implanted into the mirror surface and cause erosion of the mirror material. Under certain conditions, formation of re-deposited impurity layers on the mirror surface can occur. These processes depend on the type of species, energy and incident angles of particles incoming to the mirror surface and can lead to degradation of mirror properties. In this chapter these processes will be briefly described and their influence on the mirror reflectivity will be illustrated.

3.1 Surface erosion by particle bombardment

Physical sputtering is an erosion mechanism, which involves the removal of atoms from the surface of a solid as a result of an impact of energetic particles. When an incident ion or neutral atom collides with lattice atoms, it causes their displacement in the form of collision cascades. The energy of the particle is transferred to the affected lattice atoms and dissipated on friction with electrons. If a collision cascade takes place within a near surface layer, surface atoms may receive sufficient energy to overcome the surface energy barrier (the surface binding energy) and be ejected (sputtered) off the material. The sputtering yield Y is defined as the number of ejected surface atoms per one incident projectile. For low energies of incident particles, displaced lattice atoms have low or no chance to overcome the surface energy barrier, the sputtering yield decreases strongly and becomes zero below a certain threshold energy E_{th} specific for each projectile-target combination.
The incident energy and angle dependence of the sputtering yield can be expressed by analytical empirical formulae of Bohdansky-Yamamura [Bohdansky 1984, Yamamura 1983] or Eckstein-Preuss [Eckstein 2003] and are illustrated in Figure 3.1. The decrease of the sputtering yield at high energies of incidence is due to collision cascades taking place deeper in the solid and correspondingly lower chances for surface atoms to receive sufficient energy for sputtering. For grazing incidence, more energy is deposited within the near surface layer and the sputtering yield increases, except for very shallow incident angles when reflection dominates.

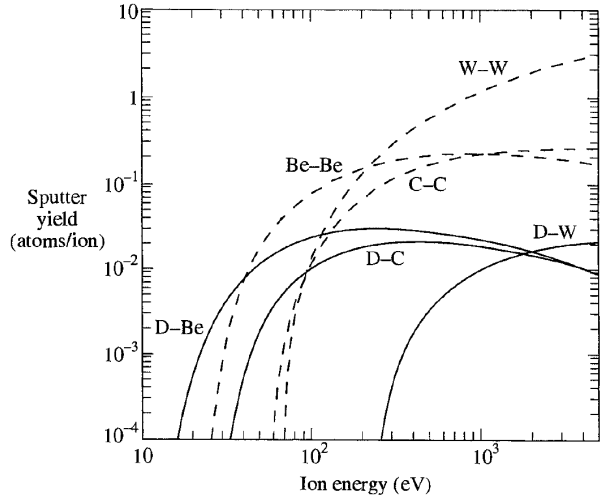

Figure 3.1. Energy dependence of the sputtering yield for Be, C and W targets in case of D-ion and self-bombardment [Wesson 2004]

The results of modelling and experiments, shown in [Voitsenya 2013] corroborate the dependence of sputtering rate on crystal orientation of grain. This investigation revealed that the densest faces sputter the fastest (in case of body centered cubic structure, such as tungsten has, the face (110), in case of face centered cubic structure characteristic for stainless steel, the face (111)).

The sputtering yield of a given material depends on its crystallographic structure, i.e. whether the material is polycrystalline (PC) or a single crystal (SC), and, in the case of PC materials consisting of individual grains, on the crystallographic plane of each grain surface and its orientation with respect to the incoming particle flux. Therefore, different grains of a PC material can be sputtered with different rates. Preferential sputtering of individual grains leads to the development of a surface relief (surface roughness), which tends to reduce the sputtering yield and smear its angular dependence [Kuestner 1998, Ruzic 1990]. For example, in [Voitsenya 2013a] energetic Ar ions bombarded tungsten mirror specimens. Averaged eroded depth was 3.9 μm, while maximal step between neighbor grains was 1.5 μm. The most sputtered face was the densest one, (110), and the most resistant face was (111). Such a way the ratio of sputtering speeds could be estimated as (3.9+0.75) / (3.9-0.75) = 1.5 times.

In the case of metallic mirrors, roughening of the surface due to the variation of the erosion rate over the mirror surface causes the incident light to reflect diffusely. As a result, the specular reflectivity (R_{spec}) decreases and the resolving power of the mirror deteriorates. Therefore PC metallic mirrors exhibit a very pronounced decrease of their reflectivity due to physical sputtering under long-term CXA bombardment [Konovalov 2001]. The development of the surface roughness due to sputtering is higher for higher ion energy, i.e. the difference between sputtering rate of differently oriented grains increases with increasing ion energy [Konovalov 2012].

The mirror material, as well as the energy, mass, incident angle and flux of incoming particles have the strongest impact on the sputtering rate of the mirror surface [Eckstein 1993]. In fact, the reflectivity of a mirror exposed under erosion conditions depends not on the thickness of the sputtered layer, but on the roughness of the resulting surface. The surface roughness is, in turn, correlated with the particular material used for the mirror and its crystallographic structure. This is illustrated in Figure 3.2, where reflectivities of Mo and W mirrors with different crystallographic structures are plotted against the eroded layer thickness. Another

example of mirror degradation due to erosion of the surface is shown in Figure 3.3 for a copper (Cu) mirror [Lipa 2006]. Such a behaviour, namely reduction of the mirror reflectivity, was confirmed in many laboratory and tokamak experiments performed in order to investigate the influence of erosion on the mirror properties [Wienhold 2005, Voitsenya 2001b].

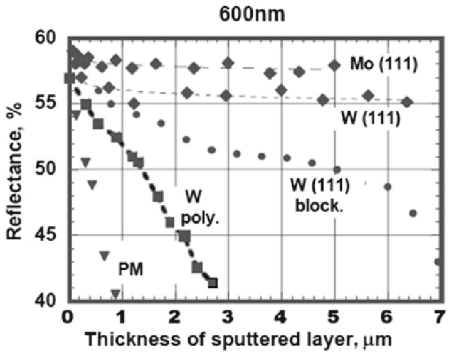

Figure 3.2. The reflectivity of Mo and W mirrors with different crystallographic structures at 600 nm as a function of the thickness of the layer eroded by deuterium ions [Voitsenya 2001a].

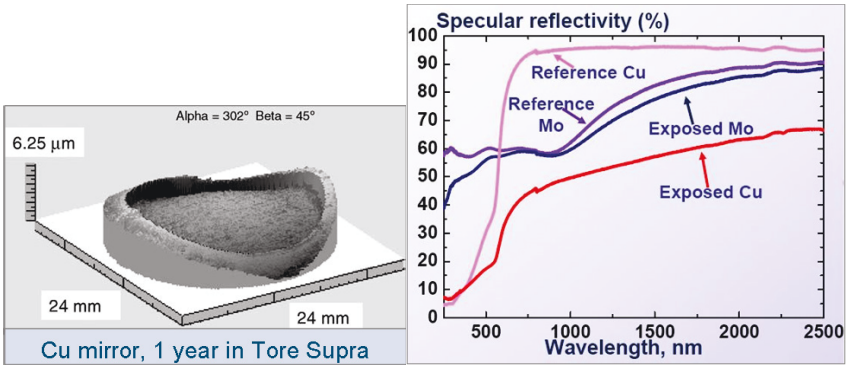

Figure 3.3. Left: 3D reconstruction of the surface of a copper mirror exposed in the Tore Supra tokamak for one year. The figure shows strong erosion of the exposed mirror surface. Right: changes of the mirror reflectivity curve in comparison with the reference sample for Cu and Mo mirrors exposed under the same conditions in Tore Supra [Lipa 2006].

In earlier works [Litnovsky 2007b, Litnovsky 2005], the importance of keeping the surface relief of a PC mirror small compared to the wavelength of the probing light as a measure to minimize the diffuse reflectivity was shown. This means that small grain sizes and preferably similar crystallite orientation must be achieved for PC mirrors. It had been proposed [Voitsenya 1999] that the use of nanocrystalline mirrors with grain sizes much smaller than the required wavelength may be suitable for in-vessel diagnostic mirror in a fusion reactor. For this proposes the characteristic scale length of surface roughness developing due to sputtering by charge exchange atoms should be significantly less than the wavelength of the light being analyzed. For example, for visible or near-infrared ranges of the spectrum mirrors with crystallite sizes ≤ 70 nm could be acceptable as in-vessel mirrors for a fusion reactor. Preparation of such mirror samples, however, is a challenging task, which can be resolved by using coatings. Although metallic coatings also represent PC materials, they have substantially smaller grain sizes and, if grown with equally oriented grains, should have

similar sputtering rates over the entire surface. For example, these can be coatings with a columnar structure of the surface with a small diameter of columns. This means that surface roughness should not develop or at least should be less pronounced on coated mirrors compared to bulk PC materials. To minimize the diffuse reflection, the characteristic grain size of such coatings must be below the wavelength of light used for the optical diagnostics under consideration [Konovalov 2001]. Therefore, not only the choice of materials, but also a proper adjustment of the coating procedure is important in order to ensure the quality and stability of respective coatings. Coated mirrors are also beneficial for economical reasons since small amounts of high-reflective but expensive materials may be used to create large coated areas on relatively inexpensive substrates. This makes coatings a very attractive mirror concept even compared to SC mirrors. Some recent investigations [Voitsenya 2013b] suggest, however, that development of the surface roughness may impair the performance of coatings since the longitudinal length scale of the surface roughness is typically much larger than the grain size. As a consequence, degradation of the mirror reflectivity can occur for fine grain mirrors due to the development of a large-scale (1 - 10 μm) surface relief, even though the mirror grain size (~ 0.1 μm in the case of Rh-film mirrors) is much less than the wavelength of the probing light.

SC materials have a clear advantage of the homogeneous sputtering of the entire surface. In particular, SC mirrors made of mono-crystalline W, Mo and Ni with surfaces represented by differently oriented crystallographic planes (111, 100, and 110) were tested in different simulation experiments under conditions similar to other mirror experiments [Konovalov 2001, Voitsenya 2001a], and no noticeable degradation of the mirror reflectivity at a wavelength of 600 nm was observed even after layers of ~5 μm (W) and ~7 μm (Mo) were eroded (see Figure 3.2). These results emphasize the beneficial properties of monocrystalline mirrors. In [Bardamid 2002] perfect SC Mo and W preserve optical characteristics after bombardment by energetic D^+ with fluences 5×10^{24} ion/m^2 and 7×10^{24} ion/m correspondingly. Deformed SC Mo degraded few times faster than perfect SC. In this work it was shown, that perfect SC mirrors could be used as a reference and test mirrors for experiments relevant for fusion reactor. However, application of SC mirrors for optical diagnostics in fusion devices is restricted due to possible expensiveness of such mirrors, depending on the material, and technological limitations in the mirror size. The largest SC Mo mirror produced for these purposes up to now measures 140 mm in diameter.

3.2 Surface contamination via deposition and impurity implantation

3.2.1 Implantation of impurities

Energetic particles impacting at the surface of a solid undergo collisions with lattice atoms and are scattered in different directions. As a result of such collisions, incident particles slow down and may either leave the surface as reflected atoms or come to rest at some distance under the surface. These implanted particles finally occupy available vacancy locations within the lattice structure or become interstitial atoms. The depth distribution of implanted particles depends on the energy and angle of incidence and has in general a Gaussian profile. Typical range of plasma and impurity ions in solids in fusion applications is of the order of few nanometres. For sufficiently high surface temperatures atom diffusion may contribute to broadening of depth profile of implanted particles and lead to formation of phases of different chemical compounds (alloying, carbidization, oxidation, etc). Such compounds are often non-

metallic or anisotropic, thus their optical properties may be significantly different from those of the original metallic mirror material (see chapter 2).

3.2.2 Formation of deposited layers

Impurity layers re-deposited on the mirror surface strongly affect the mirror reflectivity due to the fact that light rays pass the surface layer at least twice during the reflection process. In general, the reflectivity of a surface with a deposited layer on it represents a strong function of the layer thickness. As an example of the influence of an a-C:H film on the reflectivity of a molybdenum mirror at normal incidence the ellipsometric simulations for two different types of layers found in fusion devices are provided on the Figure 3.4 [De Temmerman 2006]:

- soft (polymer-like) with a refractive index of 1.6 at 632.8 nm and H/C ≈ 0.8;
- hard (diamond-like) with a refractive index of 2.4 at 632.8 nm and H/C ≈ 0.3.

In these simulations a homogeneous film on a semi-infinite substrate with the RMS roughness $\sigma = 0$ was considered. Simulation results show that even a very thin carbon film of less than 20 nm thickness can strongly modify the reflectivity properties of metallic mirrors. These results are confirmed by measurements performed on mirrors with films deposited in the laboratory [Matveeva 2008] as it is shown in Figure 3.5.
As one can see from Figure 3.4 and Figure 3.5, after a certain thickness of the deposited layer is reached, the reflectivity can increase again. It can even exhibit oscillating wavelength dependence due to interference of multiply reflected rays in the layer. The relation (3.1) describes the maxima of the reflectivity:

$$k\lambda = 2dn \,, \tag{3.1}$$

where k is an integer number, λ – the wavelength, d – the thickness of the layer, and n – the refractive index of the layer.
Although experiments and simulations may help to predict the properties of films deposited in the laboratory, i.e. the films that are uniform and well pre-characterized, the situation turns out to be very different in the case of a tokamak environment where the layers will be formed non-uniformly and with rather unpredictable deposition rates. The thickness of resulting layers may vary significantly over the surface even for a single mirror. Moreover, in future fusion reactors, depending on the mirror location and PFC materials, not only a-C:H but also mixed metallic (as well as non-metallic) layers will be formed leading to complex surface composition and morphology, which are hard to assess. In particular, metallic deposits formed on in-vessel components in present day fusion devices are observed to have non-uniform and porous structure [De Temmerman 2007]. Extinction coefficients for metals are higher than for amorphous carbon layers (Figure 2.2), i.e. light wave penetration depths will be correspondingly smaller on metallic layers compared to a-C:H films. Therefore formation of metallic layers can lead to lower penetration depths of the incident light wave and thus partial or complete replacement of the mirror reflectivity by the reflectivity of the respective deposited layer. The usage of mirrors contaminated by metallic impurities as optical components in fusion devices may no longer be possible [De Temmerman 2007]. In overall formation of deposited layers in tokamaks leads to unknown reflectivity characteristics of contaminated mirrors with no reliable predictions possible. Therefore the only trustworthy reflectivity of a mirror is that of the clean mirror.

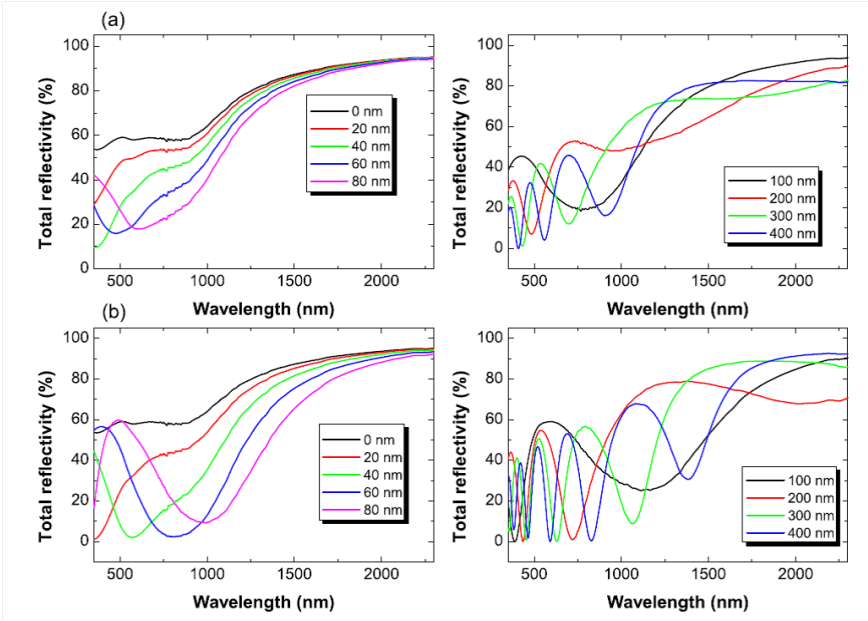

Figure 3.4. Dependence of the reflectivity of a Mo mirror on the thickness of a soft polymeric (a) and hard diamond-like (b) a-C:H film [De Temmerman 2006].

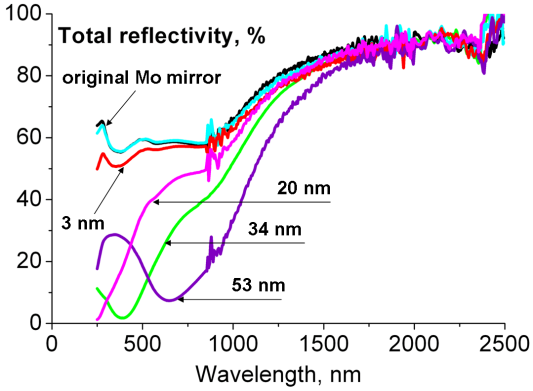

Figure 3.5. Dependence of the reflectivity of a Mo mirror on the thickness of hard laboratory-deposited a-C:H films [Matveeva 2008].

3.3 Surface modification due to chemical processes

Strong variation of particle and energy loads along the first wall and divertor calls for different requirements with respect to the choice of plasma-facing materials at different locations within the device. Erosion and transport of wall materials in plasma unavoidably lead to material re-deposition elsewhere in the device, in particular, on diagnostic mirrors. As

a result, multi-component surfaces and mixed material layers are formed, which are subjected to thermal and ion-driven chemical and physical processes. Implantation and diffusion of impurities on one hand and formation of chemical compounds on the other hand govern the dynamic change of the mirror surface composition during plasma operation. Solid state reactions between surface components may lead to formation or dissociation of thermo-dynamically stable chemical phases, e.g. alloys, oxydes, carbides, etc, which can have very different physical and optical properties, thus affecting the performance of diagnostic mirrors. As an example, Figure 3.6 illustrates how surface carbidization affects the reflectivity of Mo mirrors.

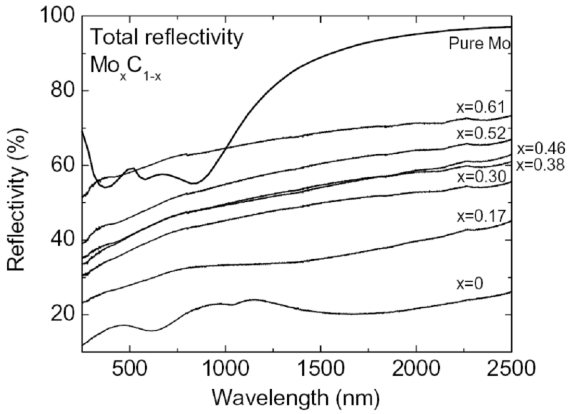

Figure 3.6. Reflectivity of Mo_xC_{1-x} in the wavelength range 250 - 2500 nm depending on the compound composition stoichiometry [De Temmerman 2005].

Chemical reactions between incident and surface atoms can lead to formation of volatile compounds and thus may also lead to erosion of wall materials. E.g., chemical reactions between carbon and incident hydrogen ions and atoms lead to formation of volatile hydrocarbon radicals as well as to loosely bound hydrocarbon precursors, which are sputtered easier due to lower threshold energy. Chemical erosion itself has no energy threshold and thus is the dominating erosion process at low energies of incident particles. However, unlike physical sputtering, chemical erosion takes place only for specific combinations of incident and surface atoms. In the case of first metallic mirrors, chemical erosion of deposited a-C:H layers can lead to cleaning of the mirror surface without causing damage to the bulk mirror material as it was confirmed earlier [Matveeva 2008, Laengner 2009, Litnovsky 2011a].
Chemical erosion represents a multi-step process. It depends on the surface temperature and material properties such as crystalline structure, impurity atoms concentrations, lattice defects, etc [Haasz 1998, Vietzke 1987b]. Also strong dependence of the chemical erosion yield on the presence and impact energies of seeded impurity projectiles was observed [Schlueter 2008]. The basic processes underlying chemical erosion in the case of hydrogen bombardment of carbon-based materials are the following [Roth 1996]:
a) Carbon atoms at the edges of graphitic planes are hydrogenated to CH_3–C complexes. Thermal release of hydrocarbons takes place at surface temperatures above 400 K. At surface temperatures above 600 K the chemical erosion yield Y_{therm} decreases due to molecular recombination of hydrogen at the surface (release of H_2 molecules).
b) Radiation damage created by incident ions to lattice atoms enhances the above thermal reaction by providing open bonds for hydrogen attachment. This process is isotope dependent and the corresponding contribution is noted as Y_{dam}.

c) If carbon atoms at the surface are not embedded in a perfect crystal structure, they form fully hydrogenated CH_3 groups with only one remaining bond to the graphitic lattice. The surface binding energy of such groups is much smaller (~1 eV) than that of carbon surface atoms at their regular lattice positions (≈ 7.4 eV) leading to enhanced physical sputtering. Kinetic ejection of surface hydrocarbon complexes is called ion induced desorption (surface contribution Y_{surf} [Roth 1999]).
In total, the chemical erosion yield of carbon under hydrogen bombardment is composed of three contributions:

$$Y_{chem} = Y_{therm}(1 + DY_{dam}) + Y_{surf}. \tag{3.2}$$

In [Roth 1996], analytical expressions for Y_{therm}, Y_{dam} *and* Y_{surf} can be found, which give a quantitative description of the chemical erosion under low fluxes. Parameter D depends on the hydrogen isotope.
The surface temperature dependence of the chemical erosion yield is illustrated in Figure 3.7. The yield increases from the room temperature and has a maximum at a temperature T_{max} = 700 - 900 K that depends on the incoming ions energy.
Swift chemical sputtering represents another chemical erosion mechanism, which was identified and explained by means of molecular dynamics computer simulations. The main mechanism underlying this process is breaking of a covalent C-C bond due to momentum transfer from a hydrogen ion approaching the region between the two carbon atoms (repulsive core-core interaction) [Nordlund 2006]. Swift chemical sputtering mechanism can be important for metals if for some reason surface atoms have a weakened bond to the surface [Bjorkas 2009, Nordlund 2011]. In particular, beryllium can be chemically sputtered in the form of BeD molecules as it was determined experimentally in the PISCES-B divertor simulator [Doerner 2009, Nishijima 2009].

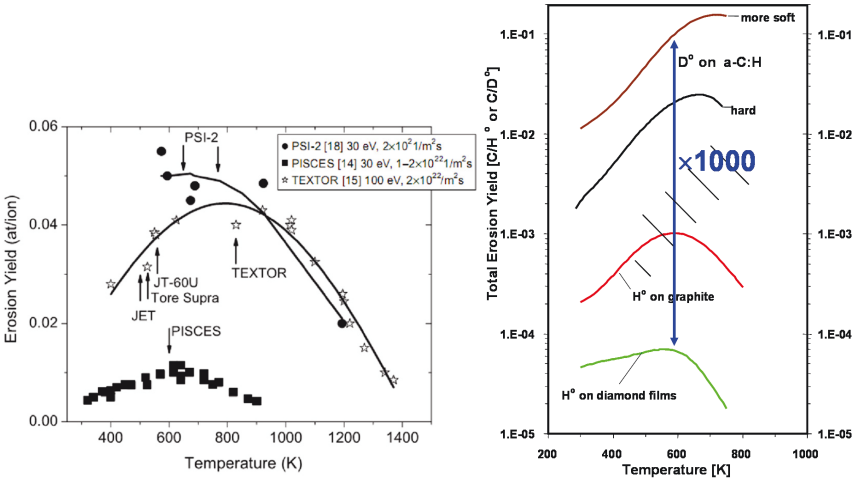

Figure 3.7. Surface temperature dependence of chemical erosion as measured in different high-flux devices (left) [Roth 2004], and for amorphous hydrogenated carbon layers (a-C:H/D) with impact of thermal atoms (right) [Vietzke 1987a].

Measurements of the chemical erosion yield in tokamaks and plasma simulators allowed determining the flux dependence of the chemical erosion yield, which decreases strongly at high ion fluxes (> 10^{22} ion/m^2/s) [Roth 2004] (Figure 3.8).

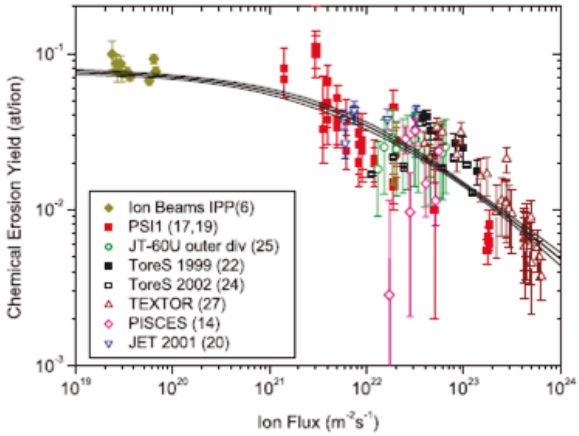

Figure 3.8. Chemical sputtering yield dependence on particle flux density [Roth 2004].

Chapter 4. Surface characterization techniques

Metallic mirrors of monocrystalline molybdenum, as well as polycrystalline copper mirrors, molybdenum and tungsten substrates coated by rhodium and molybdenum were characterized before and after plasma exposure in the TEXTOR tokamak. Optical measurements (spectrophotometry, spectroscopic ellipsometry) and surface characterization (optical microscopy, stilus profilometry) were performed in the MirrorLab in Forschungszentrum Juelich, which was specially equipped for the mirror research [MirrorLab]. Additional analyses with Scanning Electron Microscopy (SEM), Energy Dispersive X-ray Spectroscopy (EDX) and Secondary Ion Mass-Spectrometry (SIMS) were also made in Forschungszentrum Juelich. X-ray photoelectron spectroscopy (XPS) and several SEM measurements were done in the University of Basel.

4.1 Optical microscopy

In optical microscopes the surface is illuminated with the visible light and magnification of the sample is achieved by using a system of lenses. In such a way objects about one μm in size can be successfully resolved and studied. In this thesis an optical microscope Carl Zeiss Axio Observer was used. The zooming capability of the microscope is 100x. Using the native software mode for image series acquisition from different focus positions, it is possible to obtain an in-focus image of a rough surface with clearly visible micro-relief. Still the optical microscopy gives only qualitative information on the structure of the surface and other methods have to be used to get a deeper insight into its composition and properties.

4.2 X-Ray photoelectron spectroscopy

The X-ray photoelectron spectroscopy (XPS), also referred to as electron spectroscopy for chemical analysis (ESCA), represents a powerful technique for the surface elemental composition studies. XPS is able to identify and quantify the elemental composition of the outer 10 nm or less of any solid surface. The detection limit for the chemical element of interest is 0.05 at.%. H and He are not detectable due to their extremely low photoelectron cross section and the fact that XPS is optimized to analyse core electrons. In addition, XPS allows identifying the chemical environment where the respective element exists [van der Heide 2012].
Photoelectron spectroscopy involves the single-step process of ejection of electrons from atoms or molecules following bombardment by monochromatic photons [Hollas 2010]. A schematic example of the photoelectron emission process and the basic components of an XPS instrument are shown in Figure 4.1.

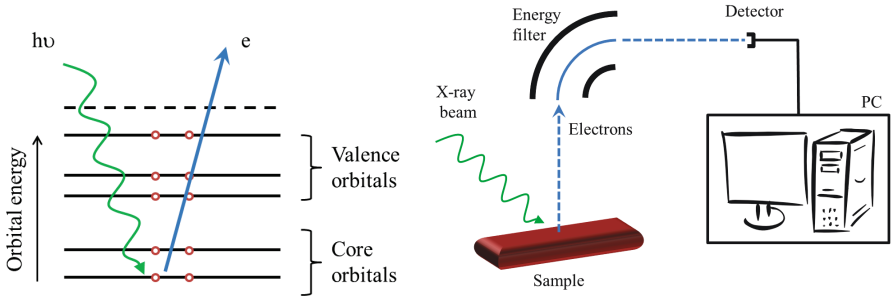

Figure 4.1. a) Schematic example of the photoelectron emission process and b) the principal components of a photoelectron spectrometer

Bombardment of the sample with photons with energy sufficient to overcome the work function Φ of the sample material will lead to ejection of photoelectrons with kinetic energy

$$\frac{1}{2}m_e v^2 = h\nu - \Phi - E_{binding}, \tag{4.1}$$

where $h\nu$ is the photon energy, $E_{binding}$ – electron binding energy, m_e and v – electron mass and velocity. The work function Φ is the minimum energy needed to remove an electron from a solid to a position immediately outside the solid surface.

The measured physical quantity is the remaining kinetic energy of emitted electrons and determination of the kinetic energy of an outgoing electron is the cornerstone of the photoelectron spectroscopy. The energy of photons is known. The annihilation of photons during photon-electron interaction happens with complete energy transfer. Therefore the kinetic energy of an electron is a measure of the electron binding energy. The binding energy of core electrons is an intrinsic material property, element and environment specific, and does not change with the photon energy. Chemical environment of an atom, molecule or ion leads to slight variations in the electron binding energy for a particular element and energy level, which can be detected, thus allowing chemical composition analysis.

XPS measurements of mirror samples used in this work were performed for each sample twice: before and after exposures in TEXTOR. First measurements were performed right after the coating. The samples were transferred from the high vacuum deposition chamber to the ultra-high vacuum (UHV) chamber of the photoelectron spectrometer without breaking the vacuum. The UHV chamber was pumped down to a base pressure of about 2×10^{-4} Pa. Second measurements were done after the mirrors were exposed to plasma and analysed by other techniques in the lab, including exposure of the samples to air.

The electron spectrometer used in this work was equipped with a hemispherical analyser and an X-ray source (Mg Kα excitation, hν = 1253.6 eV) for core levels spectroscopy. As a reference for the electron binding energy calibration, the Au 4f7/2 line of a gold sample was set to 84.0 eV. An example of a survey XPS spectrum is presented on Figure 4.2.

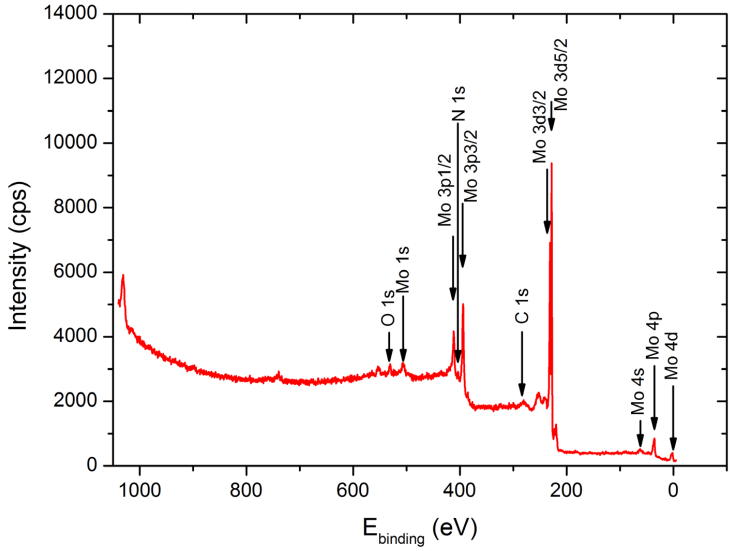

Figure 4.2. XPS spectrum collected from a Mo-coated mirror measured *in-situ* after the coating procedure.

4.3 Secondary ion mass-spectrometry

For depth profiling and elemental surface composition measurements, the double-beam time-of-flight (ToF) secondary ion mass spectrometry (SIMS) facility ION ToF IV at FZJ was used. In the SIMS technique the surface is bombarded with a probing ion beam (Bi^{3+}), which produces a collision cascade in the near surface region. The sputtered secondary atoms and ions are then analysed using the ToF method.. Depth profiles are obtained by alternate application of probing and sputtering ion beams. The sputtering ion beam usually consist of heavy ions (Cs^+, O^{2+}, O^- , Ar^+, and Ga^+) at energies 1-30 keV and leads to efficient sputtering of surface atoms and thus continuous recession of the surface within the area analysed by the probing beam. The SIMS facility used for measurements of diagnostic mirrors presented in this work utilizes for sputtering Cs^+ ion beam with ion energies 1-2 keV. Typical SIMS craters formed during measurements were 200 x 200 μm^2 or 300 x 300 μm^2.
SIMS represents a very sensitive technique which is capable of detecting elements with the surface abundance of only 10^8 at/cm^2. However, since the sputtering yield of different elements and the ratio of neutral and ionized species depend strongly on the surface composition, surface conditions and chemical environment, it is very difficult to obtain quantitative information on the surface composition with this technique. Although SIMS is not well suited for quantitative comparison of different elements, it is successfully applied for identification of the presence of particular elements on the surface and their depth-concentration profiling.

4.4 Surface profiling

To measure thicknesses of deposited layers, SIMS craters were scanned with the DEKTAK-6M stylus profiler (profilometer). Profilometer represents a mechanical tool in which a small needle (stylus) that can move up and down is dragged across the surface and thus records the vertical surface profile. The radius of a standard diamond stylus is 12.5 µm. In combination with SIMS measurements, the thickness of a deposited layer can be defined. SIMS craters sputtered down to the interface with the substrate material are measured with the profilometer and the depth of the crater defines the layer thickness.

4.5 Scanning electron microscopy

Magnification achievable by optical microscopes (~1000x) is limited by the wavelength of visible light. Electrons have shorter wavelengths; therefore in electron microscopy larger magnifications, up to two million times, become possible. To produce an image of the surface, the primary electron beam is generated, accelerated up to 10-40 keV and focused into a point of about 1 nm in diameter, being then controlled to scan the surface; thence it is called the scanning electron microscopy (SEM). The primary electrons interact with the surface atoms producing several detectable signals, among which backscattered electrons, secondary electrons and X-rays are used the most for the analysis. Secondary electrons detection allows visualizing the surface relief. Due to their relatively low energy, secondary electrons are effectively slowed down on their way up to the surface, therefore only electrons produced near the surface can reach the detector. Backscattering of high energy primary electrons occurs more likely on heavy elements and therefore backscattered electrons detection allows visualizing the surface composition. X-rays are generated as a result of interaction of primary electrons with the inner shell of atoms. The energy of emitted photons is characteristic for each element and therefore X-rays detection gives additional insight into the elemental composition of the surface. In this work SEM imaging of mirrors was done to analyse the stability of the coatings and to access surface relief modifications after plasma exposures.

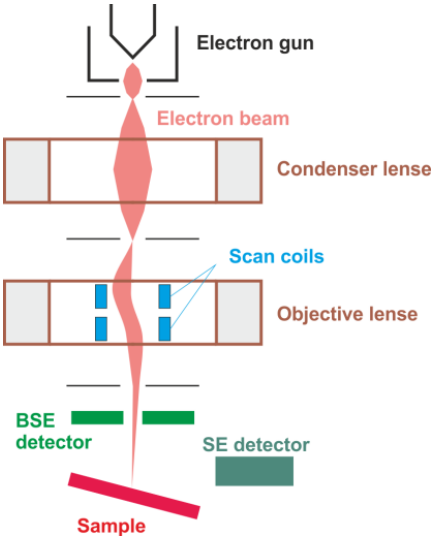

Figure 4.3. Schematic representation of a SEM device.

4.6 Electron backscatter diffraction

The electron backscattering diffraction (EBSD) represents a technique, which is used to evaluate the crystallographic orientation of the material. In particular, it allows identifying the preferred orientation of crystallites and the grain size in a polycrystalline material. EBSD measurement is conducted using an SEM with a special detector for diffracted electrons. The sample is inclined with respect to the electron beam and to the diffraction camera. Some backscattered electrons leave the sample at the Bragg's condition

$$n\lambda = 2dsin\theta, \tag{4.2}$$

related to the spacing of the atomic lattice d, where n is an integer, λ is the wavelength of the incident electron wave and θ is the inclination of the incident electron beam with respect to a particular scattering plane within the crystal. Diffraction of electrons on different lattice scattering planes results in an electron backscatter diffraction pattern, which can be related to the crystal phase and orientation.

4.7 Spectrophotometry

Measurements of the mirror reflectivity contribute significant part to the thesis and were carried out with a double-beam UV-VIS-NIR spectrophotometer Perkin Elmer Lambda 950, equipped with an integrating sphere. Measurements were performed for the spectral range of 250-2500 nm.

The double-beam spectrophotometer measures the relative intensity of two light beams, one reflected from the reference sample and the other one reflected from the tested specimen (Figure 4.4 (c)). The device is equipped with an integrating sphere of 150 mm in diameter. The integrating sphere is coated with a highly-reflective material (Spectralon^{TM}), which provides almost 100% reflectivity of light in the entire working wavelength range. The total and diffuse reflectivity of samples can be measured. To measure the diffuse reflectivity, the sample is illuminated at an incident angle of 4° with respect to the normal; the specular reflected light leaves the sphere through a special aperture (light trap, Figure 4.4 (a)) and the diffusely reflected light is registered by detectors at the bottom of the sphere. For the total reflectivity measurements, the specular light trap aperture is closed with a white plate. The white plate is also coated with Spectralon^{TM} thus providing the sphere with a continuous smooth Spectralon^{TM} surface of the inner wall. The specular reflected light is reflected back from the white plate into the sphere and is therefore also detected (Figure 4.4 (b)). The specular reflectivity is then calculated as the difference between the total and the diffuse parts.

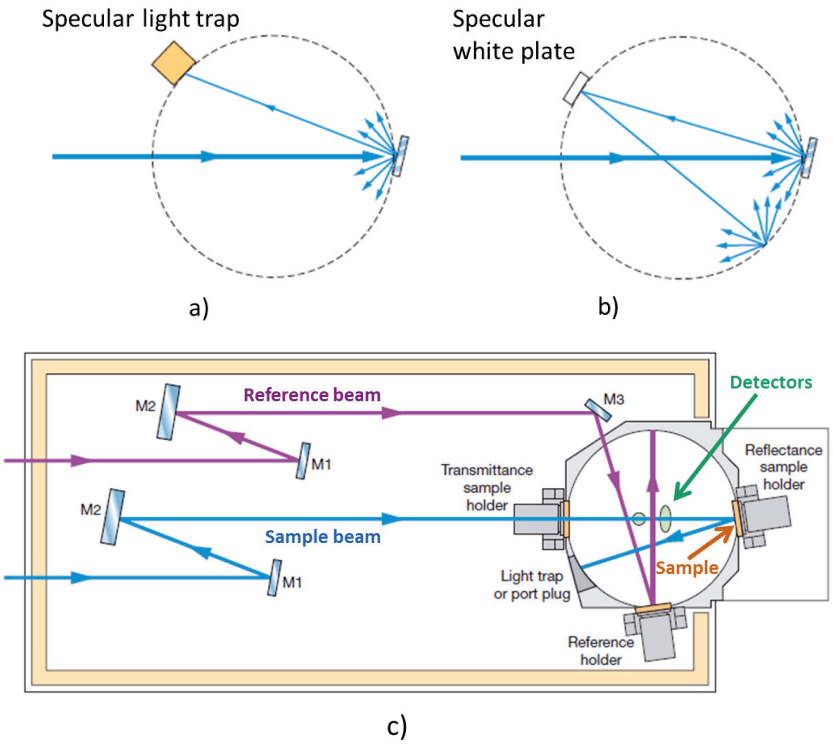

Figure 4.4. Sampling configurations for diffuse (a) and total (b) reflectance measurements; the optical design of spectrophotometer Perkin Elmer Lambda 950 (c)

4.8 Spectroscopic ellipsometry

Ellipsometry characterizes light reflection or transmission of materials. It represents a non-destructive measurement technique and is used to determine optical properties of materials, as well as thicknesses of thin films. The key feature of ellipsometry is that it measures the change in polarized light upon light reflection on a sample (or light transmission by a sample) [Fujiwara 2007]. Ellipsometry measures two values, ψ and Δ, which represent the amplitude ratio and the phase difference between the p- and s-polarized light waves. The ratio of Fresnel coefficients, which determine the ratio of the amplitude of incident and reflected waves for s- and p- components, is related to ψ and Δ, so-called ellipsometric angles, as

$$\frac{r_p}{r_s} = \tan(\psi) \cdot \exp(j\Delta). \tag{4.3}$$

In the spectroscopic ellipsometry the spectra of ψ and Δ are measured by changing the wavelength of light. An estimation of the optical properties (refractive index) of the material under investigation is not straightforward and requires an iterative computer procedure that fits the calculated parameters to the measured values based on pre-defined model of the surface. Since even a good fit of simulated and experimental data does not guarantee the correctness of the model, it is highly recommended to support ellipsometry simulations with other surface analysis techniques in order to build a proper surface model.

For the measurements in this work, the ellipsometer SENTECH SENresearch SE 800 with the wavelength range from 240 nm up to 1100 nm and a spot size of the light beam 1 mm^2 was used. A scheme of methodology underlying ellipsometry measurements is shown in Figure 4.5.

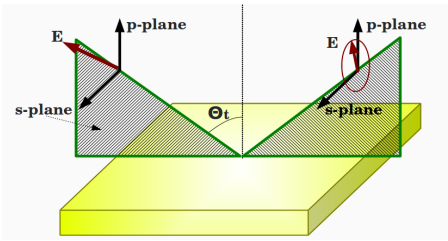

Figure 4.5. Scheme of ellipsometric measurements.

4.9 Electron Probe Micro Analysis

In Electron Probe Micro Analysis (EPMA) an electron beam accelerated to 5 - 30 keV is focused on the material surface. In this sense it represents an SEM. Inelastic electron collisions lead to excitation of substrate atoms within a small interaction volume of 1 - 9 μm^3. De-excitation of atoms is possible in two processes presented in Figure 4.6: the Auger process, i.e. ejection of an outer shell electron, and emission of a photon. In the latter case, which will be described in more detail here, relaxation of an atom is accompanied by a characteristic X-ray emission. The intensities of this emission are measured by means of spectrometry and determine the concentrations of different elements in the surface. Two different types of systems used for detection of X-rays in EPMA are wavelength dispersive spectrometers (WDS) and energy dispersive spectrometers (EDS). Generally WDS is utilized more often due to an order of magnitude better energy spectra resolution (1 - 10 eV) and one to two order of magnitude lower detection limits (10^{-3} - 10^{-2} %). WDS uses the principle of constructive interference to select X-rays according to their wavelength using a diffraction crystal. Continuously adjusting the wavelength of incidence of X-rays on the crystal, a full spectrum of emitted X-rays can be acquired according to the Bragg's rule (see section 4.6). High resolving power of WDS is ensured by high sensitivity of constructive interference condition to the lattice distance and the angle of incidence.

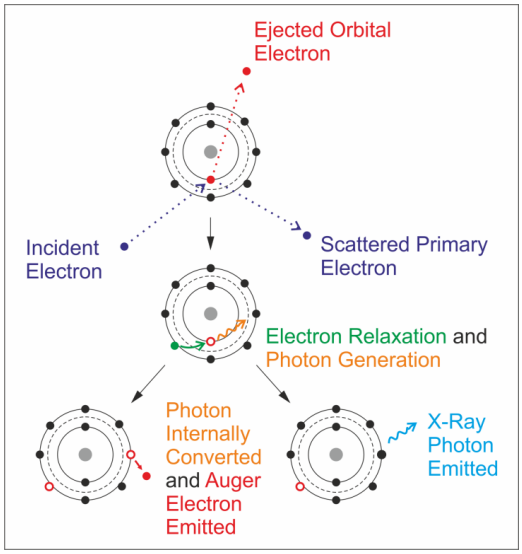

Figure 4.6. Atom excitation/de-excitation processes.

In the thin film EPMA analysis, standards of bulk materials are used for calibration of measured X-ray intensities. From the calibrated X-ray intensities (the so-called *k*-ratios), partial mass coverages of different elements are determined by solving the following equation:

$$k_i = \frac{I_i^{probe}}{I_i^{std}} = \frac{c_i^{probe}}{c_i^{std}} \cdot \rho \cdot d \cdot F_{corr}^{phys}\left(c_i^{probe}, d, c_{substrate}\right), \tag{4.4}$$

where c_i^{probe} and c_i^{std} are wt.% of element *i* in the measured layer and in the standard, and $c_{substrate}$ gives the chemical composition of the substrate material. The product of the layer thickness *d* and density ρ is equal to the total mass coverage of the layer on the substrate (in terms of µg/cm^2). The product

$$M_i = c_i^{probe} \cdot \rho \cdot d \tag{4.5}$$

represents then the partial mass coverage of the element *i*. The correction factor F_{corr}^{phys} depends on the chemical composition of the sample and the layer thickness. It considers different (material dependent) interaction of the electrons in the material, the absorption effects of the generated X-rays and other physical effects. Since this correction factor depends itself on the parameters of interest, the above equation can only be solved by an iterative procedure. The detectable partial mass coverage on a foreign substrate in the thin film EPMA analysis is about 0.02 µg/cm^2. For light elements such as carbon, the sensitivity of 0.05 wt.% is typically achieved.
In this work, EPMA measurements were done at the Central Facility for Electron Microscopy (Gemeinschaftslabor fuer Elektronenmikroskopie - GFE) at RWTH-Aachen [EPMA-Aachen].

Chapter 5. Exposures of diagnostic mirrors in tokamaks

5.1 Exposures under erosion conditions

In this section the performance of coated and SC mirrors made from ITER-candidate materials is investigated in the TEXTOR tokamak under erosion conditions to assess the applicability of the studied mirror concepts for ITER diagnostics. In addition, an exposure of a large SC mirror of 10 cm in diameter under the same conditions in TEXTOR was performed to study the mirror performance under particle fluxes varying over the mirror surface. The difference in the processes of physical sputtering of different mirror materials and their influence on the mirror reflectivity was described earlier in section 3.2.1. In this section, experiments performed at TEXTOR are described and the experimental results are presented.

5.1.1 Mirror characterization

For the experiments under erosion conditions, mirrors of different substrate materials coated with molybdenum (Mo) and rhodium (Rh) were studied along with SC Mo mirrors. Although Rh provides better reflectivity in the visible wavelength range [Palik], Mo is more favourable under erosion conditions due to its lower sputtering yield [Matsunami 1984]. Two sets of coated mirrors used in this study were produced at the University of Basel. Each mirror had a diameter of the polished area of 18 mm. Mirror set 1 included Rh and Mo coatings on Mo substrates deposited by the evaporation technique (Figure 5.1). Mirror set 2 consisted of Rh-coated tungsten (W) deposited by evaporation technique and Mo-coated Mo deposited by magnetron sputtering technique. For the sake of comparison, both sets of coated mirrors were extended with SC Mo mirrors produced by the active zone melting technique at FSUE SRI SIA "LUCH" in Russia. The Rh coating on W was selected for mirror set 2 as a more robust mirror concept for higher temperatures of the mirror surface since the first phase transition for a Rh-W system happens at a higher temperature (1880°C) as compared to a Rh-Mo system (830°C) [Shunk 1969], [Gurler 1991], [Brewer 1980]).The technology of manufacturing of the coatings is described in [Marot 2007], [Eren 2011], [Marot 2008]. As it was observed in the SEM analysis [Eren 2011], the coatings had a columnar structure, and molybdenum films produced by magnetron sputtering deposition at RT had a much denser surface compared to evaporation deposited mirrors. Such coatings are called nanocrystalline, since they consist of columnar grown grains which themselves consist of homogeneously dispersed nanocrystals with different orientations. The coating itself does not have a preferred orientation.

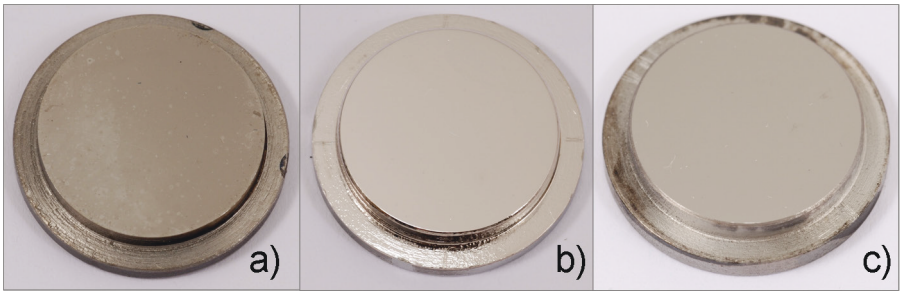

Figure 5.1. Photographic view of mirrors from set 1 before exposure: a) Mo coating on polycrystalline Mo substrate made by evaporation technique, b) Rh coating on polycrystalline Mo substrate made by evaporation technique, c) SC Mo mirror.

The large SC Mo mirror was manufactured at "LUCH". Among several manufactured mirrors with the diameter varying from 10 cm to 14 cm, a mirror with a diameter of 10 cm (Figure 5.3) was selected for the plasma exposure as compatible with the sample transport systems, so-called Limiter Locks [Schweer 2005], of TEXTOR.
Optical and surface characterization of all mirrors was performed before and after the exposure. Schemes of these measurements are shown in Figure 5.2 and Figure 5.3. The total and diffuse reflectivity of mirrors was measured with a spectrophotometer (section 4.7). For depth profiling and elemental surface composition measurements a SIMS facility was used (section 4.3). To measure the layer thicknesses, several SIMS craters were produced down to the substrate material and then scanned with a DEKTAK-6M stylus profiler. The elemental analysis and chemical characterization of the mirror samples were performed by XPS and the energy dispersive X-ray spectroscopy (EDX).

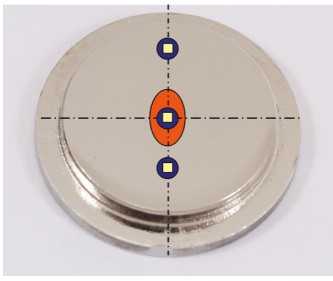

Figure 5.2. A photographic view of a diagnostic mirror. The oval spot in the middle of the sample indicates the location of measurements of the diffuse reflectivity, circles indicate the locations of measurements of the total reflectivity, small squares correspond to the locations of SIMS craters.

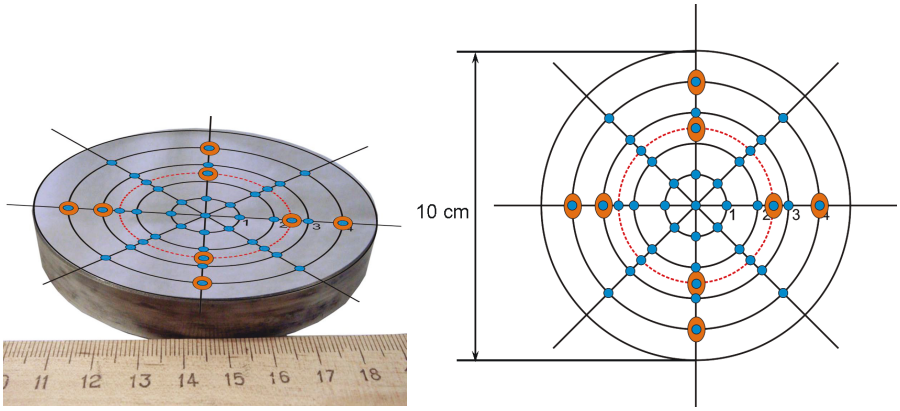

Figure 5.3. Photographic view of the large SC Mo mirror before exposure (left) and the scheme of performed reflectivity measurements (right). Large orange ellipses and small blue dots represent the positions of measurements of the diffuse and total reflectivity, respectively.

Due to considerable size and weight (~1200 g) of the large SC mirror, which were not compatible with the available SIMS facility, SIMS measurements for this mirror sample were not performed.

5.1.2 Exposures in TEXTOR

In total, three experiments were carried out, in which diagnostic mirrors were exposed for series of reproducible discharges in the scrape-off-layer (SOL) plasma of TEXTOR under ITER-relevant erosion-dominated conditions:

- a low-fluence exposure using mirror set 1;
- a high-fluence exposure using mirror set 2;
- an exposure of the large SC Mo mirror covering a large range of fluences.

For each experiment the corresponding mirror set was installed on a test limiter such that the plasma-exposed mirror surfaces were aligned with an angle of 20 degrees with respect to the toroidal direction (Figure 5.4). The test limiter was introduced into the SOL plasma of TEXTOR through the upper port using the limiter-lock transport system [Schweer 2005]. In the case of the low-fluence and high-fluence exposures the three mirrors of the corresponding mirror set were mounted side by side as indicated in Figure 5.5 to allow for direct comparison. In the case of the large SC Mo mirror a specially designed holder system was used to mount the mirror on the limiter head.

The hydrogen-deuterium (50 % H + 50 % D) plasma with neutral beam injection (NBI) heating and an assumed impurity content of 3 % for carbon (C) and 1 % for oxygen (O) [Ding 2010, Droste 2008, Pospieszczyk 1993] was used in all three cases. Edge plasma parameters were monitored with a supersonic helium beam diagnostics [Schmitz 2008, Kruezi 2012].

The low-fluence exposure was carried out to provide a direct comparison of the optical behaviour of mirrors based on different concepts. During the exposure the plasma parameters at the mirror centre averaged over the flat-top phase of all discharges were $n_e = 2.6 \times 10^{18}$ m^{-3}

and $T_e = 36$ eV (see section 6.1.1.). In total, 24 identical discharges were made with an NBI power of 1.4 MW. The total accumulated ion fluence to the centre of each mirror was estimated to be about 4.3×10^{24} ions/m^2. The surface temperature of mirrors during discharges was measured with an optical pyrometer and did not exceed 570°C.
The high-fluence exposure was performed to explore the limits of applicability of different mirror concepts. During the exposure the averaged plasma parameters near the mirror samples were $n_e = 3.6\times10^{18}$ m^{-3} and $T_e = 31$ eV (see section 6.1.1.). In total, 34 identical discharges were made with an NBI power of 1.0 MW. The total accumulated particle fluence to the center of each mirror was correspondingly estimated as 10.4×10^{24} ions/m^2, which is a factor 2.3 higher than in the low-fluence experiment. The peak surface temperature of the uppermost edge of the test limiter varied in the range of 670°C – 1250°C, which is due to variation of the edge plasma parameters from discharge to discharge.

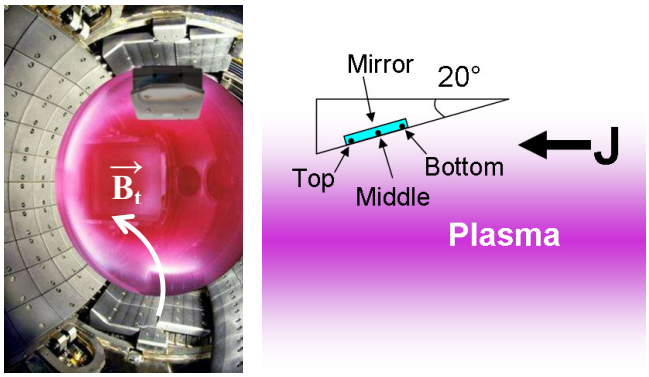

Figure 5.4. A scheme of exposure of mirrors installed on the roof-limiter in the SOL of TEXTOR (left) and an illustration of the geometry of the limiter with mirrors (right). J is the flux of impinging particles, which has the same direction as the toroidal magnetic field shown on the left picture. The mirror regions used for measurements are indicated as Top, Middle and Bottom.

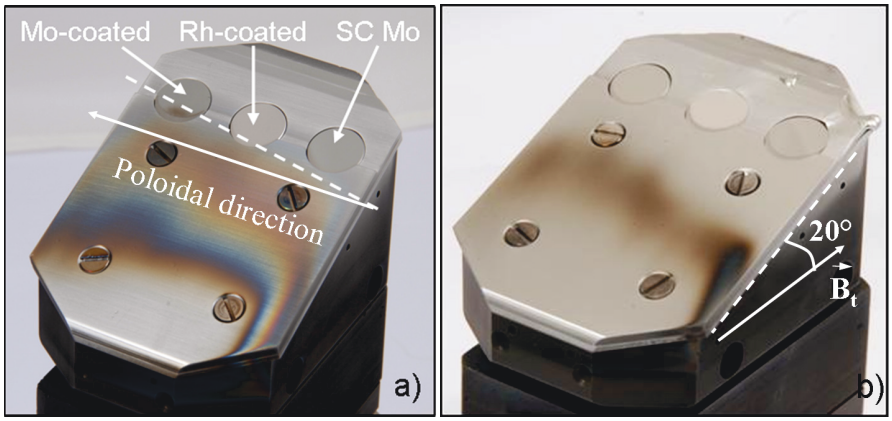

Figure 5.5. Test limiter with mirrors after exposures: a) low-fluence experiment: the boundary between the erosion-dominated and deposition-dominated zones on the test limiter is inclined with respect to the poloidal direction as it is indicated by the dashed line; b) high-fluence experiment (the mirrors are mounted in the same order as indicated in Figure 5.5a).

The exposure of a 10 cm large SC Mo mirror was performed in order to assess the quality of manufacturing and erosion behaviour of SC mirrors of ITER-relevant sizes. The mirror was exposed in the SOL of TEXTOR at a radial position of R=46.8 cm from the plasma center (position of the limiter tip, i.e. the most protruding part of the upper mounting clamp) for 37 identical discharges made with an NBI power of 1.2 MW. During the exposure, visual observations of the mirror using a high resolution camera were made. The temperature of mirror holders was controlled using thermocouples. The average plasma parameters at the center of the mirror were $n_e = 1.4\times10^{18}$ m^{-3} and $T_e = 14$ eV, while the mirror edge closest to the plasma experienced $n_e = 2.4\times10^{18}$ m^{-3} and $T_e = 20$ eV. The total accumulated particle fluence varied over the mirror surface from about 1.3×10^{24} ions/m at the lower part of the mirror surface, the most distant from plasma, to about 5.9×10^{24} ions/m^2 at the upper, plasma-closest part, respectively. The temperature of the mirror surface was controlled with a pyrometer. During the exposure the temperature did not exceed 400 °C at its hottest part. The test limiter head with the mirror and holders after the exposure is shown in the Figure 5.6.

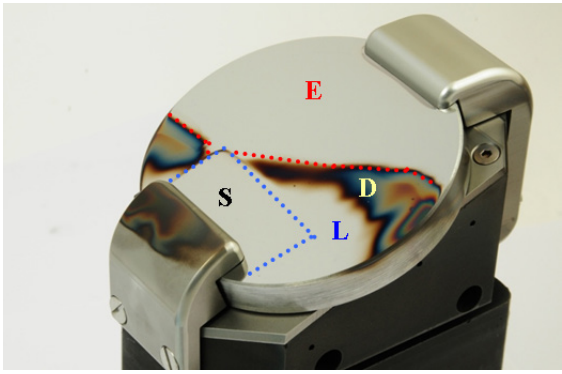

Figure 5.6. A photographic view of the large SC Mo mirror in the holder on the test limiter head after exposure in TEXTOR. The letters indicate the erosion zone (E), the deposition zone (D), the shadow from the mounting clamp (S), and the area of low deposition (L).

5.1.3 Results

5.1.3.1 Low-fluence exposure

Reflectivity measurements performed prior to the low-fluence exposure showed drastically reduced reflectivity of the Mo-coated mirror manufactured using the evaporation technique as compared to the reference data for Mo [Palik] (Figure 5.7 a). The surface of the mirror was investigated with an optical miscroscope and with SEM. Flaking of some regions of the coating was observed (Figure 5.8, Figure 5.9).

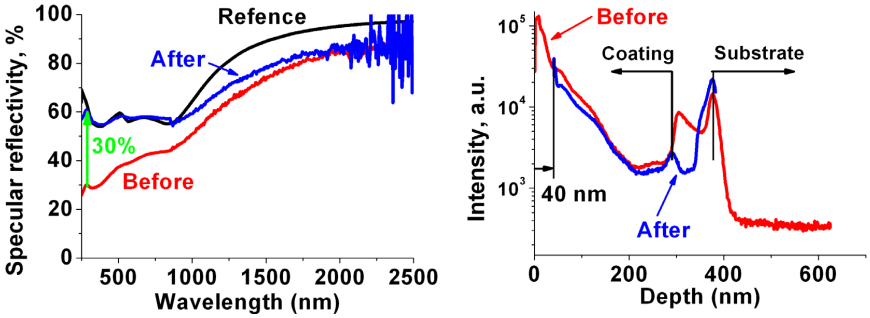

Figure 5.7. Optical and surface characterization of the Mo-coated mirror (evaporation technique) used for the low-fluence exposure: (a) the total reflectivity of the mirror before and after the exposure, the reference data according to [Palik]; (b) SIMS depth profiles illustrating the amount of oxygen in the most oxidized surface layer before and after the exposure. The noise on Figure 5.7a is attributed to the low intensity of the reflected light (at the sensitivity limit of the detector) due to measurements with a small spot.

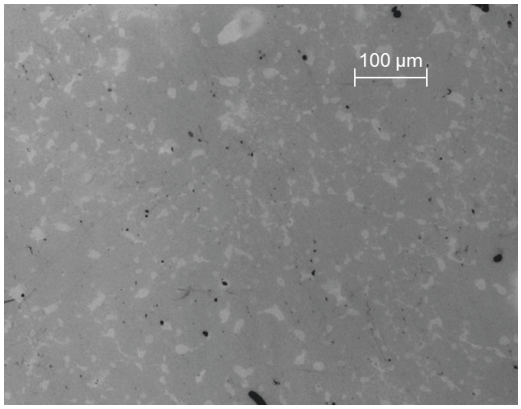

Figure 5.8. An image of the surface of the Mo-coated mirror produced by the evaporation technique. The photo was taken by the optical microscope before the exposure. Light spots indicate flaking of the coating from the substrate material.

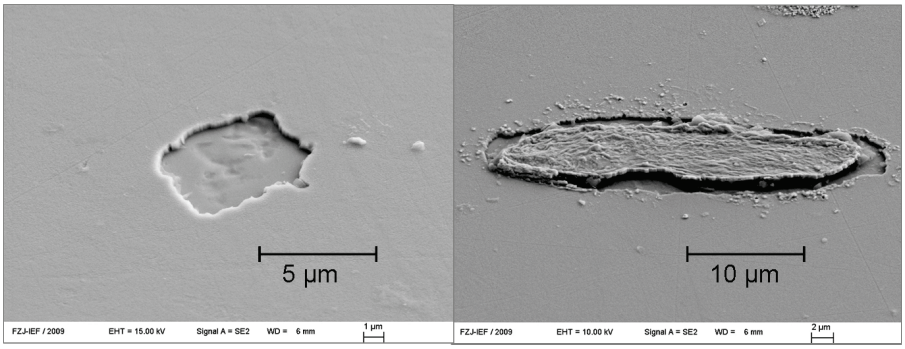

Figure 5.9. Flaking of the Mo coating (evaporation technique on Mo substrate) before the exposure as detected by SEM.

SIMS depth profiles of the Mo-coated mirror before and after exposure shown in Figure 5.7b indicate that the initially oxidized top layer of the Mo surface (see section 5.1.4.1 for a discussion) was eroded in the course of the experiment. As a result, the mirror reflectivity in the ultraviolet (UV) and visible (VIS) wavelength ranges was successfully restored (Figure 5.7a). The specular reflectivity, R_{spec}, at 1000 – 2500 nm remained about 5 % below the reference curve for Mo according to [Palik]. Similar trend in reflectivity changes was observed in the case of the SC Mo mirror (Figure 5.10): a recovery of R_{spec} due to removal of the oxidized surface layer was achieved in the UV and visible wavelength ranges, with only slight improvement in the range of 1000 – 2500 nm. Similar evolution of the reflectivity of Mo in the UV range was reported earlier for the case of consecutive cleaning of oxidized Mo mirrors using glow discharge plasmas [Litnovsky 2007b]. The reason for such a behaviour of optical characteristics of Mo mirrors in the infrared (IR) wavelength range will be discussed in section 5.1.4.3.

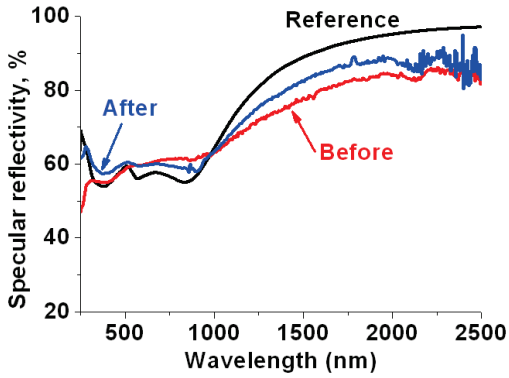

Figure 5.10. The specular reflectivity of SC Mo mirror before and after the low-fluence exposure (reference data according to the reference data according to [Palik].

Optical microscopy measurements of the Rh coating deposited on the Mo substrate using the evaporation technique performed before the exposure demonstrated that the surface was smooth except few observed droplets (Figure 5.11a,b). After the exposure, however, different types of defects were observed on the mirror surface (Figure 5.11c). The specular reflectivity of the mirror decreased after the exposure by up to 4 % at 250 – 500 nm for locations at the upper part of the mirror surface. For the mirror center, which was farther away from plasma, the corresponding change of R_{spec} was only 2.5%. Even smaller specular reflectivity changes were observed for the wavelength range of 500 – 2500 nm (Figure 5.12a). Such changes in R_{spec} are mostly caused by corresponding increase of the diffuse reflectivity, R_{diff}, at 250 – 1000 nm (Figure 5.12b).

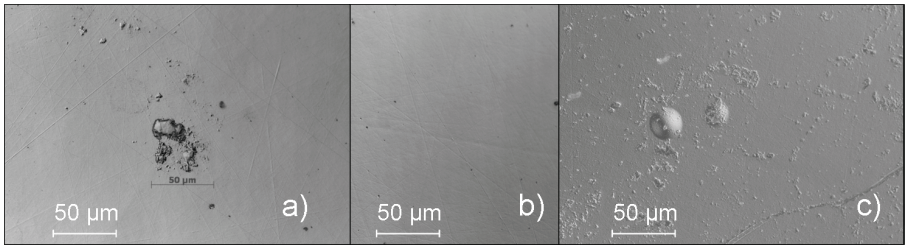

Figure 5.11. Photos of the surface of the Rh-coated mirror on Mo substrate taken by the optical microscope: a) an example of droplets on the mirror surface before the exposure, b) the mirror surface in the droplet-free region before the exposure, c) defects on the surface observed after the low fluence exposure.

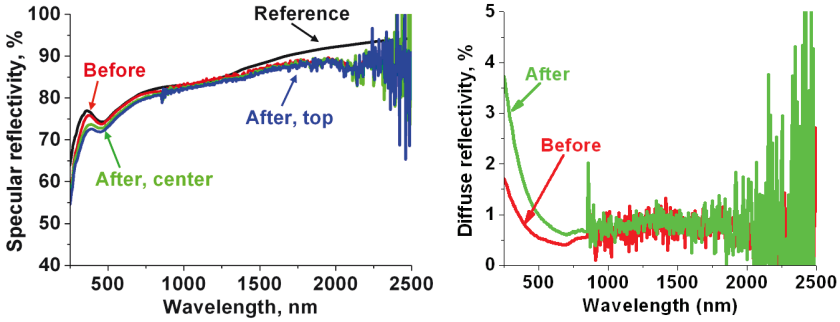

Figure 5.12. Specular reflectivity (a) and diffuse reflectivity (b) of Rh-coated mirror before and after the low-fluence exposure (reference data according to [Palik]). The top area of the mirror was sputtered by 190 nm, the central area – by 100 nm.

In general, in the low-fluence exposure all mirror samples demonstrated acceptable performance with the maximal drop of the total reflectivity not exceeding 4 % in the wavelength range of 250 – 2500 nm. The Mo- and Rh-coated mirrors were sputtered by about $d_{exp\ Mo}$ = 40 nm and $d_{exp\ Rh}$ = 100 nm, as measured in the center of each mirror. The amount of sputtered material for the SC Mo mirror could not be measured since SC material is uniform and the mirror had no marker layer for reference.

5.1.3.2 High-fluence exposure

The Mo coating prepared by the magnetron sputtering technique was stable and not oxidized before the high-fluence exposure (Figure 5.13 a). The mirror demonstrated good performance after erosion of 120 nm (in the center) by incoming particles. The surface remained smooth except for few small regions with surface defects (Figure 5.13 b, c). The diffuse reflectivity increased up to 2.5 % at 250 nm being around 1 % in the wavelength range of 500 – 2500 nm. The specular reflectivity decreased by 4 % in the range of 1000 – 2500 nm and by up to 12 % in the range of 250 – 600 nm (Figure 5.14).

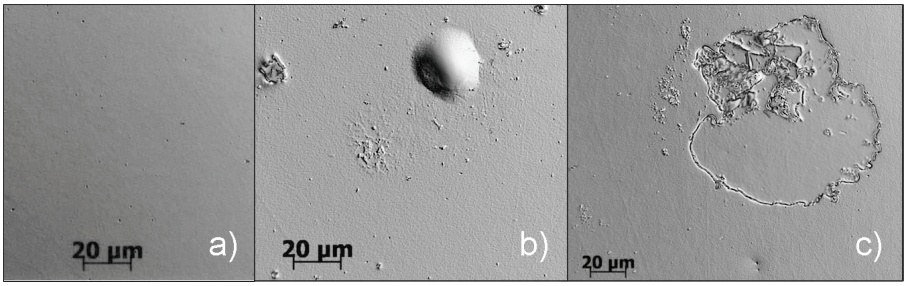

Figure 5.13. Optical microscopy images of the surface of the Mo-coated mirror: before (a) and after (b, c) the high-fluence exposure. After the exposure, defects and flaking of the mirror surface can be observed.

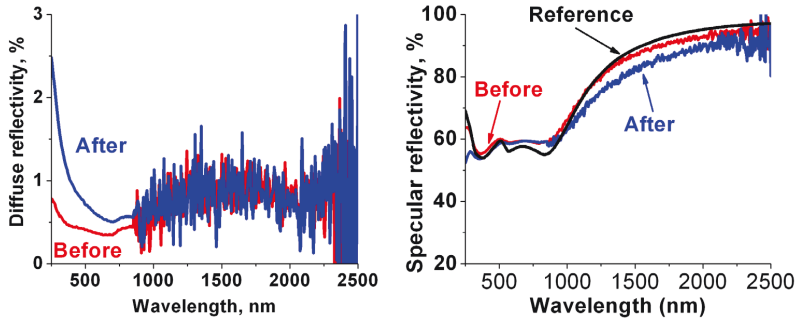

Figure 5.14. The diffuse (a) and specular (b) reflectivity of the Mo-coated mirror before and after the high-fluence exposure (reference data according to [Palik]).

The Rh coating on W (evaporation technique) had an initial surface roughness of about 20 nm (Figure 5.15a). The mirror had many traces of flaking on the surface already before the exposure (Figure 5.15b,c and Figure 5.16a). The density of flaked regions with sizes larger than 10 μm was about 120 per 100 mm^2. EDX measurements showed that flaking of the Rh coating (a layer of 1 μm thickness) occurred down to the very substrate. The total area of flakes, however, was well below 1 % of the exposed mirror surface. At such a concentration, flakes should not affect the reflectivity measurements.

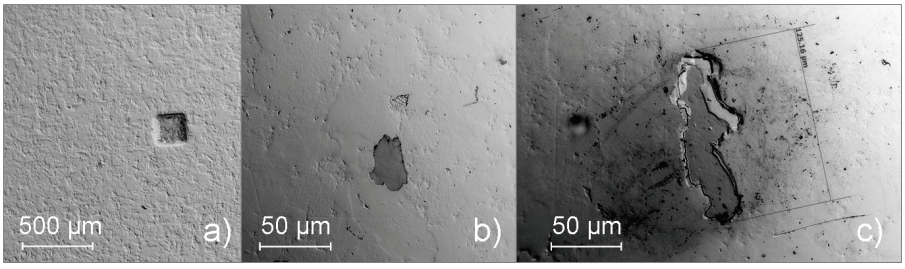

Figure 5.15. Photos of the Rh coating made by the evaporation technique on W substrate showing the rough mirror surface with developed structures (a) and flaking of the coating from the substrate (b and c). The photos were taken by the optical microscope before the exposure.

During exposure, the Rh-coated mirror was eroded by 340 nm in its center. From SEM images of the mirror surface (Figure 5.17) an increase of the grain size after the exposure can be seen. Such an increase is attributed to re-crystallization of Rh, which occurred due to the high temperatures reached during discharges (chapter 5.1.2) (the recrystallization temperature of Rh is about 983°C [Marot 2013]). As a result, the roughness of the mirror surface increased accordingly (Figure 5.16b). Profilometry measurements showed that the root mean square roughness, σ, has increased from about 21 nm to about 29 nm. The development of a surface relief and respective increase of R_{dif} of the mirror (Figure 5.18 a) correspondingly led to a drop of the intensity of the specular reflected light by about 25 % in the UV wavelength range (Figure 5.18b).

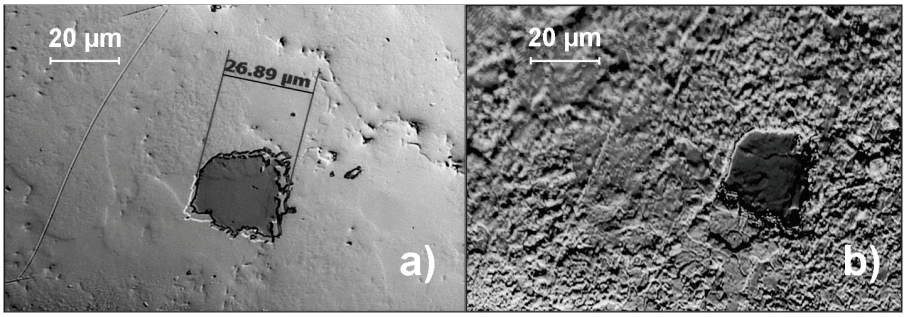

Figure 5.16. Photos of the surface of the Rh-coated mirror on W substrate taken by the optical microscope: a) selected flaked spot on the mirror surface before the exposure and b) an increase of the surface roughness at the same location after the high fluence exposure.

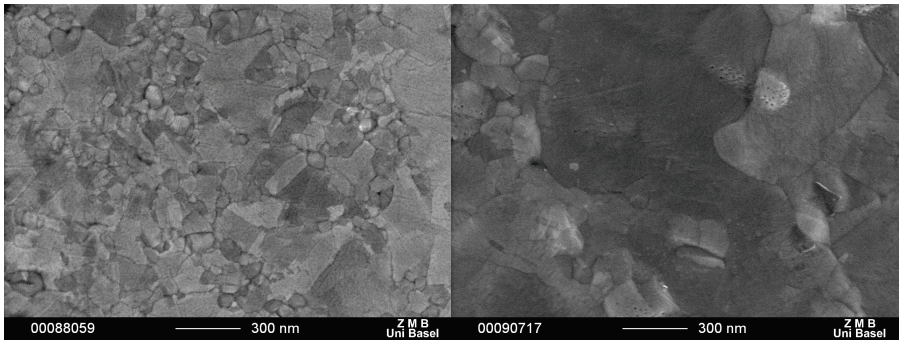

Figure 5.17. SEM images of the Rh coating showing the crystallite size before (a) and after (b) the high-fluence exposure.

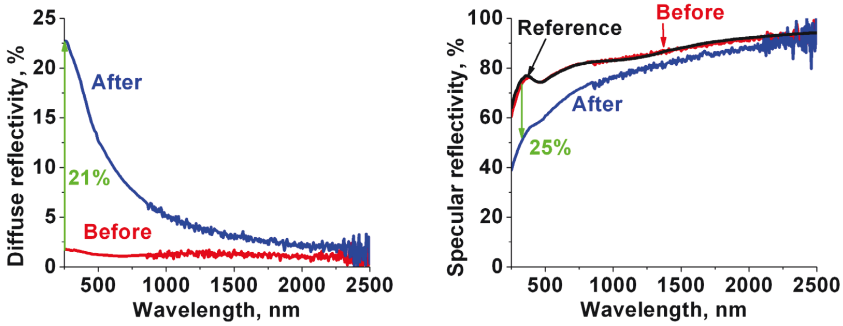

Figure 5.18. The diffuse (a) and specular (b) reflectivity of the Rh-coated mirror before and after the high-fluence exposure (reference data according to [Palik])

The SC Mo mirror demonstrated a very good performance. The diffuse reflectivity of the mirror remained very low (~ 1 %) after the exposure. The surface roughness was preserved at a level of ~ 2 nm, same as it was before the exposure, thus confirming the homogeneous sputtering of the entire mirror surface. The specular reflectivity of the mirror decreased by 4 % in the IR wavelength range (Figure 5.19), alike for all studied SC Mo and Mo-coated mirrors regardless of the amount of eroded material.

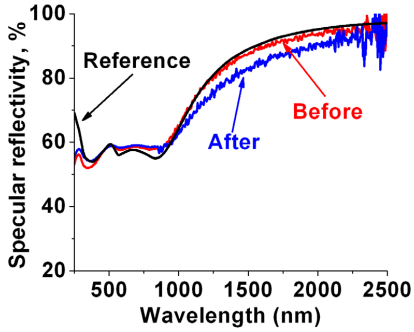

Figure 5.19. The specular reflectivity of the SC Mo mirror before and after the high-fluence exposure (reference data according to [Palik]).

5.1.3.3 Exposure with flux variation over the mirror surface

Mechanical shaping procedures produce defects in SC materials. Ongoing R&D in the Kurchatov Institute in Russia show that the amount of such defects in SC mirrors can be significantly reduced by annealing [Litnovsky 2007b, RF ITER 2005]. At the same time, polishing of a SC mirror with diamond pastes brings some carbon contamination and thus may stimulate carbide formation on the mirror surface when it is heated after the polishing procedure. Therefore it is preferential to perform annealing before polishing.

It was decided to perform annealing of the selected large SC Mo mirror on the stage between mirror shaping and polishing. Since the temperature of annealing should be kept below the temperature of re-crystallization of the mirror material to ensure minimal effect of this procedure on the SC microstructure, annealing of the selected mirror sample was done at a temperature of 1000-1200^{o}C, while the spontaneous grain growth leading to severe degradation of the material strength and hardness occurs in industrially produced Mo at temperatures of 1600^{o}C - 1800^{o}C. The mirror sample was annealed for 2-3 hours under vacuum conditions to avoid surface oxidation, which may lead to a degradation of the mirror reflectivity.

After the mirror was produced, it was stored for about 6 months in atmosphere. During the air storage, the reflectivity of the mirror did not degrade much as compared to the handbook data [Palik] (Figure 5.21). Nevertheless, to ensure the best possible mirror performance, it was decided to clean the mirror surface using plasma sputtering, the technique expected to be used for cleaning of diagnostic mirrors in ITER.

For the oxide removal a capacitively coupled parallel plate discharge in Ar in the PADOS laboratory facility was used (see Figure 5.20). The upper electrode was grounded, and the lower electrode was powered by a 13.56 MHz radio-frequency generator, operated to provide a constant self-bias voltage, evolving due to the ambipolar plasma flux. The sample was

placed on the powered electrode. In this case just one 20 min long exposure was sufficient to remove the oxidized layer. Optical measurements made on the mirror after cleaning showed R_{spec} values very close to those from the handbook (Figure 5.21).

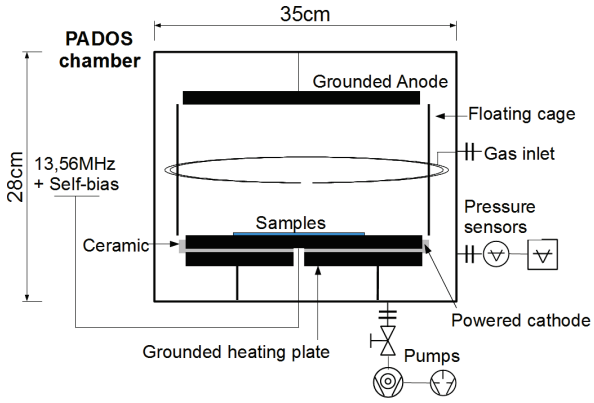

Figure 5.20. The scheme of the vacuum chamber of PADOS, in which the cleaning of the large SC Mo mirror with Ar plasma was performed [Moeller PhD thesis]

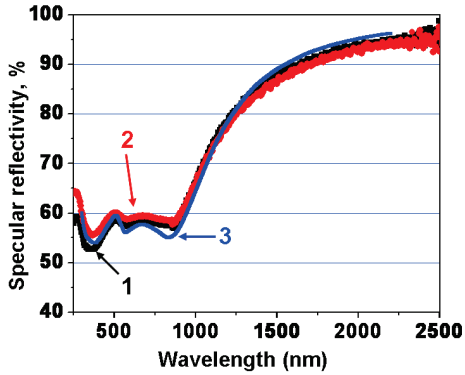

Figure 5.21. Wavelength dependence of the specular reflectivity of the large SC Mo mirror: 1) after the storage in air (before plasma cleaning); 2) after plasma cleaning; 3) handbook data for Mo [Palik].

To evaluate further the quality of the mirror surface and the uniformity of the surface roughness over the entire area, measurements of the diffuse reflectivity were performed. The scheme of these measurements is provided in Figure 5.22a, and the results are shown in Figure 5.22b. Diffuse reflectivity was measured to be below 2% in the studied wavelength range of 250 – 2250 nm, similar over the entire mirror surface. These measurements, coupled with subsequent stylus profiling of the mirror surface, demonstrate a high surface quality of the manufactured mirror with a uniform roughness over the entire surface.

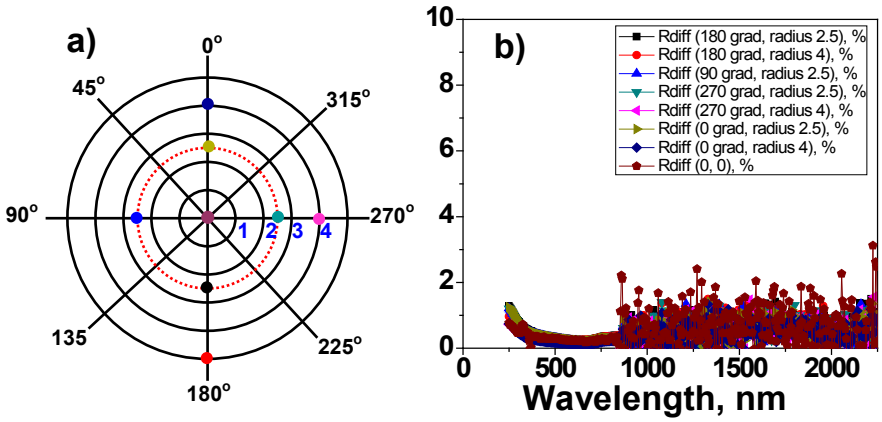

Figure 5.22. The diffuse reflectivity (b) of the large SC Mo mirror measured at various locations of the mirror surface (a) prior to exposure in TEXTOR.

During the exposure in TEXTOR various areas of the large SC Mo mirror were subjected to different plasma fluxes. As a result, a part of the mirror surface appeared to be in the deposition-dominated zone (area D in Figure 5.6, Figure 5.23a), interrupted by area S representing the shadow cast on the limiter by the lower protective clamp. The small trace of deposition visible on the upper part of the mirror surface was most likely produced by the upper protective clamp, which served as a source for reflected and eroded particles, in a full similarity with earlier observations [Litnovsky 2007b]. Area L is the zone of net deposition, which is just too low to be visible. The remaining part of the mirror surface represents an erosion-dominated zone (area E in Figure 5.6, Figure 5.23a) and provides sufficient opportunities for the evaluation of reflectivity changes over a large area due to erosion under different plasma fluences.

The reflectivity measurements of the large SC Mo mirror were made before and after the exposure at multiple locations on the mirror surface on all characteristic areas of the exposed mirror. In the following only several examples of measurements done in the erosion-dominated zone (area E in Figure 5.23a) will be demonstrated. Six various locations in the erosion zone were selected for the comparison. The corresponding scheme of R_{spec} measurements is shown in Figure 5.23a with the results provided in Figure 5.23b. Generally, the reflectivity of the exposed mirror remained the same in the wavelength range of 270 – 1000 nm and slightly dropped by about 5-7% at 250 nm and by about 4% in the range of 1000 – 2500 nm. These results reproduce the typical behaviour of SC Mo mirrors under erosion conditions discussed in the previous two sections.

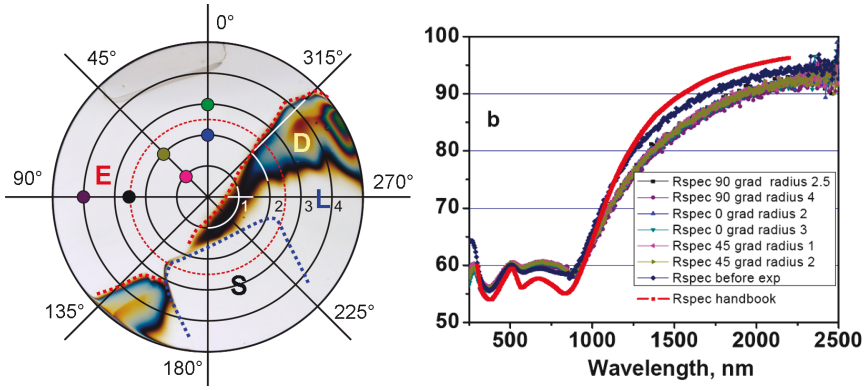

Figure 5.23. Locations of reflectivity measurements on the large SC Mo mirror (a) and the specular reflectivity measured after the exposure in TEXTOR compared to the pre-exposure data (b) (handbook data according to [Palik]).

Measurements shown in Figure 5.23 (b) correspond to parts of the mirror surface that were located at different distances from plasma (see Figure 5.4 and Figure 5.23 (a)). Due to a radial dependence of the fluxes of particles in the SOL, effectively this means different erosion conditions at these locations (Table 5.1).

Table 5.1. Ion fluences at various locations used for reflectivity measurements.

	Fluence, $x10^{24}$ ion/m^2			
Radius (cm)	**0°**	**45°**	**90°**	**135°**
0.0	2.82			
1.0	3.36	3.33	3.00	2.61
2.0	3.99	3.94	3.20	2.41
2.5	4.35	4.29	3.30	2.32
3.0	4.75	4.66	3.41	2.23
4.0	5.65	5.51	3.63	2.06

Results of experiments described in the section 5.1 are summarized in Table 5.2 and Figure 5.24 where the specular reflectivity of all studied mirrors at different wavelengths is shown as a function of the ion fluence accumulated by the mirror surface. A very strong decrease of R_{spec} of the Rh-coated mirror can be seen at the wavelengths of 250, 300, 400, and 600 nm. Among all studied SC Mo and Mo-coated mirrors, the most pronounced decrease of the reflectivity by 12% and 5.5% occurred for Mo-coated mirrors at the wavelengts of 250 nm and 300 nm respectively. At 2000 nm all Mo mirrors experienced a slight reflectivity decrease by about 3-4%.

Table 5.2. Summary of conditions and results of erosion experiments.

		Low-fluence exposure			High-fluence exposure			Large SC Mo
		Rh coating on Mo	Mo coating on Mo	SC Mo	Rh coating on W	Mo coating on Mo (Ti interlayer)	SC Mo	Erosion-dominated zone
Technique		evaporation	evaporation	active zone melting	evaporation	magnetron sputtering	active zone melting	active zone melting
Plasma parameters		Calculated at the mirror center position: $n_e = 2.6\times10^{18}$ m^{-3} $T_e = 36$ eV			Calculated at the mirror center position: $n_e = 3.6\times10^{18}$ m^{-3} $T_e = 31$ eV			$n_{e(center)}=1.42\times10^{18}$ m^{-3} $n_{e(range)}= 1.08-2.37\times10^{18}$ m^{-3} $T_{e(center)}=13.6$ eV $T_{e(range)} =10.7 - 19.5$ eV
Total fluence, $\times10^{24}$ iom/m^2		4.3			10.1			$\Gamma(0;0)=2.82$ Range: 2.23 – 5.90
Maximal surface temperature of uppermost edge of limiter		570°C			1250°C			400°C
State of the mirror	Before exposure	Flat mirror surface	strong oxidation, flaking	oxidation	strong flaking	Flat mirror surface	Flat mirror surface	Flat mirror surface
	After exposure	Defects	flaking	Flat mirror surface	strong flaking, roughening	defects and flaking	Flat mirror surface	Flat mirror surface
Sputtered material, nm	center	100	40	–	340	122	–	–
	top	190	67	–	416	155	–	–
Reflectivity changes UV: at 250 nm IR: at 2000 nm	R_{diff}	UV: ⇗ by 2%	no changes	no changes	UV: ⇗ by 21%	UV: ⇗ by 1.7%	no changes	no changes
	R_{spec}	UV: ⇘ by 2.5% IR: OK	UV: ⇗ by 25% IR: 9% below reference	IR: 5% below reference	UV: ⇘ by 25% IR: ⇘ by 2%	UV: ⇘ by 12% IR: ⇘ by 3.5%	IR: ⇘ by 4%	IR: ⇘ by up to 3%
Roughness, nm	Before				21	7.5	–	–
	After				29	9.3	3.2	–

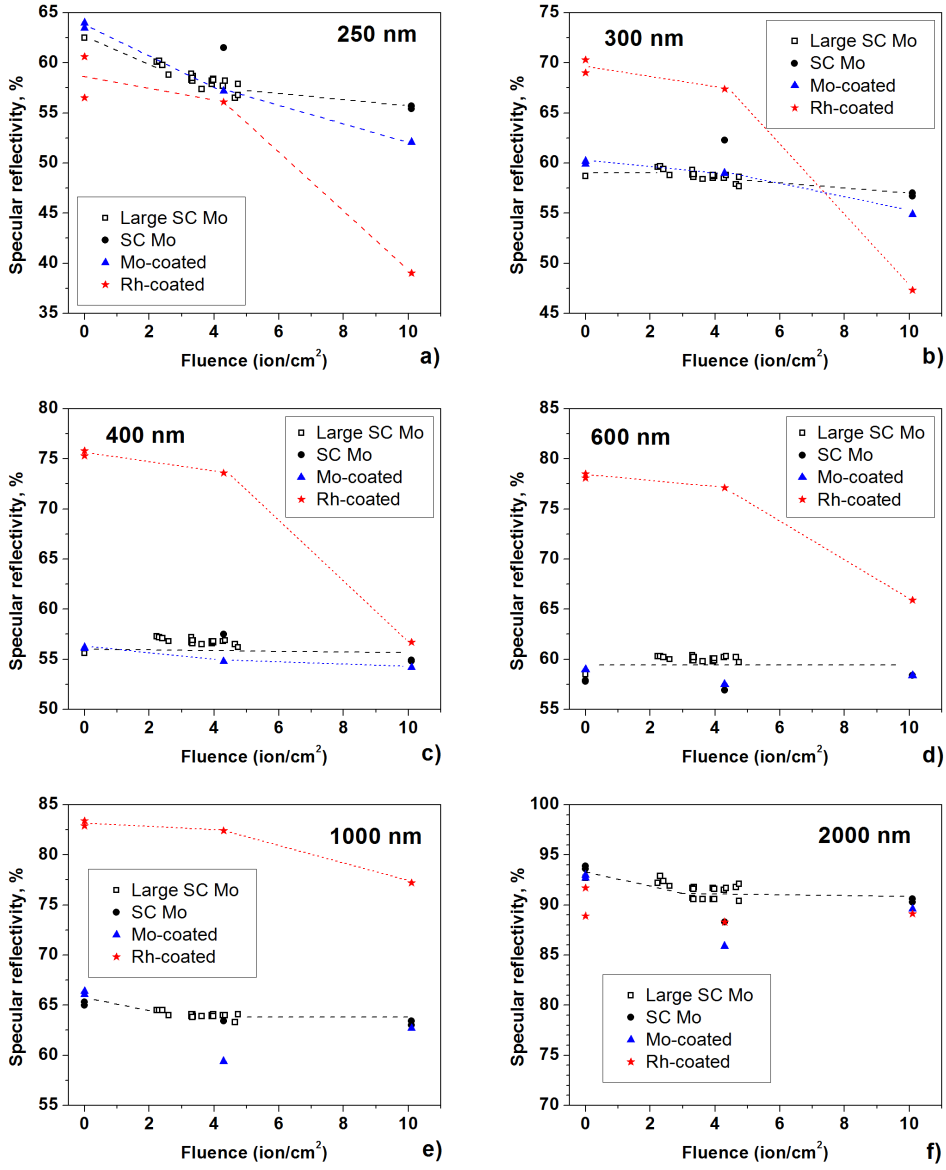

Figure 5.24. The specular reflectivity of SC Mo, Mo-coated and Rh-coated mirrors used in TEXTOR experiments as a function of the ion fluence accumulated by the mirror surface. Results are shown for wavelengths of the probing light equal to 250, 300, 400, 600, 1000 nm, and 2000 nm. Lines between the experimental data points are drawn to guide the eye.

5.2 Exposures under deposition-dominated conditions: gas feeding

The influence of deposited layers on the mirror reflectivity was described in section 3.2.1. The possibility to suppress impurity deposition on the mirror surface and thus to preserve the mirror properties by a gas puff in the vicinity of the mirror surface is discussed in this thesis. In this section experiments performed under net deposition conditions in TEXTOR employing deuterium and helium gas injection are described and experimental results are presented. The influence of the gas injection on the flow of plasma and impurity particles towards the mirror surface is analysed with a one-dimentional SOL model (Section 6.1.2.). Physical processes leading to deposition suppression in the case of different injected gases are discussed.

5.2.1 Scheme of experiments and mirror characterization

A periscope-like system with mirrors located inside tubes was built to investigate the particle transport in diagnostic ducts and to test techniques for mitigation of material deposition on diagnostic mirrors [Wienhold 2005]. The Periscope mirror system in TEXTOR, further referred as the Periscope, simulates light guides in diagnostic ports transmitting the plasma radiation to distant mirrors and sensors in a fusion reactor. For experiments, the Periscope was introduced into the SOL plasma of TEXTOR through the upper port using the limiter-lock transport system as it is shown in Figure 5.25. Some details on the system are shown in Figure 5.26. All circular openings on the front surface of the Periscope, except for the lowest one, are non-through holes made to decrease the weight of the system. The apperture of 35 mm in diameter is oriented perpendicular to the toroidal direction. Two plane mirrors are placed at marked locations inside the Periscope duct at a distance of 275 mm being oriented perpendicular to each other such that SOL fluxes hit the first mirror at an angle of 45°. For the pilot experiment mirrors made from TZM (99% Mo, 0.1% Zr, 0.5% Ti) were used. For later experiments they were replaced with PC Mo mirrors representing one of the main candidate materials for diagnostic mirrors in ITER. An additional mirror was installed at the location of the end plate. The entire system can be heated up to temperatures of 550 – 600°C using internal heaters. The bulk temperature of the Periscope can be measured by means of built-in thermocouples. The Periscope duct walls can be equipped with exchangeable foils for studies of impurity transport towards the mirrors. The entire system is dismountable allowing for post-mortem analysis of deposited impurity layers on the surfaces of mirrors.

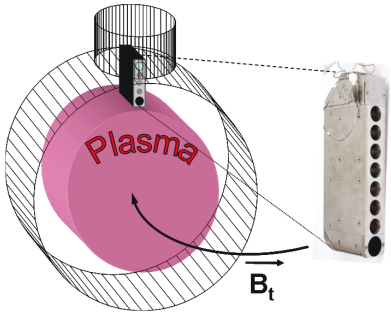

Figure 5.25. Scheme of exposure of the Periscope mirror system in the SOL plasma of TEXTOR.

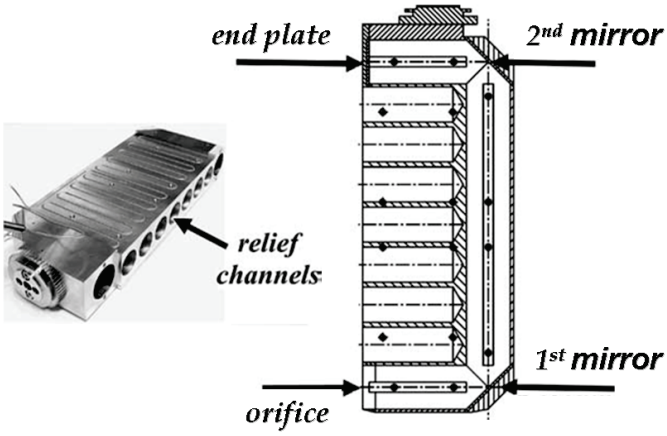

Figure 5.26. The Periscope mirror system. Mirror 1 is the closest to the plasma. The photograph on the left shows the stainless steel body without the end plate. Relief channels represent non-through holes and are intended to reduce the weight of the system [Wienhold 2005].

Optical and surface characterization of all mirrors was performed before and after exposures in TEXTOR. Schemes of these measurements depend on the observed deposition patterns and are therefore different for different experiments. Optical characteristics such as the total and the diffuse reflectivity, and the reflectivity of the polarized light were made using the single beam spectrophotometer Varian Cary 5 and the spectroscopic ellipsometer SENTECH SE850 at the University of Basel. The most recent experiments with He and D_2 gas feeding were analysed using the double-beam spectrophotometer Perkin Elmer Lambda 950 (section 4.7) and the spectroscopic ellipsometer SENTECH SenResearch SE800E (section 4.8) at the MirrorLab [MirrorLab] at Forschungszentrum Juelich (FZJ). For elemental surface composition analysis and depth profiling, double-beam ToF-SIMS measurements (section 4.3) were combined with the stylus profilometry (section 4.4). To calculate layer thicknesses, the sputter rates of SIMS were estimated by measuring the depth of SIMS calibration craters done till the substrate with a stylus profiler. Thicknesses and composition of deposits were cross-checked with EPMA (section 4.9). As an example, schemes of measurements of pre-deposited mirrors after the exposure in TEXTOR with He and D_2 gas feeding are shown in Figure 5.27.

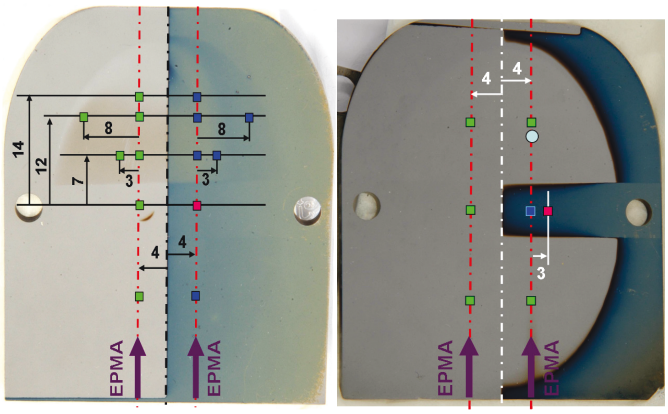

Figure 5.27. A photographic view of 1st mirrors after exposures in TEXTOR with He and D_2 gas feeding. The distances are indicated in mm. Small squares correspond to locations of SIMS craters. The measurements of R_{dif} and R_{tot} were done at the same locations as SIMS craters. The direction of EPMA line scans (red dash-dotted lines) is shown with arrows.

5.2.2 Exposures in TEXTOR

Several experiments with the Periscope mirror system were performed in TEXTOR on a step-by-step basis.

During the first, pilot experiment described in [Wienhold 2005] the system was exposed in a passive regime to NBI-heated, ohmic and electron cyclotron resonance heated (ECRH) discharges with a total plasma duration of about 1050 s. The plasma-closest edge of the Periscope was kept at a position of 25 mm away from the LCFS. The central line average plasma density was $n_{eo} = 1.5 – 4.5 \times 10^{19}$ m^{-3}. The temperature of the system was 150°C. The plasma fluence averaged over the aperture of the Periscope towards the first mirror, i.e. the one facing the plasma, was estimated to be 4.5×10^{20} particle/cm^2.

In the second experiment, NBI and ohmic heating was applied, and the total plasma duration was about 500 s. As a follow up of the campaign with heated mirrors in DIII-D where a moderate increase of the mirror temperature up to 165°C led to the complete suppression of carbon deposition [Litnovsky 2008, Rudakov 2006], the entire Periscope with mirrors was heated up to temperatures of ~390 – 420°C. Such heating was applied to get the maximum advantage from thermally intensified chemical erosion of carbon deposits by hydrogenic atoms and ions, which has under TEXTOR conditions a temperature maximum at about 500°C [Vietzke 1987a, Philipps 2003].

During the third experiment the deuterium gas was blown into the Periscope as it is illustrated in Figure 5.28. This was done in addition to heating of the system in order to increase the source of chemically reactive D atoms and possibly detach the plasma from the mirror surface [Litnovsky 2009]. In total, 44 identical repetitive high-power NBI-heated discharges with total plasma duration of ~240 s were done. The averaged fluence over the aperture of the Periscope was about 1.2×10^{20} ion/cm^2. The D_2 gas was blown into the periscope at an almost constant rate of ~5.2×10^{19} D_2/s.

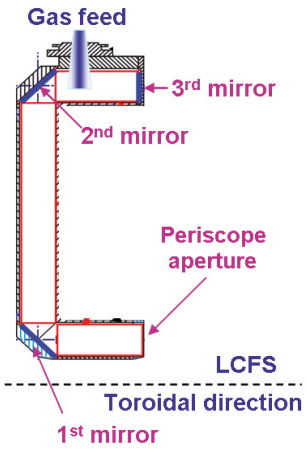

Figure 5.28. A scheme of the Periscope mirror system with gas feeding in the vicinity of mirrors.

The last experiments with the Periscope were done to clarify the physics of deposition mitigation by gas feeding. The two questions that were investigated are the following [Matveeva 2011]:

- Is gas feeding able to clean the mirrors, or does it only keep the mirror protected from deposition of impurities?
- Is deposition mitigation/cleaning attributed solely to chemical erosion, or does the contribution of physical sputtering play a role?

To answer the above questions two experiments were performed, in which non-reactive He and chemically reactive D_2 gases were fed, correspondingly, at a rate of about 1.63×10^{19} s^{-1} for He and 5.63×10^{19} s^{-1} for D_2. Hydrogen-deuterium plasmas (50% H + 50% D) with an assumed impurity content of about 3% for carbon and about 1% for oxygen [Ding 2010, Droste 2008, Pospieszczyk 1993] were used, i.e. similar to plasmas used in experiments described in section 5.1. The central line averaged plasma density was $n_{e0} = 3 - 5 \times 10^{13}$ cm^{-3} with the toroidal field $B_t = 2.25$ T and the plasma current $I_p = 350$ kA. Edge plasma parameters were monitored with the supersonic helium beam diagnostics. Averaged plasma parameters at the center of the Periscope aperture were $n_e = 1.5 \times 10^{12}$ cm^{-3} and $T_e = 25$ eV so that the plasma fluence to the mirror surface averaged over the Periscope aperture was about 5.2×10^{20} ion/cm^2 for the case of He feeding and about 9.1×10^{20} ion/cm^2 for the case of D feeding (see section 6.1.1). During the experiments the bulk temperature of the Periscope was kept at about 370 – 390°C. Two identical sets of mirrors were used for both experiments, each consisting of three PC Mo mirrors. A half of each mirror was pre-coated in the laboratory with a 100 nm thick a-C:D film. A photograph of one of the 1st mirrors after the laboratory deposition and prior to exposure in TEXTOR is shown in Figure 5.31a. A horizontal stripe in the middle of the mirror was covered with an aluminium bar in order to protect this part of the mirror from erosion and deposition during the exposure.

5.2.3 Results

After the first experiment, when the Periscope system was exposed without pre-heating and without gas feeding, the 1st mirror showed a radially decaying deposition (Figure 5.29 (left)). The maximum deposit thickness estimated by the interference fringe analysis was about 0.5 μm. EPMA measurements confirmed this estimate and showed that the deposit consisted mainly of carbon. Such a layer thickness corresponds to a deposition rate of about 0.4 nm/s. Although this high deposition rate on the 1st mirror surface, no detectable deposition was observed neither on the subsequent mirrors deeper in the duct nor on the duct walls.
After the second experiment where the heated Periscope was exposed without gas feeding, the 1st mirror was significantly contaminated. The photo of this mirror after the exposure is shown in Figure 5.29 (right). The deposition pattern is clearly visible. Ellipsometric measurements showed that amorphous carbon deposits with a thickness of 410 nm were formed on the mirror surface, which agrees well with results of the interference fringe analyses. The total reflectivity of the mirror decreased significantly reaching the value of 12% at the wavelength of 250 nm.

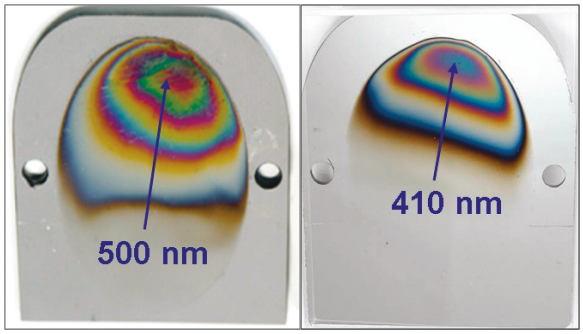

Figure 5.29. Photographic views of 1st mirrors after Periscope exposures without gas feeding without (left) and with (right) heating up to ~400°C with thick deposits visible on the upper part of the surface.

After the third exposure involving, in addition to heating, the D_2 gas feeding no visible deposition was observed on surfaces of all three mirrors. Photographs of the first, plasma-facing mirror before and after the exposure are shown in Figure 5.30. The mirror looked shiny without any trace of deposition. The mirror surface analyses did not detect any presence of impurities on the mirror surface. Moreover, optical measurements showed only negligible changes in the optical reflectivity of the exposed mirror (Figure 5.30 c).

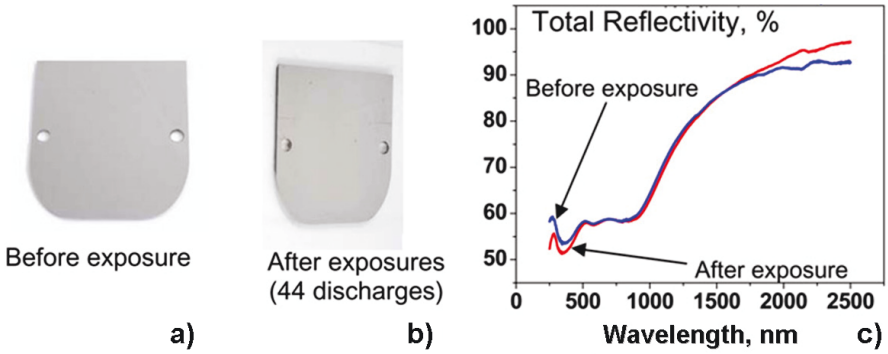

Figure 5.30. Photographic views of the 1st mirror before (a) and after (b) exposure of the Periscope system with the D_2 gas feeding, and the evolution of the total reflectivity of the mirror before and after the exposure as measured at the centre of the mirror (c) [Litnovsky 2009].

In the last exposure, in which helium feeding was applied, deposition on the surface of the 1st mirror was significantly suppressed, although not enough to protect the mirror surface completely. As a result, the initially clean part of the mirror surface was covered with a 12 nm thick deposited layer causing a decrease of the mirror reflectivity (Figure 5.31 b, Figure 5.32 a). A similar layer growth was observed on the pre-deposited part of the mirror surface: the layer thickness at the upper part of the mirror increased by about 11 nm. According to EPMA measurements, the layer thickness on the pre-deposited half of the mirror increased by 11 nm on the upper part of the mirror (Figure 5.33) and remained the same on the lower part.
After the exposure with the D_2 gas feeding the full suppression of deposition and even the complete removal of the pre-deposited a-C:D film was achieved on the 1st mirror surface (Figure 5.31 c). The specular reflectivity of the mirror was restored to its initial values (Figure 5.32 b) being similar on pre-deposited and non-deposited parts of the mirror. The EPMA analysis confirmed the absence of deposition on the pre-deposited half of the mirror, except for the part protected by the aluminium bar during the exposure in TEXTOR. As for the second and the third mirrors, no changes of surface and optical characteristics were detected in all experiments that were carried out with the Periscope mirror system.

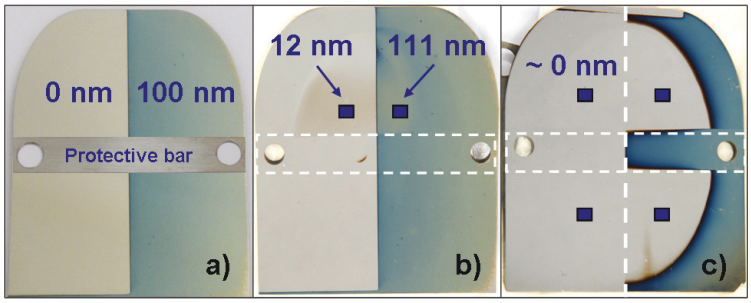

Figure 5.31. Photographic views of 1st mirrors: a) before gas puff exposures with one half of the mirror surface pre-deposited in the laboratory; b) after the exposure with the He gas feeding, showing slight deposition on both halves of the mirror surface; and c) after the exposure with the D_2 gas feeding showing deposit removal from the pre-deposited half of the mirror surface.

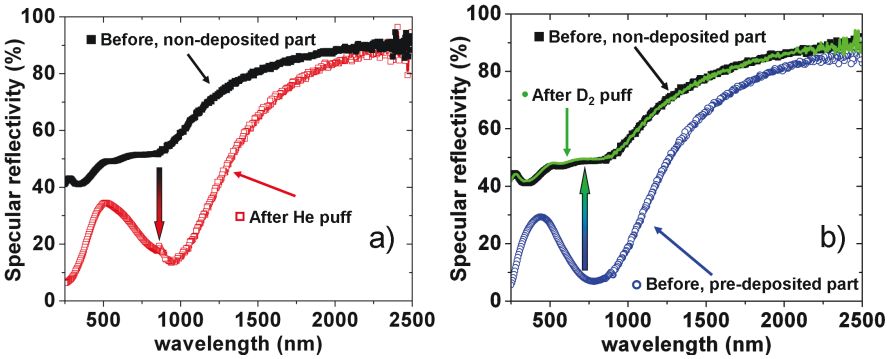

Figure 5.32. The specular reflectivity of 1st mirrors before and after exposures with gas feeding: a) He feeding, measurement in the region above the protective bar, initially without deposition; b) D_2 feeding, measurement in the initially pre-deposited region.

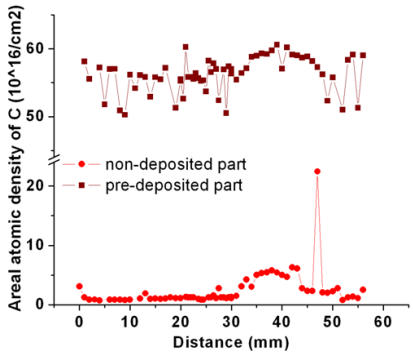

Figure 5.33. Profiles of the areal atomic density of carbon measured by EPMA on non-deposited and pre-deposited parts of the 1st mirror after the exposure with the He gas feeding. The distance is counted from the lower part of the mirror as shown in Figure 5.31 b. The increase of the areal density at a distance of about 30-50 mm corresponds to the regions with slight deposition accumulated during the exposure.

In addition to measurements of the specular reflectivity of mirrors, the reflectivity of the parallel and perpendicularly polarized light was measured after the exposures. Exemplary reflectivity curves measured at an incident angle of the probing light of 45° are presented in Figure 5.34, Figure 5.35, Figure 5.36 and Figure 5.37. In particular, Figure 5.34 shows that the reflectivity of the parallel polarized light after the exposure with the D_2 gas feeding is almost similar for all locations, and that there is practically no difference between the pre-deposited areas cleaned during the exposure (locations #1 and #5) and initially clean areas where deposition was mitigated by the gas feeding (locations #2 and #6). The same holds for the reflectivity of the perpendicularly polarized light (Figure 5.35) in this experiment.

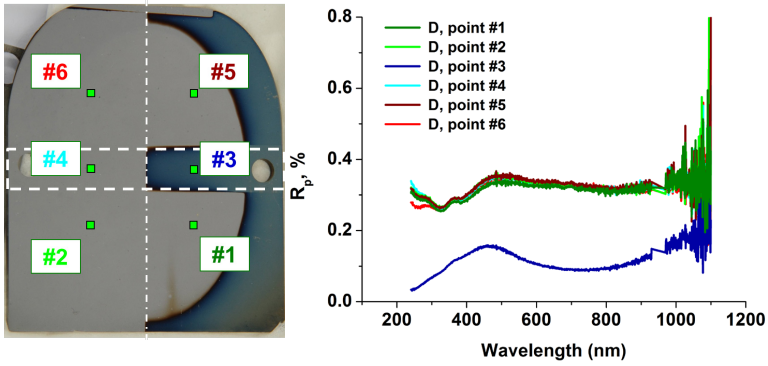

Figure 5.34. Locations of measurements of the reflectivity of the polarized light for the 1st mirror after the exposure with the D_2 gas feeding (left), and the reflectivity of the parallel polarized light measured at a 45° incidence (right).

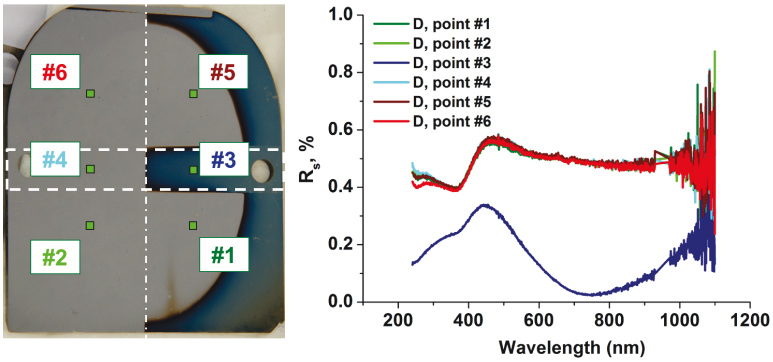

Figure 5.35. Locations of measurements of the reflectivity of the polarized light for the 1st mirror after the exposure with the D_2 gas feeding (left), and the reflectivity of the perpendicularly polarized light measured at a 45° incidence (right).

Figure 5.36 shows the reflectivity of the parallel polarized light for the first mirror after the exposure with the He feeding. The reflectivity curves are almost similar for locations #1, #3 and #5, which all correspond to the pre-deposited zone. Locations #1 and #3 were exposed to plasma and location #3 was protected during the exposure. The reflectivity at location #5 differs slightly from the other two due to the layer thickness increased after the exposure. The reflectivity of the parallel polarized light at point #6, in turn, decreased significantly due to deposition of a thin carbon layer, since the initial mirror surface was absolutely clean from deposition. Figure 5.37 illustrates the same behaviour of the reflectivity of the perpendicularly polarized light after this experiment.

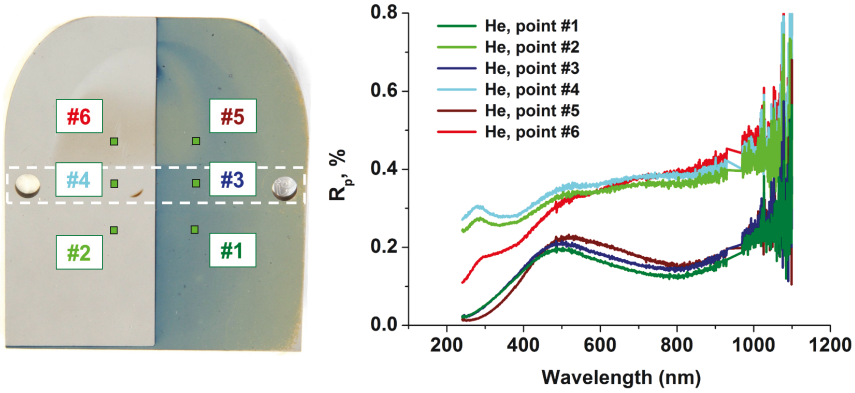

Figure 5.36. Locations of measurements of the reflectivity of the polarized light for the 1st mirror after the exposure with the He gas feeding (left), and the reflectivity of the parallel polarized light measured at a 45° incidence (right).

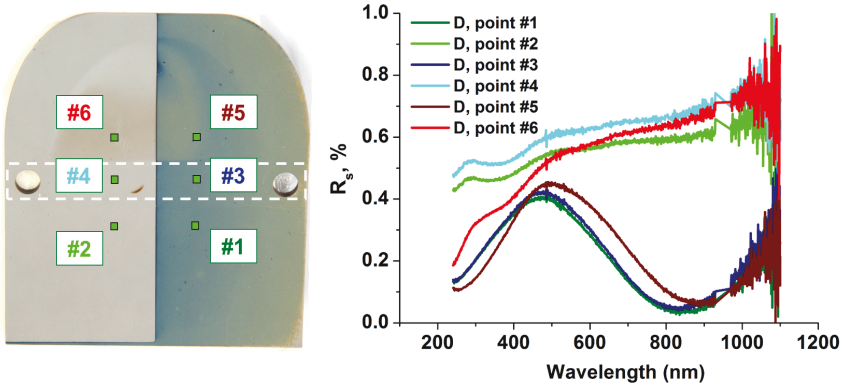

Figure 5.37. Locations of measurements of the reflectivity of the polarized light for the 1st mirror after the exposure with the He gas feeding (left), and the reflectivity of the perpendicularly polarized light measured at a 45° incidence (right).

5.3 Exposure in oxygen-rich atmosphere

5.3.1 The thermo-oxidation process

Oxygen is known to be very reactive, especially at elevated temperatures, so that carbon is readily eroded by oxygen chemically [Haasz 1996, Philipps 1999, Hu 2006]. There can be several possible sources of an oxygen influx at a material surface in a fusion device:

- Intrinsic impurity in plasma;
- Accidental air ingress;
- Wall conditioning in an oxygen-rich atmosphere.

Thermo-oxidative wall conditioning represents a very effective tool for removal of hydrogenated carbon films [Davis 2009]. It has been extensively tested in laboratory experiments [Davis 2009, Tsui 2008, Haasz 2007] and successfully applied as a wall conditioning technique in several tokamaks [Philipps 1999, Hu 2006, Allen 2010]. Thermo-oxidation was considered as a technique for de-tritiation of carbon-based co-deposits in ITER. On the other hand, surface oxidation represents a strong change of the surface composition and therefore may be expected to affect the optical characteristics of the material.
Incidental effects of thermo-oxidation on a wide variety of tokamak components were investigated in laboratory experiments [Fitzpatrick 2010]. The impact of thermo-oxidation on optical properties of diagnostic mirrors was not addressed in those studies and represents the main focus of the work described below.

5.3.2 Exposure of mirrors in DIII-D

Four copper and six PC molybdenum mirror samples were installed in the DIII-D tokamak (see Figure 5.39) and exposed during a thermo-oxidation experiment [Allen 2010]. Three PC Mo mirrors were initially clean, while the other three were pre-deposited with a-C:D layers with layer thicknesses of about 38 nm, 60 nm and 60 nm, respectively. Coated mirrors were used to check the possibility of removal of deposited carbon layers from the mirror surface by means of thermo-oxidation. Cu mirrors were not coated.

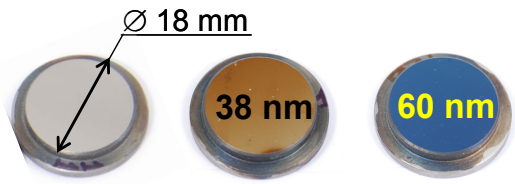

Figure 5.38. Polycrystalline Mo mirrors used for the thermo-oxidation experiment in DIII-D. From left to right: an initially clean mirror, a mirror with a 38 nm thick a-C:D coating, and a mirror with a 60 nm thick a-C:D coating deposited in the laboratory.

Pre-characterization of mirrors performed at FZJ before the exposure included measurements of the total and diffuse reflectivity, determination of optical constants by means of spectroscopic ellipsometry, SIMS measurements of the surface elemental composition, and

stylus surface profiling. To avoid surface oxidation during transportation, mirrors were delivered to DIII-D sealed in Ar.
Out of ten mirrors in total, four were placed directly in the main chamber by insertion on a stalk, other four were installed on a flange set back from the vessel wall, the remaining one Cu and one Mo mirrors were mounted on the DiMES manipulator system [Wong 1998] in the divertor. A schematic view of mirror positioning and mounting is given in Figure 5.39.
During the thermo-oxidation experiment, the vacuum vessel of DIII-D was pre-heated to a temperature of about 350°C and filled with the 80 % He and 20 % O_2 gas mixture with a nominal pressure of 1.27 kPa. As a result, mirrors placed in the main chamber and on the DiMES manipulator reached the baking temperature of 350°C, whereas the temperature of mirrors mounted on the remote flange became established at about 160°C. After two hours of oxygen exposure, the vacuum vessel was evacuated and allowed to cool down to room temperature. After the experiment, all mirrors were transported back to FZJ for post-exposure analyses. Results of the mirror analyses were published in [Litnovsky 2012] and are summarized in the next section.

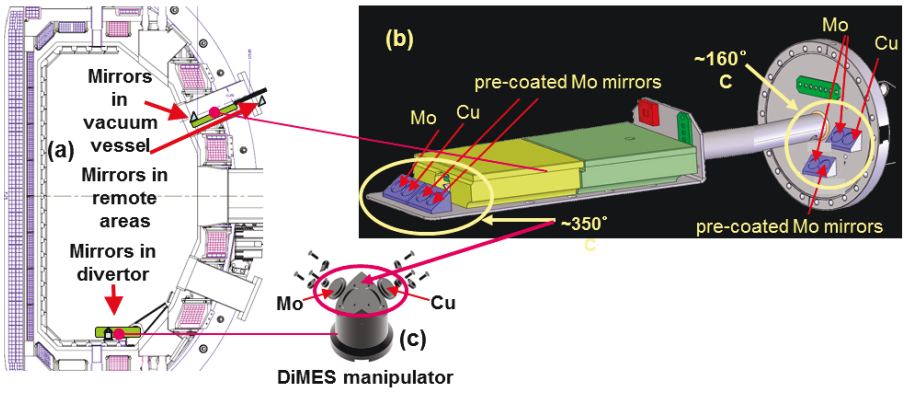

Figure 5.39. Cross-section of the DIII-D tokamak showing an overview of mirror installation locations (a); four mirrors installed on a stalk and other four on flange (b); the DiMES manipulator with one Cu and one Mo mirrors (c).

5.3.3 Results

This section is organized as follows. First the results for initially clean Mo and Cu mirrors are presented in sub-sections 5.1.3.1 and 5.1.3.2. The analysis of pre-deposited Mo mirrors is given in sub-section 5.1.3.3. Finally, the effect of the mirror storage on air is discussed in sub-section 5.1.3.4.

5.3.3.1 Molybdenum mirrors

From first visual observations, a slightly brownish tint on initially clean Mo mirrors exposed at 350°C could be distinguished after the experiment, although it was noticeable only in a direct comparison with grey-metallic and shiny non-exposed surfaces (e.g. inside SIMS craters). Reflectivity and SIMS measurements were performed at several locations on all Mo mirrors; particular results are shown in Figure 5.40. For the initially clean mirror exposed at 160°C, a slight drop of the specular reflectivity was detected in the UV wavelength range

(Figure 5.40a). The maximal decrease the reflectivity of about 10% was measured. SIMS measurements (Figure 5.40b) indicate the presence of about 4 nm thick layer of oxygen intermixed with molybdenum on the surface. In contrast, the reflectivity of mirrors exposed at 350°C degraded drastically in the UV and VIS wavelength ranges (Figure 5.40c). The maximal decrease of the reflectivity was above 50%. The corresponding resulting oxidized layer thickness was 19 nm according to SIMS and profilometry measurements (Figure 5.40d). A minor carbon contamination detected on exposed Mo mirrors corresponds to less than 1/100 of the intensity usually observed during tokamak exposures and therefore is assumed to cause no noticeable change of the reflectivity.

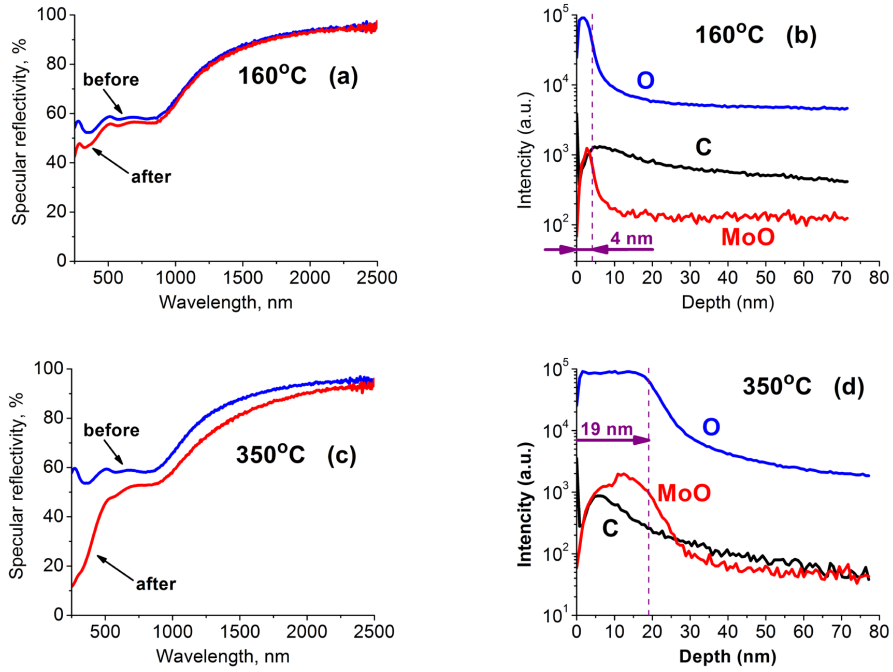

Figure 5.40. The specular reflectivity as a function of the wavelength (a and c) and SIMS elemental composition depth profiles (b and d) of initially clean Mo mirrors exposed in DIII-D at temperatures of 160 °C (remote) and 350 °C (main chamber), respectively. Mirrors installed in the main chamber and in the divertor showed very similar results.

5.3.3.2 Copper mirrors

The copper mirrors, initially shiny, experienced a visible darkening of the surface and become barely reflecting (Figure 5.41c). The darkening of the surface was stronger for mirrors exposed at the higher temperature (350°C versus 160°C). Reflectivity and SIMS measurements were performed at several locations on all Cu mirrors; particular results are shown in Figure 5.41. Even in the case of the mirror exposed at 160°C the reflectivity drop was significant and reached about 20% at a wavelength of 600 nm (Figure 5.41a). The simultaneous presence of copper and oxygen on the surface was detected from SIMS depth profiling, indicating the oxidation process and a diffusive mechanism of oxygen penetration

into copper (Figure 5.41b). The thickness of the most affected layer was estimated to be about 13 nm. For mirrors exposed at 350°C, the reflectivity drop reached a drastic value of about 90% at the wavelength of 850 nm (Figure 5.41d). SIMS investigations (Figure 5.41e) indicated the presence of a much thicker (~100 nm) oxidized layer. Mirrors installed in the main chamber and in the divertor showed very similar results.

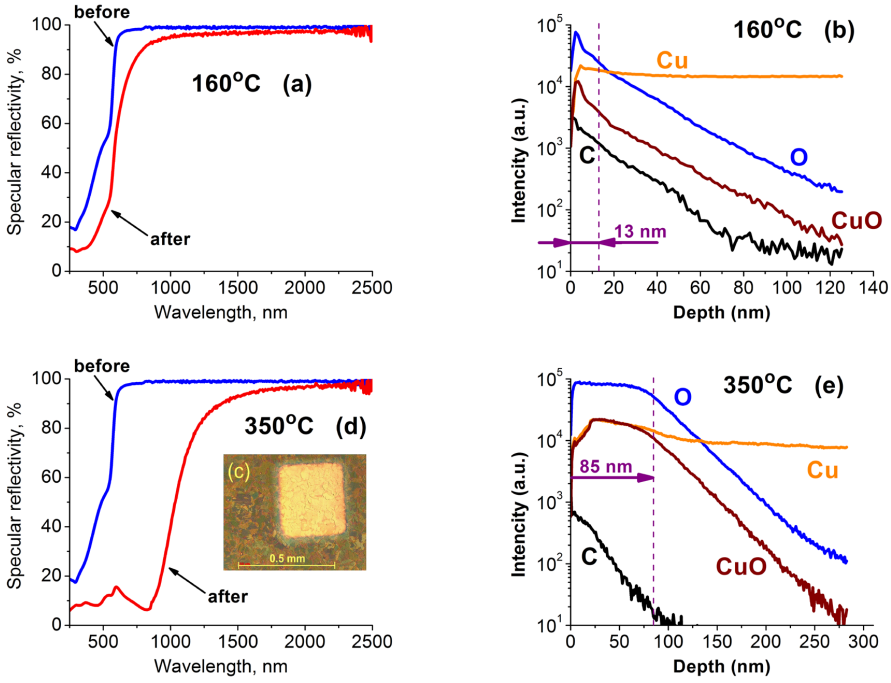

Figure 5.41. The specular reflectivity as a function of the wavelength (a and c) and SIMS elemental composition depth profiles (b and d) of Cu mirrors exposed in DIII-D at temperatures of 160°C (remote) and 350°C (main chamber), respectively.
The insert (c) shows a view on a SIMS crater on the surface of a Cu mirror after exposure at 350°C. The lighter color represents the SIMS sputtered region, i.e. corresponds to the initial state fo the mirror surface.

5.3.3.3 Pre-deposited mirrors

The reflectivity and the surface composition of pre-coated mirrors changed negligibly after the oxygen exposure (see Figure 5.42). Since the reflectivity of an a-C:D coated surface is very sensitive to the layer thickness (Figure 3.5), no changes of the pre-deposited layer thickness can be expected. However, SIMS measurements indicated an increase and broadening of the oxygen signal at the interface between the a-C:D layer and the Mo substrate, which was stronger in the case of the higher mirror temperature. This effect will be discussed in section 6.3.2.3.

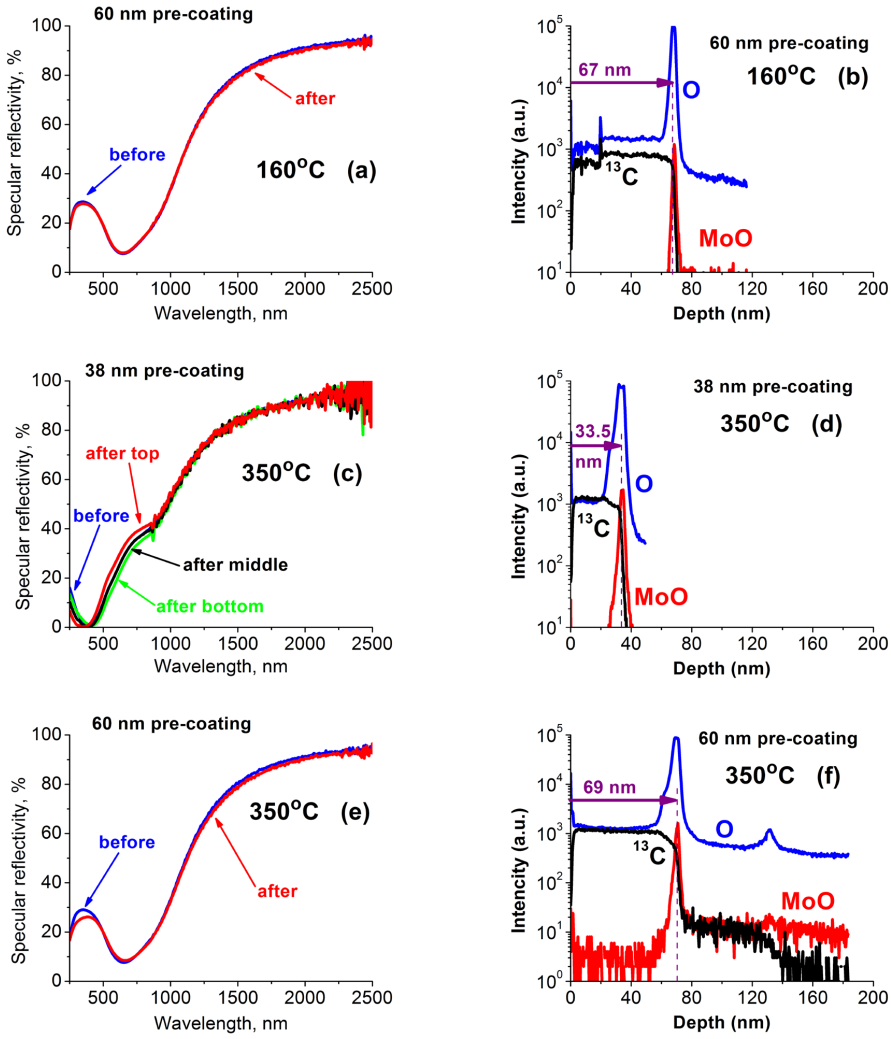

Figure 5.42. The specular reflectivity as a function of the wavelength (left) and SIMS elemental composition depth profiles (right) of the pre-coated Mo mirrors exposed in DIII-D at temperatures of 160°C (a and b – remote location, 60 nm coating) and 350°C (c and d – main chamber, 38 nm coating; e and f - main chamber, 60 nm coating).

Figure 5.43 illustrates the possible change in the thickness of the pre-coated layer with initial thickness of 38 nm after the oxygen exposure. The derived difference of the layer thickness before and after exposure is about 3 - 4 nm, which is within the 20% uncertainty of the method. Thus, no evident change of the layer thickness after the exposure could be stated.

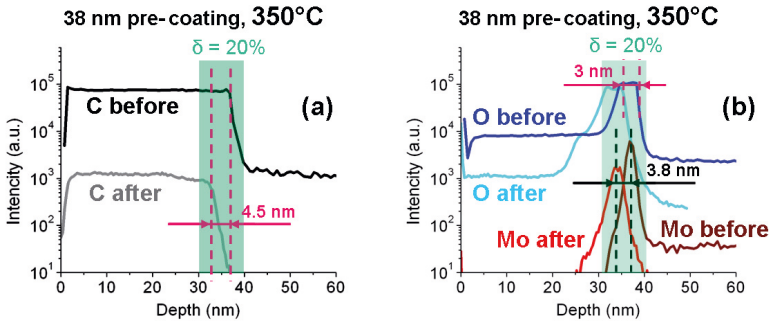

Figure 5.43. SIMS depth profiles of carbon (a) and oxygen (b) for the pre-coated Mo mirror with the initial layer thickness of 38 nm. Measured before and after the thermo-oxidation experiment in DIII-D where the mirror was positioned in the main chamber at 350°C are shown. The uncertainty of the method (δ=20%) is shown by a light green backgroun in the figures.

5.3.3.4 Effect of mirror storage on air

To investigate the effect of storage of mirrors on air, a clean Mo mirror from the same manufactured set as the mirrors used for the thermo-oxidation experiment in DIII-D was exposed to the atmosphere for about half a year. As it can be seen from Figure 5.44, the reflectivity of the mirror did not show any noticeable change. In such a way, the observed changes of the reflectivity reported for mirrors exposed in DIII-D can be unambiguously attributed to the effect of thermo-oxidation during the experiment.

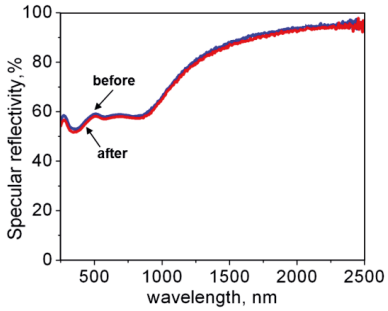

Figure 5.44. Dependence of the specular reflectivity on wavelength measured for the polycrystalline molybdenum mirror before air storage and after air storage for six months.

Chapter 6. Plasma induced surface modification and its influence on the reflectivity of diagnostic mirrors: results and analyses

6.1 Evaluation of plasma parameters and particle fluxes

6.1.1 Parameters of background plasma

During exposures of diagnostic mirrors in TEXTOR, the edge plasma parameters were monitored with the supersonic helium beam diagnostics [Schmitz 2008]. The average plasma parameters at the position of the mirrors were then estimated from measurements of the electron density n_e and the electron temperature T_e during the flat-top phase of each discharge. As an example of this procedure, the radial profiles of n_e and T_e measured by the diagnostics in different discharges of the low-fluence exposure are shown in (Figure 6.1). Grey dots illustrate the scatter of the data measured in different discharges, and the black lines indicate simple averaging over all discharges. The standard deviation of measurements performed during different discharges was taken as a measure of uncertainty of experimental determination of plasma parameters, which is thus indicated with red and blue lines in the figure. From the average radial profiles of n_e and T_e, accounting for the radial position and geometry of the test limiter with the mirror holder, plasma parameters at the center of each mirror were calculated. For the plasma conditions corresponding to mirror experiments in TEXTOR with NBI heating applied, the ion temperature is approximately twice as large as T_e [Huber 2000].
The ion flux reaching a plasma-exposed surface is proportional to the plasma density and temperature:

$$\Gamma = \frac{1}{2} n_0 \sqrt{\frac{k(T_e+\gamma T_i)}{m_i}}, \tag{6.1}$$

where n_0 is the plasma density at the so-called stagnation point where the plasma flow velocity is zero. Adiabatic constant γ=5/3 is assumed, corresponding to an adiabatic flow with isotropic pressure [Stangeby 2000].
The radial profiles of the ion density and temperature in the SOL can be described by exponential decay functions as

$$n_i = n_e = n_{e0} \times e^{-\frac{x}{\lambda_n}}; \tag{6.2}$$

$$T_\mathrm{i} = T_{i0} \times e^{-\frac{x}{\lambda_T}}, \tag{6.3}$$

where plasma parameters at the LCFS, n_{e0} and T_{i0}, and the decay lengths λ_n and λ_T can be derived from experimental measurements of n_e and T_e.

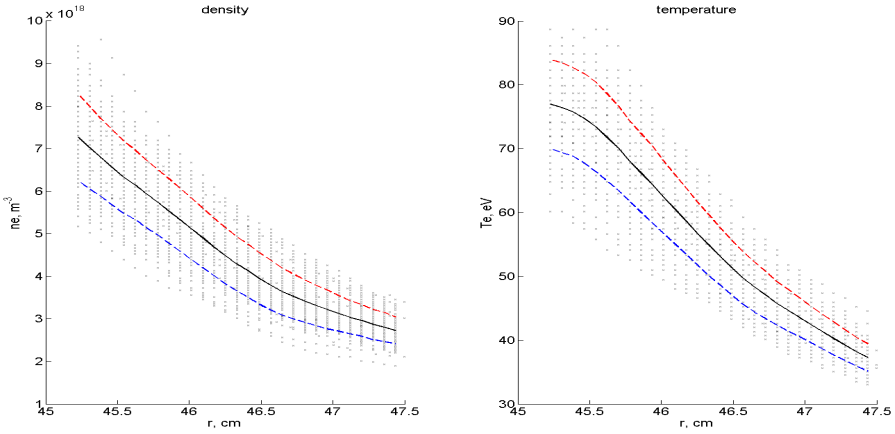

Figure 6.1. Radial profiles of plasma density and temperature in the TEXTOR edge measured with the supersonic helium beam diagnostics during the low-fluence exposure under erosion conditions.

In such a way, the ion flux can be written in the following form:

$$\Gamma = \text{const} \times e^{-\frac{x(\lambda_n+2\lambda_T)}{2\lambda_T\lambda_n}}, \tag{6.4}$$

from which the ion flux decay length can be derived:

$$\lambda_\Gamma = \frac{2\lambda_T\lambda_n}{2\lambda_T+\lambda_n}. \tag{6.5}$$

Similarly, the heat flux Q at a plasma-exposed surface is proportional to the ion density and temperature as $n_i T_i^{3/2}$, so that it can be written in the following form:

$$Q = \text{const} \times e^{-\frac{x(3\lambda_n+2\lambda_T)}{2\lambda_T\lambda_n}}, \tag{6.6}$$

from which the heat flux decay length is

$$\lambda_Q = \frac{2\lambda_T\lambda_n}{2\lambda_T+3\lambda_n}. \tag{6.7}$$

Average plasma parameters at the mirror surface in all mirror experiments are summarized in Table 6.1, where also the decay lengths and the accumulated particle fluences are indicated. Plasma parameters correspond to those at the center of mirrors, except for the case of the large SC Mo mirror exposure where the lower and upper values for n_e, T_e and Φ correspond to positions at the center of the mirror and at the plasma-closest edge, respectively. For the case of the Periscope system, the data for the last experiments with He and D_2 injections are indicated.

Due to small size of the test limiter compared to the plasma radius, it is often assumed that plasma parameters at a given radial position are the same along the limiter poloidally. This

assumption implies that the samples that are installed on the limiter as shown in Figure 5.5 face the same plasma, i.e. particles with the same energy and flux arriving at the surface along the line corresponding to a given radial coordinate. This also means that the balance of erosion and deposition on the sample holder should be the same for those locations leading to a transition from erosion to deposition zone in form of a horizontal line (poloidally) on the limiter surface. However, observing the inclined deposition pattern on the mirror holder, the poloidal inhomogeneity is visible (Figure 5.5a), and it may be concluded that the upper part of the Mo-coated mirror must have been exposed under conditions similar to those at the center of the Rh-coated mirror, which can be attributed to a variation of plasma parameters within a radial distance of 1 - 2 mm. The variation of plasma parameters can be, in turn, attributed to the finite poloidal radius of the plasma in TEXTOR.

Table 6.1. Average plasma parameters, decay lengths and accumulated particle fluences in mirror experiments.

	Low-fluence	High-fluence	Large SC Mo	Periscope
n_e (m^{-3})	2.6×10^{18}	3.6×10^{18}	$1.4 / 2.4 \times 10^{18}$	1.5×10^{18}
T_e (eV)	36	31	14 / 20	25
λ_n (mm)	24.1	26.6	26.6	39
λ_T (mm)	28.4	30.2	30.2	26.6
λ_Γ (mm)	17.0	18.5	18.5	22.5
λ_Q (mm)	10.6	11.5	11.5	12.2
No. of discharges	24	36	37	He: 22, D: 43
Fluence, Φ (m^{-2})	4.3×10^{24}	10.1×10^{24}	$2.8 / 5.9 \times 10^{24}$	He: 5.2×10^{24}, D: 9.1×10^{24}

6.1.2 Effect of gas feeding on plasma parameters

The experiments with different gases blown in the Periscope system, described in section 5.2, allow marking out the physical processes playing the major role in the mirror protection from deposition. The two gases used for this purpose are helium and deuterium, which have different physical and chemical properties. Helium is a non-reactive gas with the ionization energy of 24.6 eV such that the energy transfer with plasma ions (D^+) happens mostly in elastic collisions. Deuterium is a molecular gas with the dissociation energy of D_2 molecules of 4.56 eV. Ionization of D_2 molecules happens at 15.1 eV, and D atoms are ionized at 13.6 eV. In this case the energy transfer with D^+ plasma ions has a resonant character and is dominated by the charge-exchange process. Considering physical sputtering of deposited layers, the threshold energy for sputtering of carbon by impinging He ions is 19.12 eV. In the case of the D_2 gas injection, the rather low dissociation energy of D_2 molecules favours their prompt dissociation. To induce physical sputtering, D atoms have to be ionized and gain energy above 27.7 eV. Due to a lower mass physical sputtering in the case of deuterium is weaker than that for helium. In particular, at an ion energy of 50 eV the sputtering yield of carbon by He is about 4.8×10^{-3}, while it is 1.9×10^{-3} for the case of D impact [Eckstein 2011]. However, in addition to physical sputtering deuterium atoms and ions induce chemical erosion of deposited a-C:D layers. Considering the experimental results (section 5.2.3), namely the fact that the layer pre-deposited on the 1st mirror was not reduced in the case of the He gas injection, allows the conclusion that physical sputtering does not play a substantial role in the mirror protection from deposition under conditions of these particular experiments in TEXTOR. On the contrary, the experiments with the D_2 gas injection

emphasised the major role of chemical erosion in protecting and cleaning the mirror surface from a-C:D layers.

To assess the capability of injected deuterium to clean the mirror by chemical erosion, the following analysis was done. The chemical erosion yield at 380°C is 4×10^{-3} C/D (Figure 3.7). The atomic density of carbon atoms in a-C:D layers formed in TEXTOR is approximately 6.3×10^{22} C/cm^3 [Wienhold 1989]. Taking these values into account, the minimum amount of D atoms and ions needed to remove a 100 nm thick a-C:D layer from the deposited area of 6.8 cm^2 can be estimated as 1.1×10^{21}. The amount of D_2 molecules injected through the Periscope system during the mirror exposure was about 3.1×10^{20} per discharge, which potentially could result in 26.7×10^{21} D atoms if all molecules would be dissociated in all discharges. Such an amount of deuterium would be more than sufficient to clean the mirror. However, it is clear that only the closest to the mirror and already dissociated part of deuterium could contribute to the removal of the carbon layer. Therefore it is rather difficult to deduce the exact minimum of gas injection rate required for an effective mirror protection from deposition. In addition, as a result of elastic and non-elastic collisions of plasma ions with cold neutrals, carbon and deuterium ions from plasma lose their energy and can be even neutralized and scattered, thus reducing the effective contribution of plasma to the layer formation and removal. For a rough estimation of the mean free path of D^+ ions, the gas density inside the Periscope was calculated using the Bernoulli's equation in the form of a compressible flow equation. The resulting densities are shown in Table 6.2.

In the case of the He injection, the mean free path of D^+ ions can be estimated from the known reaction rate coefficient for elastic scattering of D^+ on He, which can be described as

$$K = 3 \times 10^{-9} T^{-1/3} \ cm^3/s \,, \tag{6.8}$$

where T is the ion temperature in eV [Vasil'ev 1982]. The resulting mean free path of a 50 eV D^+ equals then to 23.5 cm (Table 6.2).

In the case of injection of D_2 molecules, assuming that all of them are promptly dissociated into individual deuterium atoms, charge exchange represents the most probable reaction channel with SOL plasma ions. The corresponding reaction rate coefficient for the conditions of the experiment is about 3×10^{-8} cm^3/s [Freeman 1974], resulting in the mean free path for D^+ ions of about 3.4 cm (Table 6.2).

Comparing the mean free path of D^+ in D and He neutral gas clouds, which is about 7 times larger in the case of He for a factor of about 5 smaller density (4.8×10^{13} D/cm^3 against 1.0×10^{13} He/cm^3, Table 6.2), it can be concluded that D and He would have protected the mirror surface from impurity ions from plasma with a comparable effectiveness if chemical erosion would not have played a role. This could be the case, for example, for prevention of beryllium or tungsten deposition on the mirror surface.

In order to estimate the contribution of chemical erosion by deuterium atoms or ions resulting from dissociation of injected D_2 molecules, processes leading to dissociation or ionization of D_2 molecules have to be considered. These processes are the dissociation under electron and ion impact and the charge exchange. The Maxwell averaged reaction rates, R, from the ground vibrational state and corresponding mean free paths, λ_{mfp}, for these processes are summarized in Table 6.2 (see also Figure 6.2).

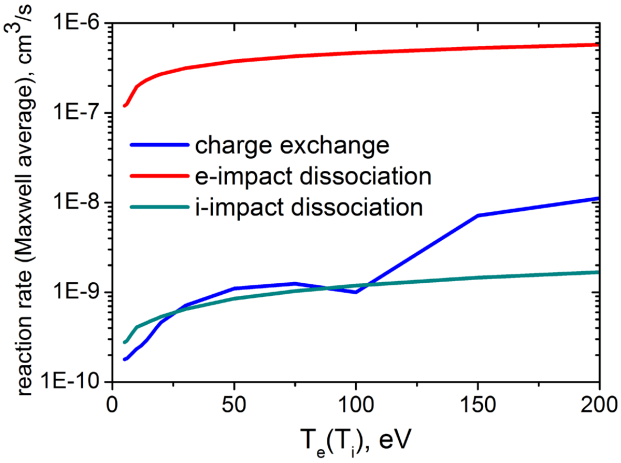

Figure 6.2. Reaction rate for processes of charge exchange and dissociation of D_2 molecules caused by interaction with electrons and ions depending as functions of electron and ion temperature, respectively [Guzmán 2013].

Table 6.2. Summary of interaction processes between plasma ions and injected gases in the Periscope system with calculated mean free paths λ_{mfp} of D^+ ions in the gas cloud.

Injected gas	Particle density, cm^{-3}	Reaction	Reaction rate coefficient, K (cm^3s^{-1})	λ_{mfp} (cm)
He	1.0×10^{13}	Elastic scattering of 50 eV D^+ on He	8×10^{-10}	23.5
D (from full dissociation of D_2)	4.8×10^{13}	Charge exchange of 50 eV D^+ on D	3×10^{-8}	3.4
Injected gas	Particle density, cm^{-3}	Reaction	Maxwell averaged reaction rate, R (cm^2)	λ_{mfp} (cm)
D_2	4.5×10^{13}	Charge exchange	1.1×10^{-9}	78.7
		Electron impact dissociation	2.9×10^{-7}	0.3
		Ion impact dissociation	8.5×10^{-10}	10^4

Comparing the reaction rates and mean free paths for all three reactions, one can see that the dissociation of D_2 molecule under electron impact is the most probable and must have happened inside the Periscope system in the vicinity of the first mirror.

The above estimations support the conclusion that the complete cleaning and protection of the mirror surface during the D_2 gas injection was possible because of chemical erosion of carbon by low energy D atoms. These atoms resulted from the dissociation of injected D_2 molecules and were present in a sufficient amount near the mirror surface due to relatively short mean free path of molecules. More detailed analyses can be performed with help of dedicated modeling.

6.1.2.1 *Modelling of influence of D_2 gas injection on plasma parameters near and inside the Periscope*

The modelling was done to study physical processes during the D_2 gas injection through the Periscope mirror system and to assess their influence on the plasma parameters and erosion-deposition conditions near the 1st mirror. A one-dimensional model of the SOL initially developed to study the transition to supersonic flow conditions in high recycling and weakly detached plasmas was applied [Marchuk 2007]. This transition corresponds to high neutral densities, and therefore the code suits well to the described gas injection experiments in TEXTOR. In the model, a system of coupled equations for the conservation of plasma particles (including recycling particles), momentum and heat transfer is solved along magnetic field lines as shown in Figure 6.3. The equations for the ion and electron temperatures are solved independently taking into account the low collisionality conditions usually observed at TEXTOR [Huber 2000].

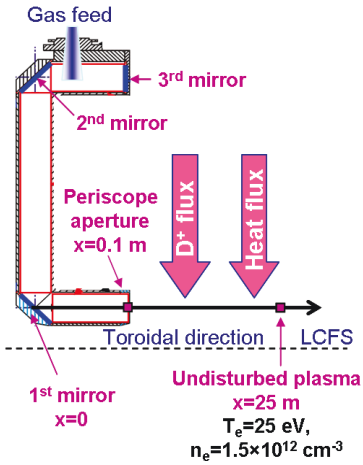

Figure 6.3. Scheme of the Periscope mirror system indicating the geometry and assumptions of the 1D model applied: the black arrow corresponds to the simulated magnetic field line.

The injection of the D_2 gas was modelled by introducing a source of D atoms at the location of the 1st mirror with a source function *S(x)* according to [Stangeby 2000]:

$$S(x) = \frac{1}{\sqrt{2\pi}\Delta} \exp\left(-\frac{x^2}{\Delta^2}\right), \tag{6.9}$$

where Δ is the e-folding length of the source intensity with distance x counted from the surface of the 1st mirror. The choice of the Gaussian profile for the source function takes into account the following effects. At one hand, this function approaches the δ-function in the limit of a small parameter Δ and therefore represents a strong source in the vicinity of the 1st mirror, thus reflecting the experimental conditions. At the other hand, the integral over the source function provides the particle influx into the Periscope, i.e. the total number of injected neutral particles. Further dynamics of neutrals is described in the model in the diffusion

approximation. It is also assumed that neutrals may escape to the main plasma volume only when they leave the Periscope through the aperture located at x = 0.1 m. In this case neutral particles leave the SOL with the frequency $\nu = \Delta_{SOL} / v_n$, where Δ_{SOL} is the radial SOL width and v_n is the speed of neutral particles. More details about the model can be found in [Marchuk 2007].

Figure 6.4 and Figure 6.5 show the profiles of plasma parameters along magnetic field lines obtained with the model for the cases with and without gas injection. Profiles of the neutral density (Figure 6.4 b) demonstrate a significant increase at the position of the 1st mirror in the case with the D_2 gas injection included and a simultaneous steepening of the plasma density profile near the mirror. This behavior indicates the transition from the sheath limited regime, i.e. plasma is essentially isothermal along the magnetic field line, to the high recycling regime, characterized by a significant parallel temperature drop between locations far away from the surface and the sheath edge in front of the surface [Stangeby]. Correspondingly, a drop of the ion and electron temperatures along the SOL is obtained (Figure 6.5). The ion temperature in the modelling is approximately twice the electron temperature, which reproduces well typical conditions in TEXTOR for the edge plasma parameters observed in the experiments [Huber 2000].

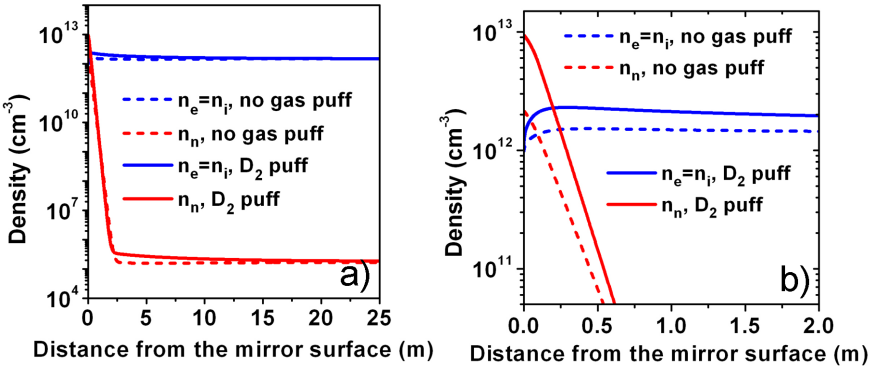

Figure 6.4. Plasma and neutral gas densities inside and outside the Periscope mirror system obtained from the modelling for the cases without gas injection and with the D_2 gas feeding: a) profiles along the magnetic field line (x = 25 m corresponds to unperturbed plasma); b) profiles in the region near the Periscope mirror system.

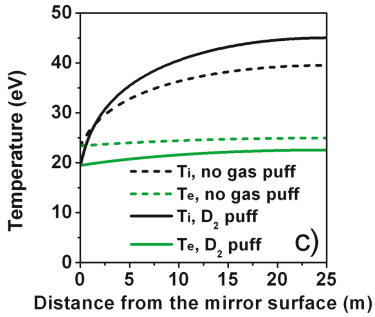

Figure 6.5. Electron and ion temperatures inside and outside the Periscope mirror system obtained from the modelling for the cases without gas injection and with the D_2 gas feeding.

Figure 6.6 a shows a weak dependence of plasma parameters near the mirror surface on the e-folding length of the deuterium source. Some variation of plasma parameters is observed only for Δ above 5 – 10 cm. For such values of Δ injected particles leave the Periscope without interaction with plasma ions and electrons, resulting in an increase of the ion temperature. The electron temperature does not change. Figure 6.6 b demonstrates the variation of plasma parameters at the position of the 1st mirror as a function of the gas injection rate. The transition to the high recycling regime occurs at a puffing rate of about 10^{20} – 10^{21} at/s when the electron temperature drops down and the plasma density at the mirror starts to increase. Such a behaviour indeed leads to a reduction of plasma and impurity fluxes to the mirror surface and, consequently, to a reduction of carbon deposition on the 1st mirror, thus confirming the experimental observations.

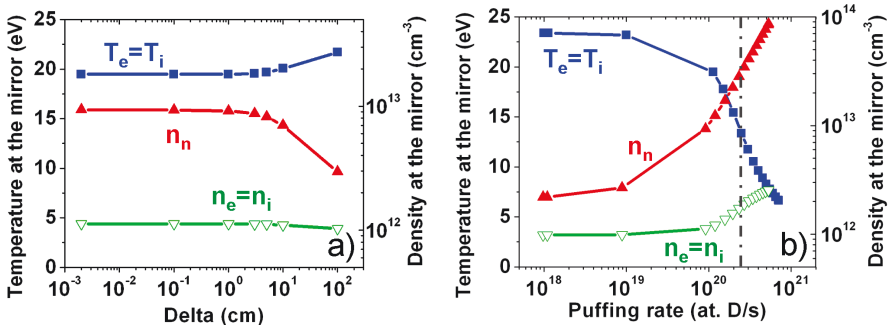

Figure 6.6. The electron (T_e) and ion (T_i) temperatures, and plasma (n_e=n_i) and neutral (n_e) densities at the center of the 1st mirror: a) depending on the e-folding length of the gas source; b) depending on the gas injection rate. The gas injection rate during the exposure with the D_2 gas feeding was equal to 1.13×10^{20} at/s, which is shown as a dash-dotted line on the figure.

6.2 Erosion of the surface

6.2.1 Distortion layer

Metallic surfaces are known to modify their structure after polishing. As a result, the top layer of the surface affected by polishing acquires a disordered structure. This layer is thus called the *distortion* or *smeared layer*. In [Manhard 2013] it is shown that a distortion layer forms after mechanical fine grinding and also after polishing with the diamond suspension. Such treatments form microstructures on the surface, which are not equivalent with the bulk structure of the sample. Namely, the characteristic size of surface grains in the distortion layer is typically much smaller than the characteristic size of bulk grains. In the case of a SC material, the distortion layer also has a disordered structure and therefore does not possess the same properties as the bulk. In practice this means that the true erosion properties of a SC mirror can be studied only after the distortion layer is completely removed.
Depending on the material, the thickness of the distortion layer can vary very significantly. In case of tungsten, a thickness of 500 nm was reported in [Manhard 2013]. In case of polished diamond, however, only few nm of the surface were affected [Pastewka 2011]. Generally speaking, the thickness of the distortion layer cannot be predicted and must be defined from measurements. After a SEM investigation of a perpendicular cut of a SC Mo mirror sample, it was concluded that there was no distortion layer on SC Mo mirrors used for experiments presented in this thesis,. The coated mirrors should not have had a distortion layer since polishing was performed only on the substrate, i.e. before the coating procedure. Such mirrors were not mechanically treated after the coating procedure.

6.2.2 Amount of material removed during exposures under erosion conditions

As a result of exposures under erosion conditions, the studied mirror samples were sputtered at different rates. In general, the thickness of the layer sputtered from a mirror surface depends on the elemental composition of the surface, which means the mirror material. It is also a function of exposure conditions such as types and fluxes of different bombarding species, particle impact energies, angles, and exposure times. To verify the involved physical processes, the experimentally obtained sputtered thicknesses can be compared with a simple analytical calculation. Such a comparison was done for Rh- and Mo-coated mirrors used for the low-fluence exposure, based on the empirical dependence of the erosion yield of a particular mirror material on energies and atomic masses of impinging particles [Eckstein 1993, Yamamura 1996].
The sputtering yield represents a rather sensitive function of plasma parameters in front of the mirror surface. For the range of conditions in TEXTOR experiments, a 15 % variation of the electron temperature near the mirror surface can lead to a change in the sputtering yield (and correspondingly in the calculated sputtered thicknesses d_{Rh} and d_{Mo}) within a factor of 2.7. However, in calculations, the ratio $\chi = d_{Rh} / d_{Mo}$ appears to be less sensitive to such variations. Therefore, the experimentally measured ratio $\chi_{exp} = 2.5$ and not the sputtered thicknesses themselves were compared with the analytical solution. The calculated ratio χ_{calc} stays in the range of $1.67 - 1.76$, accounting for uncertainties in the measured plasma parameters. The discrepancy between the calculated and experimentally measured values of χ can be explained in the following way. As it was mentioned in section 6.1.1, the upper part rather than the center of the Mo-coated mirror must have been exposed under conditions

similar to those at the center of the Rh-coated mirror. Therefore, erosion at the upper part of the Mo-coated mirror (67 nm compared to 40 nm in the center, section 5.1.3.1) has to be compared with erosion in the center of the Rh-coated mirror (100 nm). With such a correction, the experimentally determined value of χ_{exp} becomes equal to 1.68, which agrees with the calculated values very well.
In the case of the high-fluence exposure, the Mo-coated mirror in its centre was sputtered by about 122 nm, while the sputtered thickness of the Rh-coated mirror reached 340 nm. These measurements correspond to the ratio $\chi_{exp} = 2.78$, while the calculated value χ_{calc} stays below 1.71, being generally lower than in the low-fluence exposure due to the lower plasma temperature. Applying the same correction as for the low-fluence exposure, namely considering the ratio of sputtered thicknesses at the centre of the Rh-coated mirror and at the upper part of the Mo-coated mirror, results in $\chi_{exp} = 2.19$. The remaining discrepancy between the measured and calculated values of χ can be attributed to the fact that the estimates of χ_{calc} described above were done for monoenergetic projectiles, while during the exposure the Maxwellian energy distribution is characteristic for the ions. Although such calculations are good enough for rough estimations of sputtering rates of pure materials, they do not account for simultaneous implantation and deposition of impurities, neither any other physical and chemical processes involved. The measured and calculated values of χ are summarized in Table 6.3, where also the values of χ obtained from computer simulations are shown (see the following sub-sections).

Table 6.3. Ratios of sputtered thicknesses of Rh and Mo mirrors obtained in the low-fluence and high-fluence experiments (χ_{exp}) and obtained from estimative calculations using the Eckstein-Yamamura fit of sputtering yields (χ_{calc}) and simulations with the SDTrimSP code (χ_{sim}).

Low-fluence	χ_{exp}	$\frac{d_{Rh\ center} = 100\ nm}{d_{Mo\ center} = 40\ nm} = 2.5$	$\frac{d_{Rh\ center} = 100\ nm}{d_{Mo\ top} = 67\ nm} = 1.68$
	χ_{calc}	1.67 – 1.76	
	χ_{sim}	1.23 – 3.27	
High-fluence	χ_{exp}	$\frac{d_{Rh\ center} = 340\ nm}{d_{Mo\ center} = 122\ nm} = 2.78$	$\frac{d_{Rh\ center} = 340\ nm}{d_{Mo\ top} = 155\ nm} = 2.19$
	χ_{calc}	≤ 1.71	
	χ_{sim}	1.34 – 4.50	

6.2.2.1 Simulation of the mirror erosion with the SDTrimSP code

To evaluate sputtering rates of mirror materials under realistic simultaneous implantation of impurities more precisely, the Monte-Carlo computer code SDTrimSP (version 5.00) [Eckstein 2007] was used. The code describes the impact of energetic projectiles on amorphous solids using the approximation of binary collisions between the projectile and atoms of the target. In this work the dynamic version of the code was used, which accounts for modifications of the target composition during the ion bombardment. An attempt to account for re-deposition of the eroded mirror material on the mirror surface was made. Chemical erosion was not included in the simulations.

The simulations were set up to reproduce the experimental conditions:

- Maxwellian ion energy distribution corresponding to T_i = 70 eV (low fluence-exposure) and T_i = 60 eV (high-fluence) exposure assuming sheath acceleration of $3kT_e$.
- Angle of incidence 40° corresponding to the most probable one for plasma ions for the case of a 20° inclination of the magnetic field lines to the mirror surface (according to the angular distributions obtained with the ERO code [Borodin 2013] (Figure 6.7).

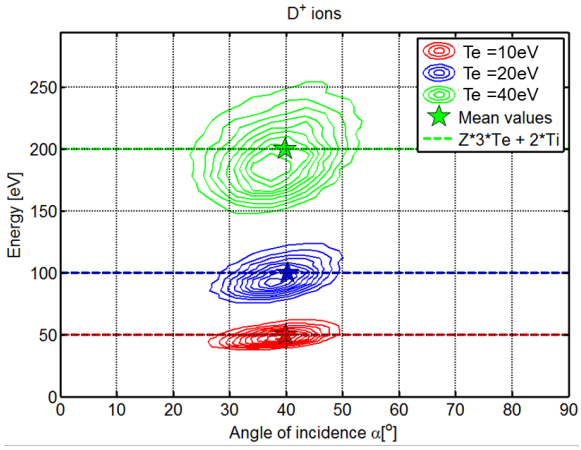

Figure 6.7. Angular distributions of projectiles – D^+ ions incident on the TEXTOR roof-limiter for T_e = 10, 20 and 40 eV [Borodin 2013]. Distributions with similar most probable angles of incidence are observed for impurity ions in higher charge states.

It was estimated (see section 6.3.3) that under conditions of the mirror exposure in TEXTOR accumulation of hydrogen and deuterium in the Rh and Mo samples should not have happened. Therefore, these processes were not included in the simulations.
The surface binding energy E_{sb} is an important parameter in SDTrimSP simulations, which influences the probability of a displaced atom or a backscattered projectile to leave the surface. For self-sputtering of monoatomic targets, E_{sb} is taken as the cohesive energy of the material. As no clear values for mixed bombardments exist, E_{sb} is usually defined as the cohesive energy of the substrate material in this case. For a single crystal material it can vary strongly depending on the crystal orientation. In addition, different chemical compounds could be formed on the mirror surface during the exposure (rhodium and molybdenum oxides, molybdenum carbides, and also compounds with the CO-group). Surface binding energies in case of complex multi-component targets could vary depending on the type of bonding [Frese 1987], as well as on the relative orientation of bound atoms. In this case the simple model that is usually used to estimate the surface binding energies for particular atomic pairs is such that the surface binding energy of one type of species to another is approximated by the average self-binding energy of each species, e.g.

$$E_{sb}(\text{O on Mo}) = (E_{sb}(\text{Mo}) + E_{sb}(\text{O})) / 2. \quad (6.10)$$

As a more sophisticated approach, the average binding energy can be calculated taking into account the stoichiometry, e.g.

$$E_{sb}(\text{O on Mo}) = ¼\, E_{sb}(\text{Mo}) + ¾\, E_{sb}(\text{O}) \quad (6.11)$$

in the case of surface composition corresponding to MoO_3.
In order to check the sensitivity of SDTrimSP results to changes of the surface binding energy, several simulations were performed, in which the surface binding energies *E_{sb}(O on Mo)* and *E_{sb}(O on Rh)* were varied according to the available literature data and the models presented above, as summarized in Table 6.4. For most cases of heterogeneous sputtering (C on Mo, C on Rh, etc.), the simple averaging of the binding energies was used.
As an example, according to simulation assuming different Mo crystal orientations, the amount of the sputtered material (the sputtered depth) of the Mo mirror in conditions of the low-fluence exposure could vary between 166 nm and 352 nm. It equals 352 nm if E_{sb}(O on Mo) = 4.7 eV (simple averaging) is used. When E_{sb} (O on Mo) = 6.53 eV (Mo_2O, [Petrova 2009]) is used instead, the sputtered depth of about 324 nm is obtained. Similarly, simulated erosion of the Rh-coated mirror varies for different types of bonding of oxygen in polycrystalline Rh. The results are summarized in Table 6.5 for Mo and in Table 6.6 for Rh.

Table 6.4. Surface binding energies of species used in SDTrimSP simulations.

E_{sb}(eV)	C	O	Mo	Rh
C	7.4 [1]	=	=	=
O	4.99 [1,*]	2.58 [1]	=	=
Mo	7.105 [1,*] 7.390 [2,*] 8.290 [3,*] 8.090 [4,*]	4.70 [1,*] 4.98 [2,*] 5.88 [3,*] 5.68 [4,*] 3.64 [1,§] 4.73 – 5.12 [5] 6.10 – 6.85 [6] 6.53 [7]	6.81 [1] 7.38 [2] 9.18 [3] 8.78 [4]	×
Rh	6.59 [1,*]	4.18 [1,*] 3.95 – 4.81 [8]	×	5.78 [1]

[1] SDTrimSP data pool;
[2] SC Mo(111); [3] SC Mo(110); [4] SC Mo(100) [Eckstein 1991];
[5] SC Mo(100) [Frese 1987]; [6] SC Mo(110) [Petrova 2009]; [7] Mo_2O [Petrova 2009]
[8] Poly Rh [Frese 1987];
[*] simple averaging; [§] stoichiometric averaging (MoO_3);
= equal to the transposed (e.g. Mo-on-O = O-on-Mo).

6.2.2.2 Re-deposition accounting for SDTrimSP simulations

In attempt to simulate possible effects of re-deposition of sputtered particles, simulations with a modified mix of projectiles (including Mo and Rh as bombarding species) were done. To calculate the fraction of Mo in the initial flux in the case of the Mo-coated mirror in the low-fluence exposure, the number of sputtered Mo atoms was estimated based on the sputtering yield of Mo (Y = 0.53%, see Table 6.5). The Mo fraction is then re-calculated according to other incoming species. The resulting mix of species coming to the surface was then the following:

H	D	C	O	Mo
47.84%	47.84%	2.87%	0.95%	0.50%

Similarly, in the case of the Rh-coated mirror in the low-fluence exposure, for which the sputtering yield is higher (Y = 0.77%, see Table 6.6), the incident mixture was as follows:

H	D	C	O	Rh
47.705%	47.705%	2.862%	0.954%	0.774%

It was assumed that sputtered Mo and Rh atoms were ionized in the vicinity of the surface and returned to the surface as singly charged ions with an initial energy of 1 eV, being then accelerated to an energy of $3kT_e$ in the sheath. Such an approach describes the re-deposition only roughly and over-estimates it since all sputtered particles are assumed to return to the surface. As a result, a significant decrease in the sputtered thickness was observed in the simulations, accounting for re-deposition, while keeping all other parameters the same. In the case of Mo, the decrease was from 352 nm down to 318 nm (by 9.7%) for the low fluence

exposure, and from 649 nm down to 563 nm (by 13%) for the high-fluence exposure. For Rh mirrors in the low-fluence and high-fluence exposures (Table 6.6), accounting for re-deposition results in the sputtered depth changes of 9.1% and 11.9%, respectively, similar to the case of Mo mirrors.

According to the results summarized in Table 6.5, the sputtered depth of Mo mirrors in the low-fluence and high-fluence exposures changes by 13.4% and 12.3% due to variation of the surface binding energy of oxygen alone. However, the differences due to different binding energies of oxygen in the case of Rh equal just to 3% (low-fluence exposure) and 4.1% (high-fluence exposure).

With the parameter variations discussed above, the simulated value χ_{sim} is in the range of 1.23 – 3.27 in the case of the low-fluence exposure and in the range of 1.34 - 4.50 in the case of the high-fluence exposure (Table 6.3). The results of the modelling show that predictive simulations in the case of sputtering of mixed materials are very sensitive to the input data. For an accurate description, the crystal orientation, the actual state of surface atoms and corresponding binding energies of all the components have to be known. Still the experimentally measured ratio $\chi_{exp,}$ as well as the calculated range χ_{calc}, falls into the range of simulated χ_{sim} very well. What is more important, the simulated sputtered depths of both Mo and Rh mirrors are in a good agreement with experiment, namely within a factor of 1.5-2, despite their strong sensitivity to plasma parameters.

Table 6.5. Results of SDTrimSP simulations for Mo mirrors.

	№	Case	Surface Binding Energy,eV			Re-dep	**Eroded depth, nm**	Surface concentration, %			Sputtering yield Y, %			Reflection yield R, %			
			Mo on Mo	C on Mo	O on Mo			C	O	Mo	C	O	Mo	H	D	C	O
Low-fluence, T_i=70 eV, Sheath 105 eV	**L1**	1,*	6.81	7.105	4.70		**351.62**	20.26	4.73	75.00	1.06	0.32	0.53	28.81	19.71	0.43	0.11
	L3	3,*	Mo(110) 9.18	8.29	5.88		**166.21**	24.17	5.97	69.86	1.08	0.32	0.30	27.91	18.85	0.40	0.10
	L4	4,*	Mo(100)8.78	8.09	5.68		**189.22**	23.25	5.77	70.98	1.08	0.33	0.32	28.02	18.99	0.40	0.10
	L2	2,*	Mo(111)7.38	7.39	4.98		**295.63**	21.54	4.95	73.50	1.05	0.32	0.46	28.65	19.54	0.41	0.11
	L7	1,7	6.81	7.105	Mo_2O 6.53		**324.07**	20.98	6.37	72.65	1.07	0.32	0.49	28.55	19.50	0.41	0.11
	L1r	1,*	6.81	7.105	4.70	+	**317.69**	20.57	4.70	74.73	1.05	0.31	0.53	28.82	19.70	0.43	0.11
	L3r	3,*	Mo(110) 9.18	8.29	5.88	+	**128.64**	24.16	6.04	69.80	1.07	0.32	0.30	27.90	18.87	0.39	0.10
	L4r	4,*	Mo(100)8.78	8.09	5.68	+	**152.11**	23.74	5.53	70.73	1.08	0.32	0.32	27.99	18.98	0.39	0.11
	L2r	2,*	Mo(111)7.38	7.39	4.98	+	**258.85**	21.08	4.95	73.97	1.05	0.31	0.46	28.60	19.44	0.43	0.11
	L§r	1,§	6.81	7.105	MoO_3 3.64	+	**333.37**	19.76	3.83	76.41	1.04	0.31	0.55	29.01	19.83	0.43	0.12
	L7r	1,7	6.81	7.105	Mo_2O 6.53	+	**288.81**	20.91	6.30	72.79	1.06	0.32	0.49	28.54	19.37	0.42	0.11
High fluence, T_i=60 eV, Sheath 90 eV	**H1**	1,*	6.81	7.105	4.70		**648.5**	21.49	4.96	73.55	1.06	0.32	0.43	28.95	19.67	0.43	0.11
	H3	3,*	Mo(110) 9.18	8.29	5.88		**261.69**	27.14	6.41	66.45	1.09	0.33	0.23	27.71	18.55	0.38	0.10
	H4	4,*	Mo(100)8.78	8.09	5.68		**311.57**	25.75	6.44	67.81	1.08	0.32	0.25	27.98	18.76	0.38	0.11
	H2	2,*	Mo(111)7.38	7.39	4.98		**528.85**	22.52	5.46	72.02	1.06	0.32	0.36	28.71	19.41	0.41	0.11
	H1r	1,*	6.81	7.105	4.70	+	**563.11**	21.20	4.96	73.84	1.06	0.31	0.43	28.89	19.62	0.42	0.11
	H3r	3,*	Mo(110) 9.18	8.29	5.88	+	**174.67**	26.54	6.31	67.15	1.08	0.32	0.23	27.69	18.53	0.36	0.10
	H4r	4,*	Mo(100)8.78	8.09	5.68	+	**220.39**	25.41	6.17	68.41	1.07	0.32	0.25	27.90	18.72	0.39	0.10
	H2r	2,*	Mo(111)7.38	7.39	4.98	+	**445.64**	22.56	5.38	72.07	1.06	0.32	0.37	28.62	19.37	0.42	0.11
	H5r	1,5	6.81	7.105	MoO4.73	+	**561.21**	21.92	5.21	72.87	1.06	0.31	0.43	28.90	19.61	0.42	0.12
	H7r	1,7	6.81	7.105	Mo_2O 6.53	+	**493.62**	22.63	7.01	70.36	1.08	0.32	0.39	28.52	19.23	0.41	0.11

Table 6.6. Results of SDTrimSP simulations for Rh mirrors.

	№	Case	Surface Binding Energy,eV			Re-dep	**Eroded depth, nm**	Surface concentration, %			Sputtering yield Y, %			Reflection yield R, %			
			Rh on Rh	C on Rh	O on Rh			C	O	Rh	C	O	Rh	H	D	C	O
Low-fluence, T_i=70 eV, Sheath 105 eV	**L1-Rh**	1,*	5.78	6.59	4.18		**463.3**	16.52	3.78	79.7	1.01	0.30	0.77	30.08	20.74	0.47	0.13
	L1r-Rh	1,*	5.78	6.59	4.18	+	**421.28**	16.11	3.83	80.06	1.00	0.30	0.77	29.96	20.73	0.47	0.13
	L8r-Rh	1,8	5.78	6.59	3.95	+	**420.23**	16.55	3.74	79.71	1.01	0.30	0.76	29.98	20.72	0.47	0.13
	L9r-Rh	1,8	5.78	6.59	4.813	+	**408.84**	16.43	4.35	79.22	1.01	0.30	0.75	29.88	20.63	0.47	0.12
High fluence, T_i=60 eV, Sheath 90 eV	**H1-Rh**	1,*	5.78	6.59	4.18		**880.89**	16.96	3.80	79.24	1.01	0.30	0.64	30.23	20.80	0.49	0.13
	H1r-Rh	1,*	5.78	6.59	4.18	+	**776.35**	17.09	3.96	78.95	1.02	0.29	0.64	30.25	20.76	0.47	0.13
	H8r-Rh	1,8	5.78	6.59	3.95	+	**786.01**	17.36	3.94	78.71	1.00	0.30	0.64	30.30	20.84	0.48	0.13
	H9r-Rh	1,8	5.78	6.59	4.813	+	**753.88**	17.54	4.28	78.18	1.01	0.30	0.62	30.14	20.70	0.47	0.13

6.2.3 Surface roughening: erosion of single crystal and polycrystalline materials

Roughening of the mirror surface leads to increased diffuse scattering of the incident light. As a result, the specular component of the reflected light, which is typically detected and used in diagnostics, is reduced. In this work the roughness of the investigated mirrors was measured before and after exposure in TEXTOR by means of surface profiling (section 4.4). In addition, an attempt to estimate the surface roughness after exposure from the specular reflectivity measurements was made. Using the Bennett formula (equation (2.14) from section 2.3.2), the resulting roughness of the mirror surface can be estimated from its initial roughness and the experimentally measured change of R_{spec}. The formula is only valid for reflectivity measurements made at sufficiently long wavelengths. In practice this means that to get a result within an error bar of 10% with the Bennett formula, the ratio of the wavelength λ of the incident light to the root mean square surface (RMS) roughness σ must be over 40 [Bennett 1961].

The surface roughness of the Rh-coated mirror measured by profilometry changed from about 21 nm before the exposure to about 29 nm after the high-fluence exposure. The measured drop of the intensity of the specular reflected light, attributed to the growth of the diffuse reflectivity of the mirror (Figure 5.18a), was ~25 % in the UV wavelength range (Figure 5.18b, Figure 5.24a,b). The corresponding value of the RMS roughness can be then calculated according to the Bennett formula as 26 – 42 nm, depending on the wavelength of the probing light in the range of 250 – 2500 nm (Figure 6.8 (a)). Results of a similar calculation performed for the Mo-coated mirror are shown in Figure 6.8 (b). Although the wavelength criterion $\lambda/\sigma \geq 40$ for the Bennett formula is fulfilled for wavelengths above ~ 1200 nm in the case of the Rh-coated mirror and already for ~ 400 nm in the case of the Mo-coated mirror, a significant variation of σ with the wavelength of the probing light is observed in both cases. Such a non-physical behaviour disclaims the applicability of the Bennett formula in the case of the described experiment. The most probable reason for that is the presence of impurities on the mirror surface. Impurities modify the electronic structure of the material and thus affect the specular reflectivity of metallic mirrors, while the Bennett formula supposes that the difference in the reflectivity is only due to the change in the surface roughness.

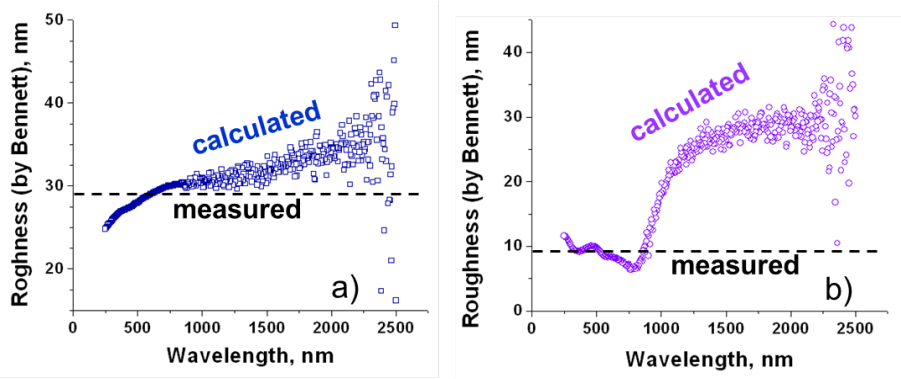

Figure 6.8. The surface roughness of a) the Rh-coated mirror and b) the Mo-coated mirror after the high-fluence exposure estimated from the specular reflectivity measurements. The dashed lines correspond to the surface roughness measured by profilometry.

According to SIMS measurements (see discussion in section 6.3.2.2.), all exposed mirrors exhibit the presence of carbon on the surface. In addition, a small fraction of Mo, mostly in the metallic form, was detected on the Rh surface by XPS measurements. Carbon originates from erosion of wall components of TEXTOR, mainly of the toroidal limiter ALT-II, and contributes to the background plasma flux. Molybdenum comes from local erosion of the sample holder (99 at% Mo). These impurities obviously influence the optical characteristics of the mirror so that the Bennett formula for the specular reflectivity provides only a rough estimate of the possible range of values for the surface roughness.
However, the theory described in [Bennett 1961] allows equally easy calculation of the value of the surface roughness from measurement of the diffuse reflectivity of the sample. In the case when the ratio of the total reflectivity of the sample to the reflectivity of the same material with $\sigma = 0$ is close to unity, the following equation describes the relation between the diffuse reflectivity and the root mean square roughness:

$$R_{diff} = R_0 \cdot (4\pi\sigma)^2 / \lambda^2. \tag{6.12}$$

Using this formula it is possible to derive the dependence of the surface roughness after the exposure on the value of the surface roughness before the exposure and the diffuse reflectivity of the sample as measured before and after the exposure:

$$\sigma_{after} = \sigma_{before} \sqrt{R_{dif\_after} / R_{dif\_before}} \tag{6.13}$$

While the diffuse reflectivity is largely determined by the surface morphology and not that much by the actual chemical composition of the surface, such modified Bennett formula can be successfully applied to the mirrors in the discussed experiment, yielding results shown in Figure 6.9. It can be seen from the graphs that the same restriction on the wavelength of the probing light applies and the RMS roughness becomes quasi-constant for wavelengths above ~ 1500 nm for the Rh mirror and ~ 1000 nm for the Mo one. For these regions the calculated surface roughness is in a very good agreement with profilometry measurements for both mirrors within the scatter of the experimental data on the mirror reflectivity. This indicates the applicability of the Bennet formula for R_{dif} even in the case of presence of impurities on the mirror surface in the described experiment.

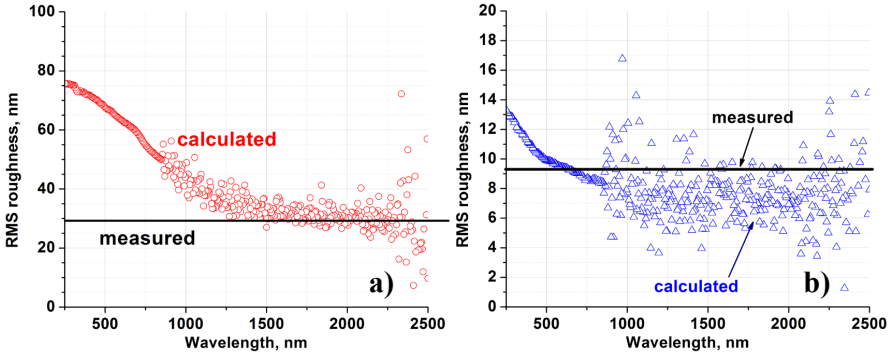

Figure 6.9. The surface roughness of a) the Rh-coated mirror and b) the Mo-coated mirror after the high-fluence exposure estimated from the diffuse reflectivity measurements. The solid lines correspond to the surface roughness measured by profilometry.

6.3 Deposition, implantation and diffusion

6.3.1 Carbon deposition and the effect of gas feeding on the deposit growth

Deposition of impurities on the mirror surface is determined by the correlation between many physical processes, among which the major ones are the following:

- implantation and reflection or sticking of incident impurity atoms;
- physical and chemical sputtering of the mirror material and already deposited impurity atoms;
- diffusion of implanted atoms to the surface and into the bulk;
- formation of chemical phases.

Due to the low temperature of the mirror (150°C), chemical erosion did not play a significant role during the first exposure of the Periscope mirror system (see the temperature dependence of chemical erosion in section 3.3). To increase the contribution of chemical erosion to the carbon removal in the second experiment, heating of the Periscope up to about 400°C was applied. However, in contrast to the experiment in DIII-D where the complete suppression of carbon deposition was achieved only by means of a moderate increase of the mirror temperature [Litnovsky 2008], no measurable suppression of carbon deposition on the 1st mirror was observed in this case. The most probable explanation for this result is that the flux of carbon ions was so high that chemical erosion was not prevailing even at elevated temperatures. A simple consideration can be the following. For the plasma electron temperature of about 25 eV, the average incident energies of ions at the mirror surface can be estimated to be about 100 eV for H^+ and D^+ and around 300 eV for C^{3+} due to acceleration in sheath. For such energies the reflection coefficient of C can be estimated as $R \sim 0.01$ if the surface is already covered with carbon and $R \sim 0.4$ in the case of the initial Mo surface [Eckstein 2002]. Correspondingly, the physical sputtering yields of C by D^+ ions $Y_{D\rightarrow C} \sim 0.01$; C by H^+ ions $Y_{H\rightarrow C} \sim 0.003$; as well as the carbon self-sputtering yield $Y_{C\rightarrow C} \sim 0.1$ can be obtained [Eckstein 2002]. Carbon impurity contributes typically 2 – 4% to the total plasma flux at the radial position of the Periscope [Tanabe 1994, Ding 2010]. An assumption of a carbon content in the plasma flux of 3% would mean that for each D^+ ion arriving to the mirror, there could be $N_1 = 8.5\times10^{-3}$ C atoms potentially deposited on the mirror surface if it is clean or $N_2 = 20\times10^{-3}$ C atoms if the surface is already covered with carbon (physical sputtering already accounted for as partial removal of depositing species). For the mirror temperature of about 400°C, chemical erosion of a-C:D layers by deuterium is about 4×10^{-3} (Figure 3.7), which is less than N_1 and N_2 and therefore would be not sufficient to remove all deposited carbon atoms. It has to be noted that due to angular and energy dependence of the reflection and sputtering yields, as well as due to uncertainty in the chemical erosion yield, it is not possible to make a precise estimate of the actual carbon deposition rate, neither to compare it with that observed in the experiment. However, these simplified calculations demonstrate the importance of the flux balance for the net erosion-deposition conditions on the mirror surface and potentially can explain the low effectiveness of the sole mirror heating under TEXTOR edge plasma conditions.

During subsequent exposures of the Periscope system, the plasma parameters in the vicinity of the first mirror were significantly altered by the D_2 gas injection (section 6.1.2); the balance of the physical processes involved and corresponding erosion-deposition balance were shifted. As it was concluded from the estimates presented in section 6.1.2, injection of D_2

molecules increased the contribution of chemical erosion by providing additional D atoms and ions as a result of the dissociation process. Larger influx of D atoms capable of chemical erosion lead, in turn, to complete protection of the mirror surface from impurity deposition and even supported cleaning of the pre-deposited a-C:D layer.

6.3.2 Implantation and diffusion of carbon and oxygen

In this section the contribution of the particle implantation and diffusion to the formation of deposited impurity layers and contamination of the mirror surface will be discussed. Contamination of the mirror surface with carbon and oxygen, main impurities in the TEXTOR plasma, was observed in erosion experiments, as well as during the exposures of the Periscope system under deposition-dominated conditions. The influence of the observed surface contamination, in particular the formation of chemical phases such as carbides and oxides, on the optical properties of mirrors will be discussed in section 6.4.

6.3.2.1 Diffusion in the case of the Periscope mirrors

In the case of the exposure of the Periscope system with the D_2 gas feeding, visual observations suggested that the pre-deposited layer was completely removed from the exposed part of the mirror surface, while kept intact under the protective bar (section 5.2.3.). Indeed, only a trace amount of residual carbon was detected (by SIMS) on the visually clean part of the mirror, and the overall thickness of the pre-deposited layer under the protective bar remained constant within the uncertainty of the method. However, indications of diffusion of carbon and oxygen at the interface between the substrate and the pre-deposited layer were found on the mirror surface under the protective bar in both cases, i.e. with D_2 and He injections.
SIMS depth profiles of O, C, MoO and MoC signals measured on the pre-deposited part of the mirror surface after the exposure of the Periscope system with the He gas feeding are shown in Figure 6.10b. All measured depth profiles at locations with the pre-deposited layer that was not sputtered during exposure had similar shapes. The shown case corresponds to a SIMS crater that was made sufficiently deeper than the thickness of the deposited layer, and thus the interface with the substrate can be clearly seen as defined from the decrease of the C signal (Mo substrate signal is not shown). SIMS depth profiles made on the pre-deposited layer before the exposure are shown in Figure 6.10a. These measurements were done on a reference Mo mirror with a thinner a-C:H coating but made under the same conditions. From the two figures, the broadening of the interface is clearly seen from the MoC and MoO signals, thus illustrating the effect of diffusion. To define the thickness of the resulting interlayer, the MoO and MoC signals have to be used since both O and C signals reached saturation during measurements. While the initial thickness of the interlayer was less than 2 nm (Figure 6.10a), the resulting thickness defined from the MoC signal varied from ~6 nm to ~11 nm for different locations on the mirror. The thickness of the oxygen reach layer defined from the MoO signal was systematically smaller and varied from ~5 nm to ~9 nm.

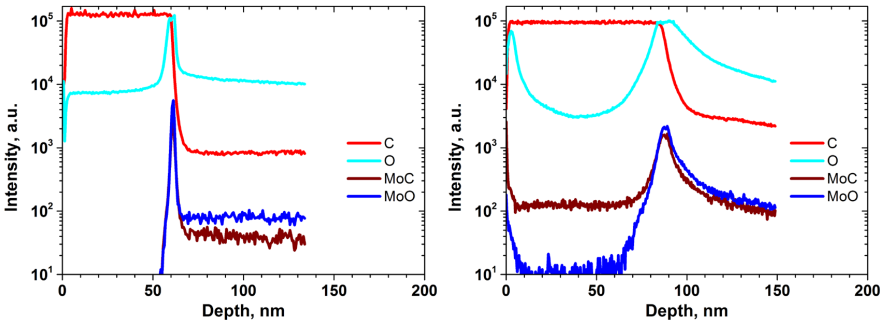

Figure 6.10. SIMS depth profiles of C, O, MoC and MoO measured on the pre-deposited part of the mirror before (a) and after (b) the Periscope system exposure with the He gas feeding. The profiles before and after exposure correspond to different mirrors with deposit thicknesses of about 60 nm (a) and 90 nm (b) but made under the same conditions. An increase of the interlayer thickness is clearly seen, attributed to diffusion of carbon and oxygen through the layer and into the bulk. O and C signals on both figures reached saturation.

Simple calculations of volume diffusion of C in Mo can be done according to Fick's second law of diffusion [Heitjans 2005]:

$$\frac{\partial c}{\partial t} = D\frac{\partial^2 c}{\partial x^2}, \tag{6.14}$$

from which the evolution of the carbon concentration *c(x,t)* in the bulk can be derived as

$$c(x,t) = \frac{M}{\sqrt{\pi D t}}\exp\left(-\frac{x^2}{4Dt}\right), \tag{6.15}$$

where *M* is the areal density of C atoms on the surface, and *D* is the diffusion coefficient. The diffusion coefficient *D* is, in turn, defined as

$$D = D_0 \exp\left(-\frac{H}{RT}\right), \tag{6.16}$$

where, in the case of carbon diffusion in Mo, $D_0 = 3.4 \times 10^{-6}$ m^2/s and the activation enthalpy *H* equals to 171.8 kJ/Mol [Heumann 1992].
From equation (6.15), the penetration depth of diffusing particles can be then defined as

$$\Delta x = 2\sqrt{Dt}\,. \tag{6.17}$$

The pre-deposited mirrors in the experiments with He and D_2 feeding were kept at 200 °C overnight prior to exposure. The mirrors then were kept at an elevated temperature of 380 °C during the entire experiment, i.e. for about 10 hours. According to equation (6.17), the 200 °C overnight heating of mirrors would lead to a negligible penetration depth of carbon into molybdenum of about 0.2 nm. The pre-deposited a-C:D layer remains intact. From the other hand, the heating up to 380 °C during the exposure would result in a penetration depth of

about 530 nm, which is almost two orders of magnitude larger than the interlayer thickness defined from SIMS profiles.
In [Kny 1988] the possibility of conversion of an a-C:H layer on a Mo substrate into the Mo_2C carbide was demonstrated. In the aforementioned work, a partial diffusion of C into the Mo substrate and a build-up of a Mo_2C layer with sharp interfaces a-C:H/Mo_2C and Mo_2C/Mo was observed at 600°C. At 800 °C the entire film was converted into Mo_2C in less than 1 hour. As it was discussed in [Semenenko 2008], the solubility of carbon in molybdenum is very low and at room temperature is only about 10^{-4} at%C. This means that carbon diffused from the pre-deposited layer cannot just largely occupy interstitial positions and thus be "dissolved" in Mo crystallites but would rather be transformed into the molybdenum carbide during the exposure or later during the mirror cooling down. If relatively fast diffusion of C into Mo bulk as calculated for the 380 °C would be assumed, formation of about 500 nm thick carbidized layer might be expected. However, within the uncertainty of the analysis method, which is a combination of SIMS with profilometry measurements of SIMS craters, the thickness of the pre-deposited layer behind the protective bar did not decrease in the discussed experiments, and the interlayer thickness increased only marginally from about 2 nm to about 8 nm. This result can be explained by a combination of two effects: firstly, a possibly slower diffusion of carbon from the interface into the bulk; and secondly, a slower diffusion of C through the Mo carbide.
It was shown in [Reinke 2000] that deposition of even a small amount of carbon (0.8 mono-layer or 0.16 nm) on Mo leads to formation of an a-C layer at room temperature and to immediate formation of molybdenum carbide at elevated temperatures, e.g. at 600°C. The mechanism of carbon transport from the surface into the Mo bulk is described in [Gall 2002]. There are two types of trapping sites for carbon atoms on the Mo surface. The first type of trapping sites is characterized by a strong binding and is filled up first to the maximal C concentration on the surface of 10^{15} cm^{-2}. As a result, the surface carbide is formed (Figure 6.11). In this case the activation energy for carbon diffusion into the bulk is equal to 3.9 eV. All carbon that is held in such type of traps dissolves at a high temperature of 1130°C. The second type of traps is characterized by a weak binding; the traps of this type start to be filled up when the traps of the first type become saturated. The activation energy for diffusion into the bulk for such traps is equal to 2.5 eV. Therefore, for surface concentrations exceeding 10^{15} cm^{-2} carbon atoms start to dissolve at 630-730°C. The volume diffusion of C in Mo has an activation energy of 1.78 eV, which is much lower than the activation energy for diffusion through the surface carbide. Ultimately, it is the transport of carbon atoms from the surface into the bulk that effectively limits the relatively fast diffusion of carbon in the Mo bulk: carbon atoms first have to overcome a higher energy barrier at the surface before they can diffuse into the bulk material. Although the interface between the pre-deposited carbon layer and the substrate material cannot be treated as an open Mo surface, certain boundary effects can be expected. That may result in a similar increase of the activation energy of diffusion that would limit C diffusion deeper into Mo.

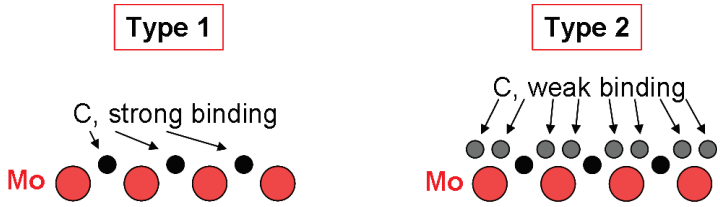

Figure 6.11. An illustration for the two types of trapping sites for carbon atoms on the Mo surface. Type 1 (left): strong binding, is filled first. Type 2 (right): weak binding, is filled when trapping sites of the first type are saturated.

Formation of molybdenum carbide on the mirror surface, in turn, happens already during the C layer growth. Carbon is known to demonstrate slower diffusion in carbides, compared to pure metals [Semenenko 2008]. Quantitatively, the difference in diffusion coefficients of carbon in pure metals and corresponding metal carbides can exceed 10^3 (Figure 6.12). Thus carbidization could inhibit strongly the diffusion of C atoms into the Mo bulk in experiments with the Periscope mirror system.

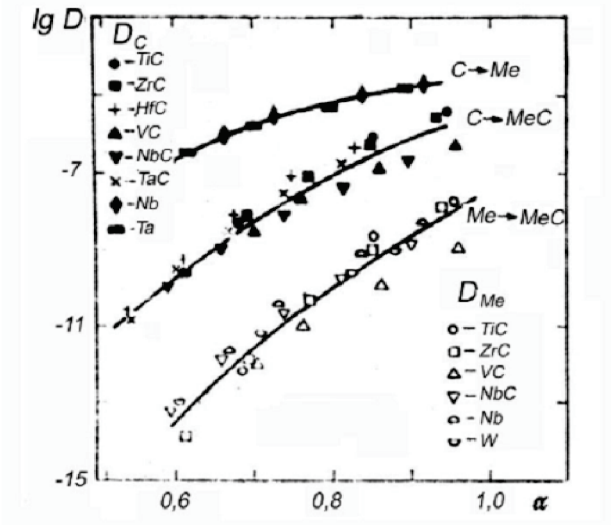

Figure 6.12. The temperature dependence of the diffusion coefficient of carbon atoms in transient metals and carbides, and metallic atoms in carbides. Parameter α represents the temperature of the material in units of its metling temperature: $\alpha = T/T_{melt}$ [Semenenko 2008].

In such a way the combination of the diffusion process with the carbide formation, which slows down the former, can lead to a significant reduction of the penetration depth of carbon particles, thus explaining rather marginal increase of the interface between the pre-deposited layer and the substrate.

As far as the unprotected part of the mirror is concerned, trace amounts of carbon detected on the visually clean mirror surface still might indicate some degree of surface contamination, although could not be quantified with SIMS. This contamination can be attributed to energetic

carbon ions from plasma implanted into the surface. Gas injection through the Periscope affects the plasma parameters (section 6.1.2) and the impact energies of ions, therefore ion implantation can be better studied in the case of erosion experiments.

6.3.2.2 Mirror contamination by carbon and oxygen implantation in erosion experiments in TEXTOR

The average impact energy of C ions on the mirror surface during the erosion experiments was about 400 – 470 eV. According to dynamic SDTrimSP simulations (section 6.2.1), C^{3+} ions with such energies would be implanted into the Mo bulk with a range of about 6 to 7 nm as characteristic for case L1 (see Table 6.5). The range here is defined as the depth under the surface where the maximal concentration of implanted C is observed. The maximal concentration of carbon in this particular case is 29.9 %, and 90% of implanted C is found within 10 nm from the surface (Figure 6.13 and Table 6.7). The depth resolution of the simulated data is 1 nm. The shape of the depth profiles was stabilized after several simulation steps and did not change anymore with the accumulated fluence. The depth profiles are practically similar in the cases with and without re-deposition of Mo. Such behaviour was also observed for other surface binding models used. However, the implantation depth is dependent on the binding energies. To demonstrate this, two extreme cases are shown in Figure 6.14. The results for all the studied binding energy cases are summarized in Table 6.7. The conclusions from these results are the following. The maximum obtained implantation depth corresponding to 90% of implanted atoms is 13 nm for carbon and 12 nm for oxygen, being systematically lower for oxygen in all studied cases. The maximal concentration of implanted atoms varies between 29.9% and 50.1% for carbon and between 7.0% and 11.7% for oxygen.

Table 6.7. Results of SDTrimSP simulations for Mo mirrors: depth profile data.

	№	Case	Surface binding Energy, eV			Re-deposition	Eroded depth, nm	Max. concentration of **C**, %	Coordinate of Max. **C**, nm	Coordinate of 90% **C**, nm	Max. concentration of **O**, %	Coordinate of Max. **O**, nm	Coordinate of 90% **O**, nm
			Mo on Mo	C on Mo	O on Mo								
Low-fluence, T_i=70 eV, Sheath 105 eV	**L1**	1,*	6.81	7.105	4.70		351.62	29.9	6.5	10	7.0	4.5-7.5	9.5
	L3	3,*	Mo(110) 9.18	8.29	5.88		166.21	45.8	9.5	11.5	10.7	7.5	11.0
	L1r	1,*	6.81	7.105	4.70	+	317.69	30.2	6.5	10.5	7.4	6.5	10
	L3r	3,*	Mo(110) 9.18	8.29	5.88	+	128.64	50.1	9.5	12.5	11.7	8.5	11.5
High fluence, T_i=60 eV Sheath 90 eV	**H1**	1,*	6.81	7.105	4.70		648.5	38.0	7.5	9.5	8.4	6.5	9.5
	H1r	1,*	6.81	7.105	4.70	+	563.11	40.0	7.5	10.0	8.9	6.5	9.5

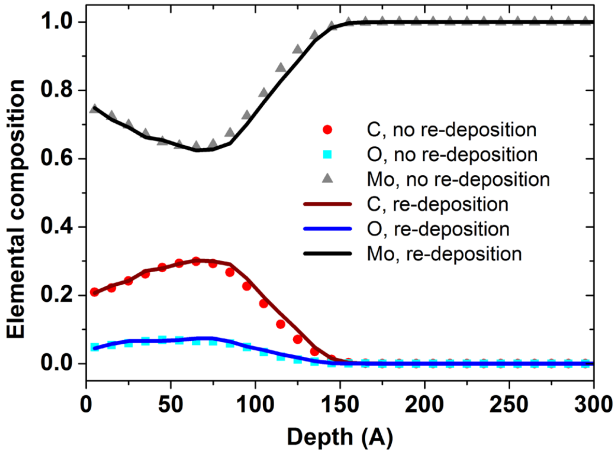

Figure 6.13. Implantation profiles of C^{3+} and O^{3+} ions in a Mo target simulated with SDTrimSP for the case of the low-fluence exposure under erosion conditions.

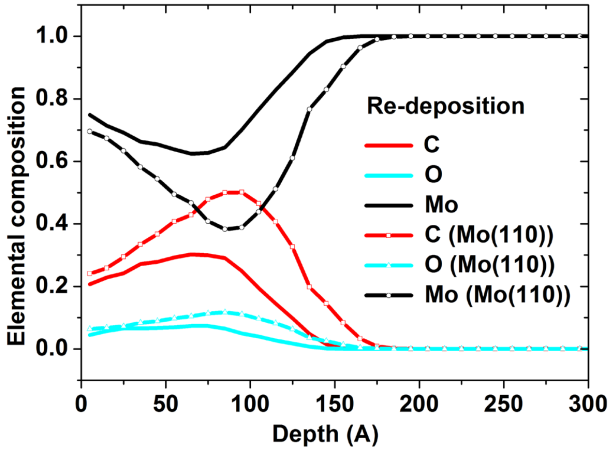

Figure 6.14. Implantation profiles of C^{3+} and O^{3+} ions in a Mo target simulated with SDTrimSP for the case of the low-fluence exposure under erosion conditions for different binding energies: cases L1 and L3.

The notable difference in depth profiles of implanted species is a somewhat shallower ion penetration in the case of the high-fluence exposure (Figure 6.15). This observation is not related to the implantation fluence itself, but should be attributed to different plasma temperatures in the vicinity of the mirrors in both experiments. Lower plasma temperature in the high-fluence exposure corresponds to about 1.2 times lower ion impact energies, in average (400 eV against 470 eV in the low-fluence experiment).

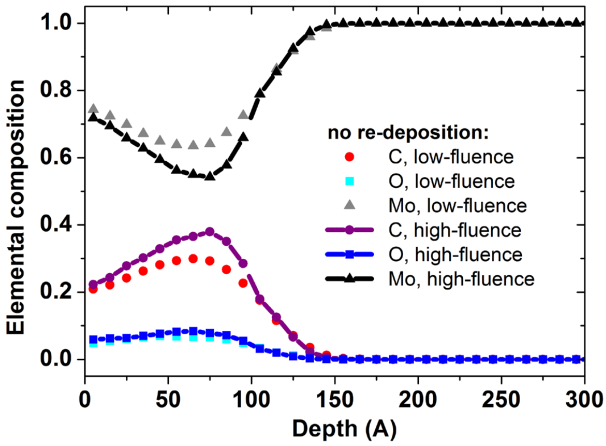

Figure 6.15. Implantation profiles of C^{3+} and O^{3+} ions in a Mo target simulated with SDTrimSP for the cases of low-fluence and high-fluence exposures under erosion conditions for the binding energy E_{sb} (Mo) = 6.81 eV.

In the case of rhodium samples, the same general trends as for Mo samples are observed. Inclusion of the re-deposition in the simulation does not change the depth profile of implanted species. The simulated depth profiles are influenced mainly by the ion impact energies and the binding energy models assumed. As one can see from Figure 6.16 and Table 6.8, the implantation depth of carbon and oxygen is lower in the case of the Rh-coated sample than for Mo. The maximal concentration of implanted C in Rh is observed at about 4.5 - 5.5 nm, and 90% of implanted C is found within 8.5 nm from the surface. The maximal oxygen concentration varied between 2.5% and 5.5%. About 90% of implanted O atoms were distributed within 8 nm from the surface.

Table 6.8. Results of SDTrimSP simulations for Rh mirrors: depth profile data.

	№	Case	Surface Binding Energy,eV			Re-deposition	Eroded depth, nm	Max. concentration of C, %	Coordinate of Max.C, nm	Coordinate of 90% C, nm	Max. concentration of O, %	Coordinate of Max.O, nm	Coordinate of 90% O, nm
			Rh on Rh	C on Rh	O on Rh								
fluence, T_i=70 eV, Sheath 105	**L1-Rh**	1,*	5.78	6.59	4.18		463.3	20.5	4.5	8.5	4.9	2.5	8.0
	L1r-Rh	1,*	5.78	6.59	4.18	+	421.28	22.6	5.5	8.5	5.7	3.5	8.0
High fluence, T_i=60 eV Sheath 90 eV	**H1-Rh**	1,*	5.78	6.59	4.18		880.89	26	4.5	8.5	6.1	4.5	8.0
	H1r-Rh	1,*	5.78	6.59	4.18	+	776.35	27.5	5.5	8.5	6.1	5.5	8.0

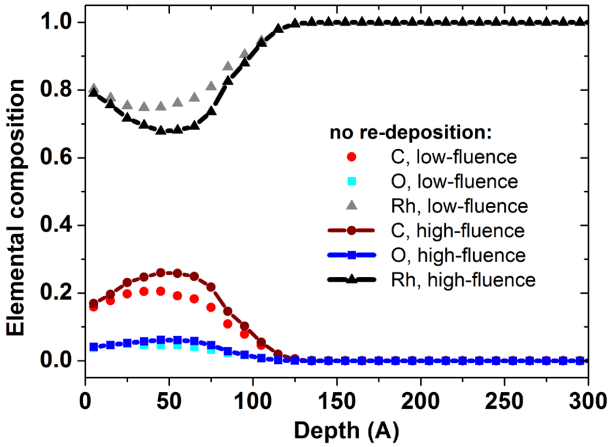

Figure 6.16. Implantation profiles of C^{3+} and O^{3+} ions in a Rh target simulated with SDTrimSP for the cases of low-fluence and high-fluence exposures under erosion conditions for the binding energy E_{sb} (Rh) = 5.78 eV.

As it can be concluded from the SDTrimSP simulations, carbon and oxygen ions get implanted up to 8 – 13 nm deep in the mirror surface. Volume diffusion of C and O in Mo and Rh substrates could stimulate further transport of impurities deeper into the bulk. From the other hand, erosion of the mirror surface leads to a continuous removal of atoms from the top layer of the surface and corresponding dynamic recession of the surface, thus dynamically reducing the effective penetration depth of impurity atoms. It can be seen from SDTrimSP simulations (Figure 6.15) and is also supported by SIMS measurements (Figure 6.17) that the effective penetration depth of C into the Mo bulk remains constant throughout the exposure time. In other words, it does not depend on the fluence in the fluence range of the experiments, indicating the balance between ion implantation, surface diffusion and erosion processes. The thickness of the C layer measured by SIMS is similar in both experiments, and the coincidence of the MoC signal with the C signal suggests that carbon is present on the mirror surface in the form of molybdenum carbide, which is also supported by XPS measurements (section 6.4.2).

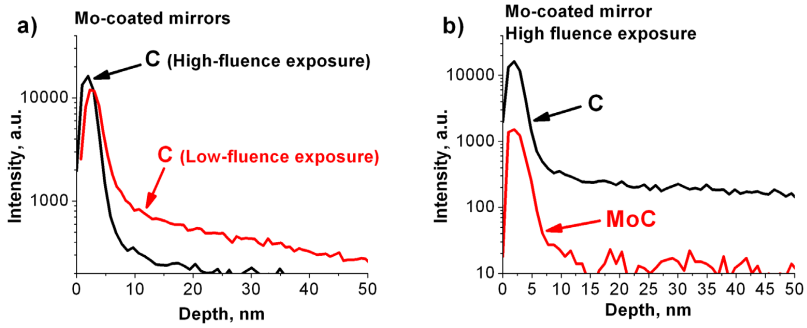

Figure 6.17. SIMS depth profiles of C (a, b) and MoC (b) signals measured on Mo-coated mirrors after low-fluence and high-fluence exposures.

The depth profile of oxygen (Figure 5.7b, Figure 6.18 and Figure 6.19), in turn, indicates presence and diffusion of oxygen atoms in the Mo-coated mirror already before the low-fluence exposure. Measurements performed on the SC Mo mirror used for the high-fluence exposure show a coincidence of oxygen depth profiles before and after exposure (Figure 6.20). In the case of the Mo-coated mirror, the small difference in depth profiles of oxygen before and after the high-fluence exposure (Figure 6.21) is basically within the uncertainty of the analysis. These observations indicate other origin of oxygen than plasma exposure. Most probably it can be attributed to unavoidable oxidation during storage and measurements under air and correspondingly slow diffusion of oxygen at room temperature.

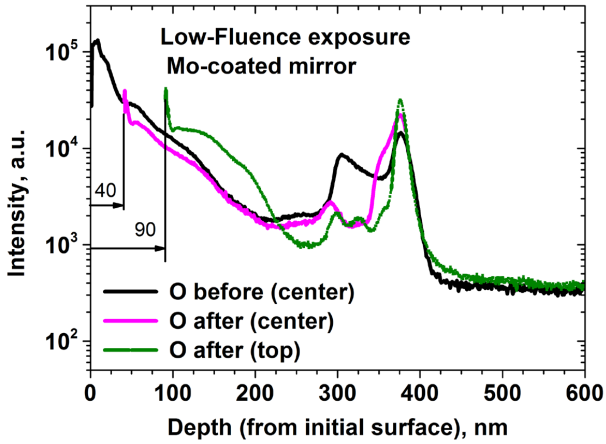

Figure 6.18. SIMS depth profiles of oxygen measured on the Mo-coated mirror before and after the low-fluence exposure.

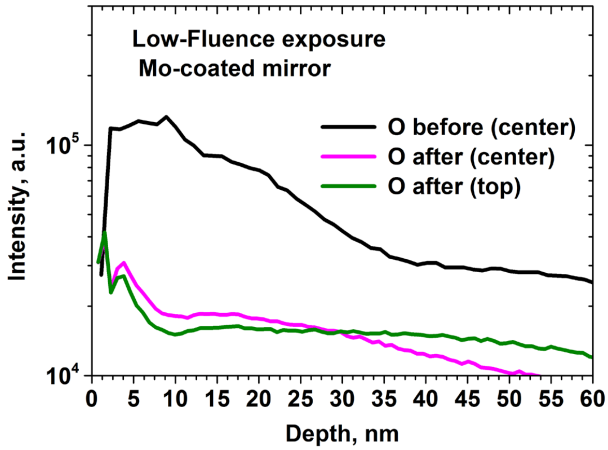

Figure 6.19. SIMS depth profiles of oxygen measured on the Mo-coated mirror before and after the low-fluence exposure. Only surface layer is shown.

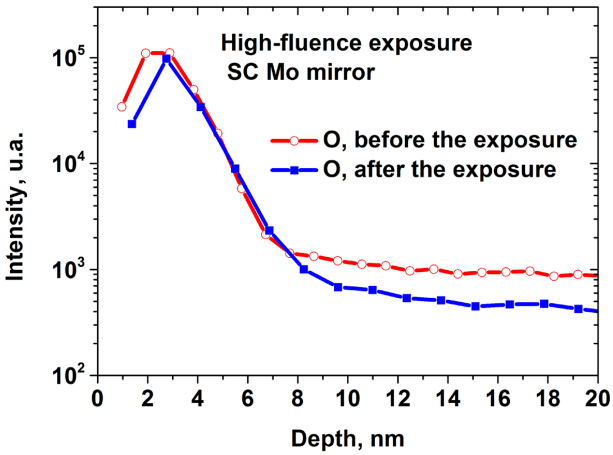

Figure 6.20. SIMS depth profiles of oxygen measured on the SC Mo mirror before and after the high-fluence exposure.

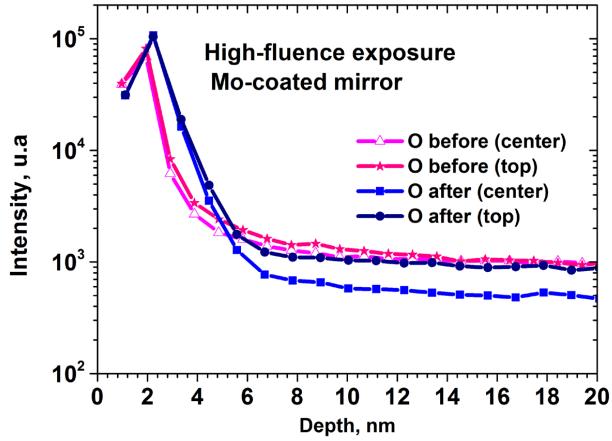

Figure 6.21. SIMS depth profiles of O signal measured on the Mo-coated mirror before and after the high-fluence exposure

However, diffusion of oxygen from the oxidized surface layer deeper into the bulk, as well as diffusion of oxygen atoms implanted into the material cannot be neglected. This conclusion is based on calculations of the diffusion depth of oxygen in conditions of low-fluence and high-fluence exposures. The calculations were performed using different literature data on the diffusion coefficients as summarized in Table 6.9. Results of calculations are presented in Table 6.10.

Table 6.9. Parameters of equation (6.16), diffusion coefficient and activation enthalpy, for diffusion of oxygen in Mo and Mo-oxide according to different literature data.

	[Baranova 1968] O→Mo	[Ying-liang] O→Mo	[Heumann 92] O→Mo	[Elyutin 71] O→MoO_3 Measured at 410–500°C and 0.21–100 atm
D_0 [cm^2/s]	3×10^{-2}	2.8×10^{-2}	3×10^{-2}	9.1×10^{-8}
activation enthalpy *H* [kcal/mole]	31	25.2	22.02	20.3

Table 6.10. Diffusion depth of oxygen in Mo and Mo oxide calculated for single 10 s-long discharges during the low-fluence (T=570°C) and high-fluence (T=1250°C) exposures.

Diffusion depth, nm	[Baranova 1968] $\Delta X_{O\rightarrow Mo}$	[Ying-liang] $\Delta X_{O\rightarrow Mo}$	[Heumann 92] $\Delta X_{O\rightarrow Mo}$	[Elyutin 71] $\Delta X_{Mo\rightarrow MoO3}$
Low-fluence	1.0×10^3	5.4×10^3	14.6×10^3	43
High-fluence	6.4×10^4	16×10^4	28.2×10^4	650

According to the data presented in Table 6.10, fast diffusion of oxygen during discharges must have played a significant role in re-distributing implanted oxygen over the volume of the sample. On the resulting oxygen depth profiles shown in Figure 6.20 and Figure 6.21 a 3-4 nm thick oxygen-reach surface layer could be distinguished, which is attributed to air oxidation.

In overall, the observed depth profiles of oxygen in Mo mirrors are rather similar for measurements done before and after exposure and could be interpreted as a result of several processes taking place during two distinct phases. The first phase is the diffusion of oxygen from the surface layer into the bulk. The surface was initially oxidized, and additionally oxygen atoms were implanted at a depth up to 8-11 nm during the plasma exposures. Heating of mirrors by plasma contributed to fast diffusion of atoms deeper into the material. The second phase covers the period after the samples were withdrawn from TEXTOR. The samples were exposed to air during all optical measurements, and a new oxidized surface layer was unavoidably formed. However, its thickness (4-5 nm) is small and can not have major influence on the mirror reflectivity.

The same reasoning with respect to fast diffusion is applicable to C and O in the case of exposures of Rh-coated mirrors under erosion-dominating conditions. The depth distributions for these cases are shown in Figure 6.22 and Figure 6.23.

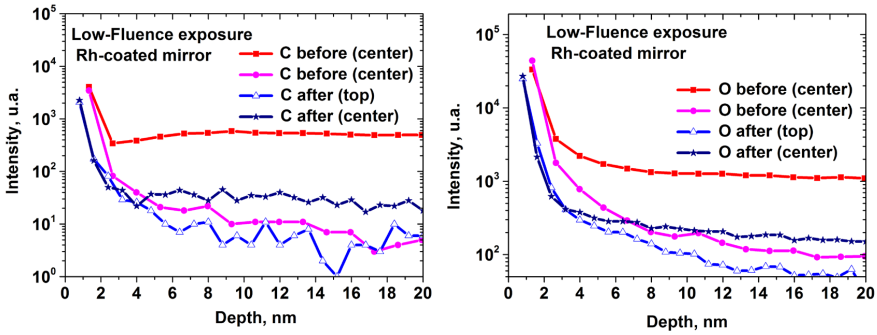

Figure 6.22. SIMS depth profiles of C and O measured on the Rh-coated mirror before and after the low-fluence exposure.

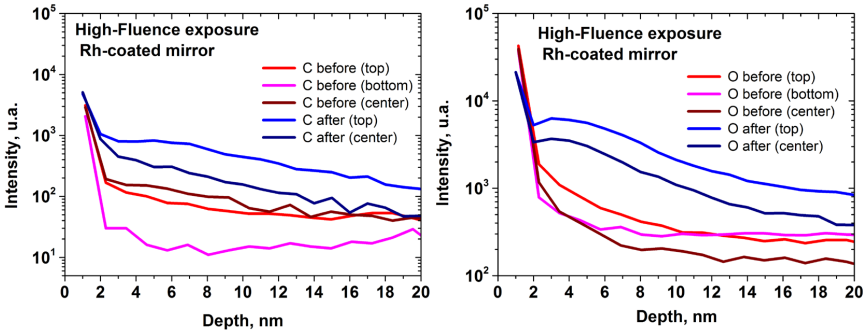

Figure 6.23. SIMS depth profiles of C and O measured on the Rh-coated mirror before and after the high-fluence exposure.

It is a known fact that Rh does not form carbides. The phase diagram of a Rh/C system is shown in Figure 6.24. The solubility of C in Rh is also very low: at 1000°C it is defined to be between 1×10^{-4} and 3×10^{-3} [Burylev 1969] and is practically negligible at lower temperatures. This means that implanted carbon atoms must migrate from the implantation zone or to form precipitates on the surface. High temperatures during the exposures activate the migration of carbon atoms from regions over-saturated by implantation. The time which would be necessary for dissolution of an 8 nm carbon layer formed due to implantation, according to the ion range obtained by SDTrimSP simulations, can be estimated to be about 4×10^{-4} s in the case of the low-fluence exposure and about 7×10^{-8} s in the case of the high-fluence exposure [Rut'kov 2011].

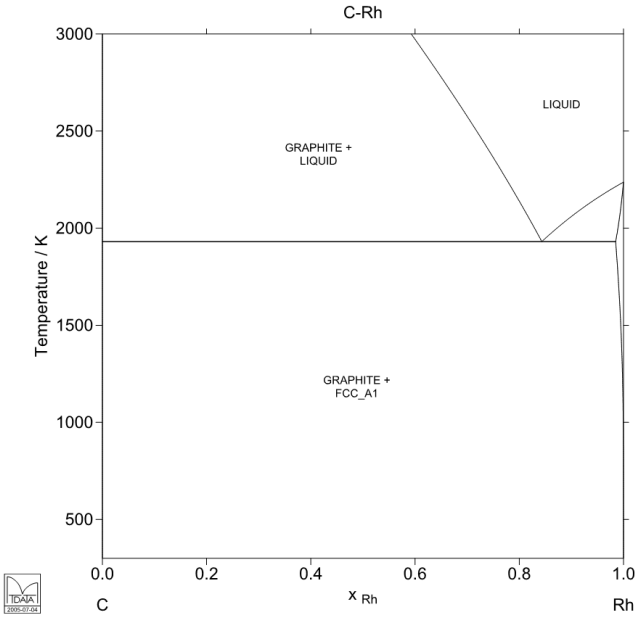

Figure 6.24. Phase diagram of a Rh/C system [MTDATA]

Describing the oxygen content and diffusion in Rh, thermal desorption has to be accounted for, which is activated already at about 420°C. At 1220°C the retained oxygen is completely released [Salanov 1992a]. The complexity of the problem increases when C and O are present and diffuse in Rh at the same time. In addition, boron (B) can be also present at the mirror surface. Boron is used for wall conditioning in TEXTOR and represents an additional impurity in the plasma flux reaching the mirror surface. The situation when C, O and B impurity are present in Rh at the same time is discussed in [Salanov 1992b]. Atoms of these three impurity species occupy interstitial sites in the Rh lattice and therefore obey the same diffusion mechanism. At temperatures above 420°C diffusion of all three species is activated. As a result the diffusion of atoms of each particular element is inhibited due to the fact that they share the same nodal sites within the Rh lattice and therefore block the positions for jumps available otherwise. At a temperature T = 560°C during the low-fluence exposure and at a temperature T = 1340°C during the high-fluence exposure oxygen atoms reaching the surface of the sample are desorbed thermally as O_2 and CO. Boron atoms diffusing to the surface may form boron trioxide (B_2O_3). However, since the implantation profile of carbon is not distinguishable in Figure 6.22 and Figure 6.23, the diffusion process is still very fast despite the inhibition in multi-component systems described above.

6.3.2.3 Mirror contamination during exposure in the oxygen-rich atmosphere

In order to analyze the results of the thermo-oxidation experiment performed in DIII-D, the measured thicknesses of oxidized layers on initially clean Mo mirrors were compared to model calculations. Within the model, it was assumed that the formation of oxide takes place in the reaction front approximation [Linsmeier 2011], i.e. in the diffusion limited regime due to diffusion of oxygen through the growing molybdenum oxide. The diffusion of oxygen was

described according to equation (6.16) based on literature data on oxygen diffusivity in MoO_3 [Elyutin 71] (see Table 6.9). The results of model calculations are given in
Table 6.11 in comparison to experimentally determined values. In the case of mirrors exposed at 160°C, calculations show the result that corresponds very well to the measurements, which means that the volume diffusion of oxygen through Mo-oxide describes the observed phenomena reasonably well. At higher temperatures, however, calculations show significantly stronger oxidation, thus suggesting that other mechanisms, probably surface limited, must be involved.

Table 6.11. Comparison of oxidation depths of exposed molybdenum mirrors as measured in the DIII-D experiment and estimated from model calculations based on the volume diffusion of oxygen through the molybdenum oxide surface layer

Temperature	25° C	160° C	350° C	400° C
Experiment, Δx_{exp} (nm)	-	4	19	-
Diffusion in Mo oxide, Δx_{MoO3} (nm) [Elyutin 71]	1.94×10^{-2}	3.7	137	251

One of possible mechanisms that could influence the oxidation rate of Mo is molybdenum oxide volatilization in the form of various polymers of MoO_3, as well as in the form of hydroxide $MoO_2(OH)_2$, which can be formed due to a reaction of water vapor with MoO_3. The studies on oxidation and volatilization of Mo from the TZM alloy (99% Mo) indicate that volatilization of Mo happens mostly in the form of Mo hydroxide for temperatures below 500°C [Smolik 2000]. The report provides experimental and calculation results for the mass flux of mobilized Mo for temperatures in the range of 400-800°C. Using the data from [Smolik 2000] and assuming the temperature of 400°C as the upper limit, the possible Mo mass transfer from the surface was estimated. The calculations indicate the surface recession rate due to Mo oxide mobilization of the order of only 10^{-2} nm/h. Since the temperature of mirrors during the oxygen bake experiment did not exceed 400°C, the influence of Mo oxide volatilization on the oxidation rate of the Mo surface can be excluded. Interestingly, the oxidation depth of molybdenum at 400°C was estimated in [Smolik 2000] to be 34 nm/h, which is smaller than that calculated from the literature ([Elyutin 71], Table 6.11).

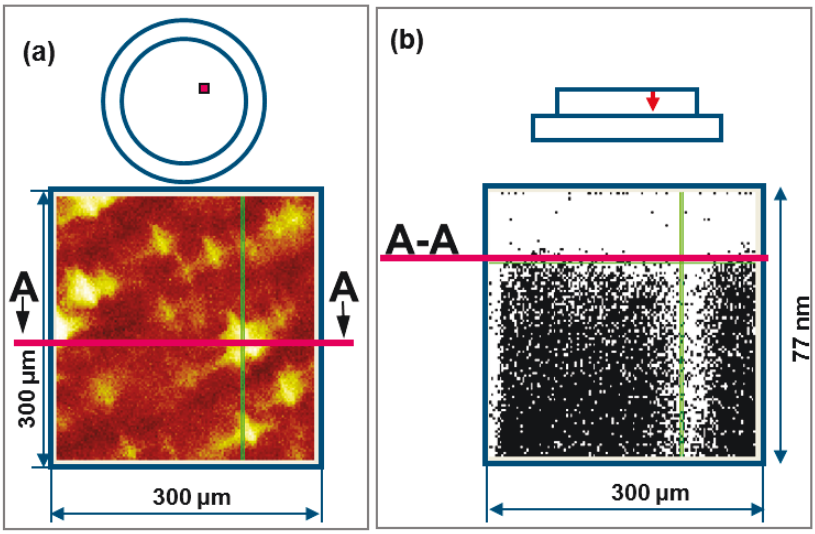

Figure 6.25. (a) The areal map of oxygen content in the PC Mo mirror exposed in DIII-D at a temperature of 350°C, as reproduced from the slice-per-slice evaluation of SIMS data. Darker colors correspond to low oxygen content, and lighter colors correspond to oxygen-rich regions. (b) The cross-section of the same SIMS crater perpendicular to the surface along the line indicated as A-A in figure (a). The black color corresponds to the comlete absence of oxygen, whereas the white color indicates the presence of oxygen. The uppermost white layer above line A-A correponds to the uniformly oxidized surface layer.

The slice-per-slice evaluation of data obtained from a single SIMS crater produced on the surface of the Mo mirror exposed at 350 revealed non-uniform oxidation of the surface. Figure 6.25a shows the areal map of oxygen content in molybdenum. Darker colors correspond to areas with a lower oxygen content, and lighter colors represent oxygen-rich regions. The cross-section of the same SIMS crater perpendicular to the surface along the line indicated as A-A in Figure 6.25a is shown in Figure 6.25b. In this case the black color corresponds to the complete absence of oxygen, whereas the white color indicates the presence of oxygen. About top 15 nm of the surface represent the oxygen-rich layer that was formed almost uniformly all over the surface (the upper white area in Figure 6.25b). In addition to uniform oxidation, deep oxidation channels with a depth of at least 60 nm were detected. The presence of such oxidation channels must be attributed to oxygen diffusion and oxidation along grain boundaries in polycrystalline Mo. It has to be noted that the experimental values Δx_{exp} given in
Table 6.11 correspond solely to the uniformly oxidized surface layer. Thus, the overall oxidation could be governed by a combination of the classical volume diffusion and the diffusion along grain boundaries.

6.3.3 Implantation of hydrogen and deuterium

During exposure in TEXTOR, not only impurity ions but also H and D plasma ions get implanted into the surface of the exposed mirrors. It is known that irradiation of metals with

high fluxes of H or D ions leads to creation of defects in the material, as well as to surface morphology changes, such as e.g. blister formation.
From various hydrogen isotopes implantation experiments with polycrystalline and SC Mo samples [Sugie 2004, Hoshihira 2009, Sharpe 2009, Alimov 2008, Alimov 2009], it becomes evident that appearance of blisters depends on many parameters, among which the intrinsic properties of the material play an important role. It was shown in [Tokunaga 2005] and [Shu 2009] for the case of tungsten that blister formation depends on the crystallographic orientation of grains, surface roughness, grain size, material purity, and sample history, such as manufacturing procedure including polishing that may introduce damage in the material.
The temperature of the sample during the exposure plays an important role in mirror morphology changes. In [Eren 2013] delamination of the Mo coatings made by the magnetron sputtering technique was observed for samples, the temperature of which remained below 200 °C during the exposure. That was not the case for samples that were exposed under higher temperatures. Possible explanation is the following. Implanted D atoms can diffuse along the columnar grain boundaries towards the interface between the coating and substrate. The concentration of D accumulated in the Mo layer by far exceeds the D solubility in Mo, thus leading to additional compressive stresses that cause the film to buckle. D atoms accumulated at the interface may also enhance cracking at this location. In the case of elevated sample temperatures, diffusion of D is fast, so it can reach the surface and leave the sample or diffuse into the steel substrate at much higher rates. This reduces D accumulation in the film itself and at the interface during the exposure and relieves additional stress in the material.
In the case of TEXTOR exposures degradation of coatings was also observed. Delamination of the Mo-coated mirror was observed even before the low-fluence exposure (Figure 5.8 and Figure 5.9). Similarly, delamination of the Rh-coated mirror was detected in the case of the high-fluence exposure (Figure 5.15 and Figure 5.16). The Rh-coated Mo substrate showed the appearance of surface defects in some regions after the low-fluence exposure (Figure 5.11). Few delaminated regions were observed on the Mo coating after the high-fluence exposure (Figure 5.13). These observations indicate that even rather stable coatings made by the magnetron sputtering technique can be damaged after exposure in a tokamak environment.
In [Eren 2011] molybdenum coatings were exposed to a RF deuterium plasma. The mirror samples were biased such that the impact energy of deuterium ions was about 200 eV. The bulk temperature of mirrors was kept at 150°C during the exposure. In [Eren 2013] the ion energy reached 500 eV. Two effects influencing the mirror reflectivity were reported. First, the roughness of the mirror surface increased that lead to an increase of the diffuse reflectivity, which was shown in [Eren 2013] as this process is more pronounced under higher ion impact energies. Second, the total reflectivity of the mirror degraded slightly in the IR wavelength range, by about 2%, that the authors attributed to changes in the electronic band structure of Mo due to presence of implanted D atoms and irradiation induced defects in the material.
Although ion beam and TEXTOR plasma conditions seem to be rather different, the implantation profile and the implantation depth of H and D ions simulated with the SDTrimSP code appear to be quite similar in both cases considered:

- a mono-energetic 200 eV ions as in [Eren 2011];
- a Maxwellian energy distribution corresponding to TEXTOR conditions.

The resulting implantation depth was about 10 nm in both cases. In the case of TEXTOR experiments, however, mirror samples were heated up to much higher temperatures. At a mirror temperature of 500 – 570°C during the low-fluence exposure and 670 – 1250°C during the high-fluence exposure, fast diffusion of hydrogen and deuterium from the implantation zone had to occur. The absence of H and D in the implantation zone of both Mo- and Rh-coated mirror samples exposed in TEXTOR is confirmed by SIMS profiles shown in Figure

6.26, Figure 6.27, and Figure 6.28. Low hydrogen content in the samples is also supported by many thermo-desorption spectra found in the literature (see e.g. Figure 6.29 and Figure 6.30). It follows from the literature data [Pisarev 1984, Ogorodnikova 2009, Sharpe 2009] that at temperatures above 530°C deuterium is not retained in Mo. In particular in the high-fluence exposure the temperature of mirrors was well above this value. This means that most of deuterium would have diffuse out of hot mirror samples during the plasma discharge and subsequent cooling down phase.

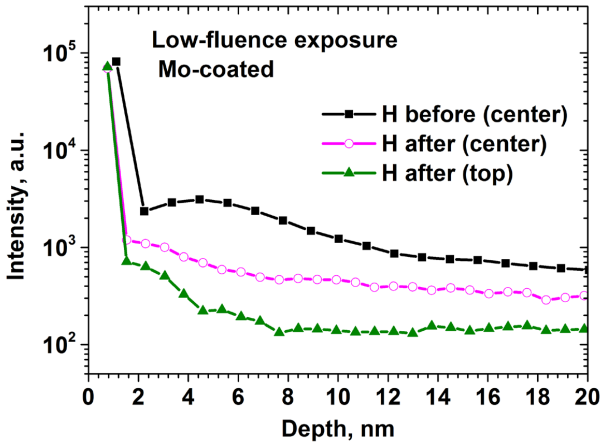

Figure 6.26. SIMS depth profiles of H measured on the Mo-coated mirror before and after the low-fluence exposure.

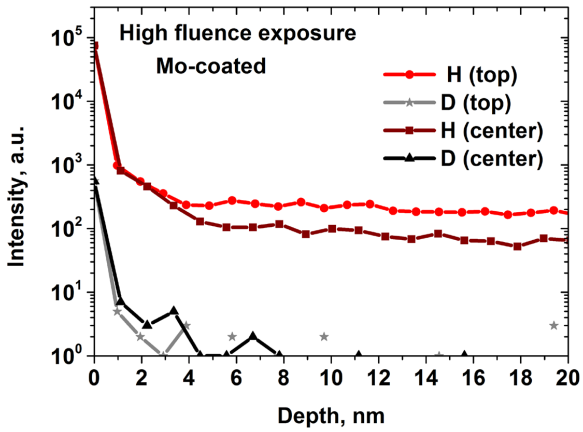

Figure 6.27. SIMS depth profiles of H and D measured on the Mo-coated mirror after the high-fluence exposure.

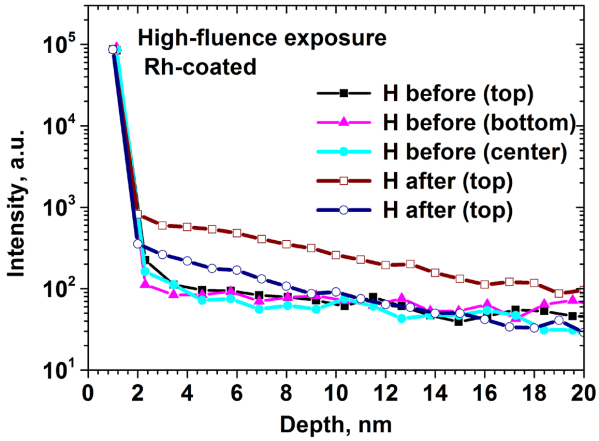

Figure 6.28. SIMS depth profiles of H measured on the Rh-coated mirror before and after the high-fluence exposure.

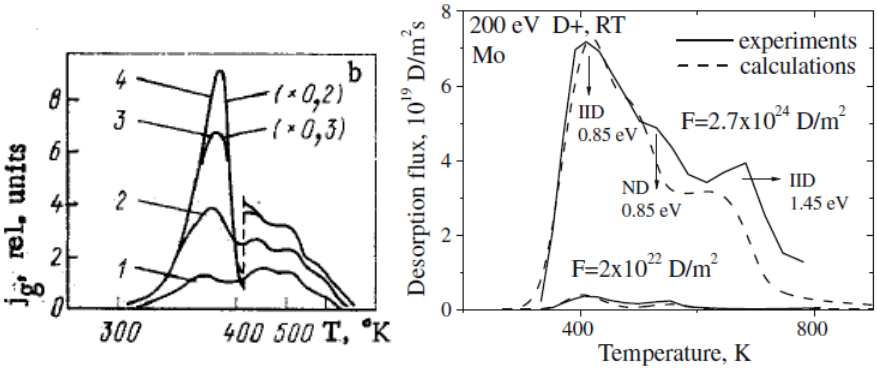

Figure 6.29. Thermodesorption spectra of D from polycrystalline Mo (left) after irradiation in various doses (#1 – 1.4×10^{17}, #2 – 3×10^{17}, #3 – 10×10^{17}, #4 – 30×10^{17} D_2^+/cm^2) by D_2^+ ions having an energy of 15 keV at a sample temperature of 280°C [Pisarev 1984]; and (right) irradiated with 200 eV D^+ ions at room temperature up to fluences of 2×10^{22} D/m^2 and 2.7×10^{24} D/m^2. Dashed lines on the right plot correspond to simulations assuming D trapping at ion-induced defects (IID) and natural defects (ND) [Ogorodnikova 2009].

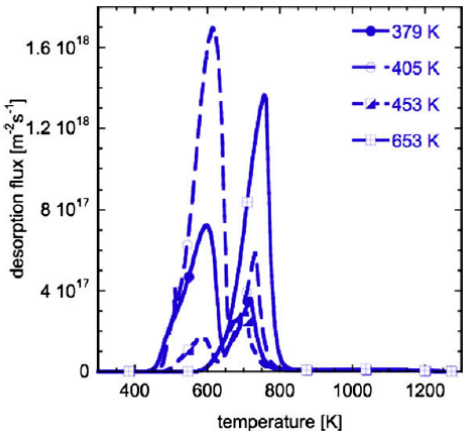

Figure 6.30. Evolution of thermodesorption spectra of D as a function of the temperature of polycrystalline Mo samples during exposure [Sharpe 2009].

Following the arguments given above, one can conclude that D accumulation in Mo described in [Eren 2011] and [Eren 2013] may play a role in the case of low sample temperatures and pure D plasma, but it cannot be claimed responsible for the decrease of the mirror reflectivity in the IR wavelength range observed for SC and coated Mo mirrors in TEXTOR (section 5.1.3, Figure 5.24). In TEXTOR exposures, high mirror temperatures lead to a fast D evacuation from the implantation zone. The conclusion from the results presented in this work is that the presence of other impurities in the surface influenced the reflectivity of Mo mirrors, and the change was at least twice higher than reported in [Eren 2011] and [Eren 2013]. These observations indicate that laboratory experimental results cannot be directly related to exposures in a tokamak.

6.4 Chemical processes

6.4.1 Surface oxidation

Extensive measurements of the mirror properties and surface composition were performed in the dedicated experimental setup. Surface oxidation of the investigated mirrors happens unavoidably during the removal of samples out of TEXTOR, their storage and investigations on air, such as reflectivity measurements, surface profiling and optical microscopy. Moreover, implantation of O ions discussed in Section 6.3.2.2 provides additional source of oxygen even during mirror exposures in TEXTOR.

6.4.1.1 Effects of storage on air

Measurements of the specular reflectivity performed before the low-fluence exposure on the Mo-coated mirror made by the evaporation technique showed a significant deterioration of optical characteristics of the sample compared to the handbook data (Figure 5.7a). Dedicated SIMS measurements of the surface composition detected the presence of oxygen throughout the entire coating, with a strong oxygen peak at the very top layer of the surface and a somewhat smaller peak at the interface with the substrate (Figure 6.18 and Figure 6.19). The presence of oxygen at the interface is explained by oxidation of the substrate before the coating procedure. Oxygen at the surface of the Mo coating, in turn, is likely to be due to oxidation during the storage on air already after the coating procedure. To estimate the thickness of the oxidized layer, calculations using the SprectraRay ellipsometer software were performed. For the model consisting of a MoO_3 layer presumably formed on the pure Mo substrate, ellipsometric calculations indicate the oxide thickness of about 15 nm. Formation of this layer led to a lower reflectivity of the mirror before the exposure as compared to the handbook data. Erosion of this layer during the experiment allowed for a successful recovery of the mirror reflectivity up to the handbook data in the UV and VIS wavelength ranges (250 – 700 nm).

6.4.1.2 Effects of exposure in oxygen atmosphere

The effect of surface oxidation on reflectivity properties of metallic mirrors can be clearly seen on the example of the oxygen bake experiment in DIII-D described in section 5.3. The measurements performed after the exposure showed a significant drop of the reflectivity for all exposed mirrors. The most affected were the ultra-violet and visible wavelength ranges (Figure 5.40 and Figure 5.41). In general, molybdenum mirrors appeared to be less prone to oxidation than copper mirrors.
Deterioration of optical characteristics of mirrors starts from a reflectivity drop in the UV wavelength range when the oxide layer starts to grow and then spreads further to VIS and finally to IR wavelengths with increasing thickness of the oxidized layer. The similarity of the influence of oxygen content in the surface on optical characteristics of Mo mirrors can be clearly seen for the cases of the on-air storage (section 6.4.1.1., Figure 5.7a) and oxygen bake (Figure 5.40).

6.4.1.3 Oxide formation during erosion experiments

To investigate the surface composition after the coating procedure and after exposures in TEXTOR, XPS measurements were performed on mirrors used for the low-fluence and high-fluence exposures. These measurements were performed in the University of Basel using an ultra-high vacuum chamber with a hemispherical analyser (Leybold EA10/100 MCD) and a non-monochromatized x-ray source (Mg K_α excitation, $h\nu = 1253.6$ eV). For the electron binding energy calibration, the Au $4f_{7/2}$ peak was set to 84.0 eV. The typical energy resolution in these XPS measurements is 0.8 eV. Samples were investigated as received. To identify the presence of different chemical components chemical shifts were used.

Measurements of coated mirrors were done directly after the coating procedure without breaking the vacuum. Measurements after exposures were performed on the mirrors extracted from TEXTOR. These mirrors were stored on air for some time, necessary for optical measurements.

The spectrum of the Mo $3d_{5/2}$ core level measured after the coating procedure embraced peaks corresponding to pure Mo and molybdenum oxide. The difference between the measured binding energies of oxide and pure Mo material was less than that between MoO_2 and Mo known from the literature data [Wagner 1979]: about 0.5 eV instead of 1.4 eV. This fact can be attributed to the lack of oxygen, amount of which in the ultra-high vacuum chamber was not sufficient to form a fully oxidized layer of MoO_2. For the evaluation of the Mo $3d_{5/2}$ core level spectra, the doublet separation due to the spin-orbit splitting of 1.15 eV was used according to the literature [Wagner 1979, William 1971].

From the fitting procedure performed with the CasaXPS and Unifit software for measurements performed after the coating procedure, two surface components were obtained, indicating the metallic and the molybdenum oxide phases.

The molybdenum trioxide formation was detected with XPS after the exposure in TEXTOR on all the exposed Mo mirrors, which is illustrated in Figure 6.31 and Figure 6.32. The surface composition of all the investigated mirrors before and after the low-fluence and high-fluence exposures based on XPS measurements of the Mo $3d_{5/2}$ core level is shown in Figure 6.32. The molybdenum trioxide formation prevails over molybdenum dioxide in most of cases. It has to be noted that after the exposures the difference between the binding energies of dioxide and pure material corresponds well to the literature data, suggesting that the amount of accumulated oxygen was sufficiently high to form the oxidized layer with stoichiometry 1:2.

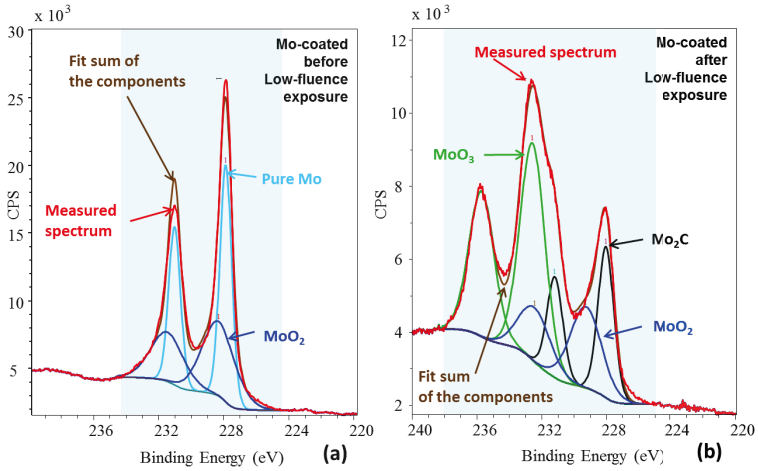

Figure 6.31. XPS measurements of Mo $3d_{5/2}$ core level signals measured on the Mo-coated mirror as-coated (a) and after the low-fluence exposure (b). The red line represents the measured spectrum after the subtraction of sattelites. Different simulated surface components are shown in blue, black and green, while the brown line is the resulting envelope (the summ of all components). Similar results were obtained for Mo-coated mirror before and after the high-fluence exposure, as well for SC Mo mirror.

The presence of Mo $3d_{5/2}$ core level peaks in measurements of the Rh-coated mirrors (Figure 6.32) can be attributed to re-deposition of Mo atoms, which originate from sputtering of the Mo-coated or SC Mo mirrors placed nearby or, even more probably, from the metallic plate made of the TZM alloy (~99%Mo, ~0.5%Ti, ~0.08%Zr, and traces of C), which fixes the mirrors on the test limiter (Figure 5.5).

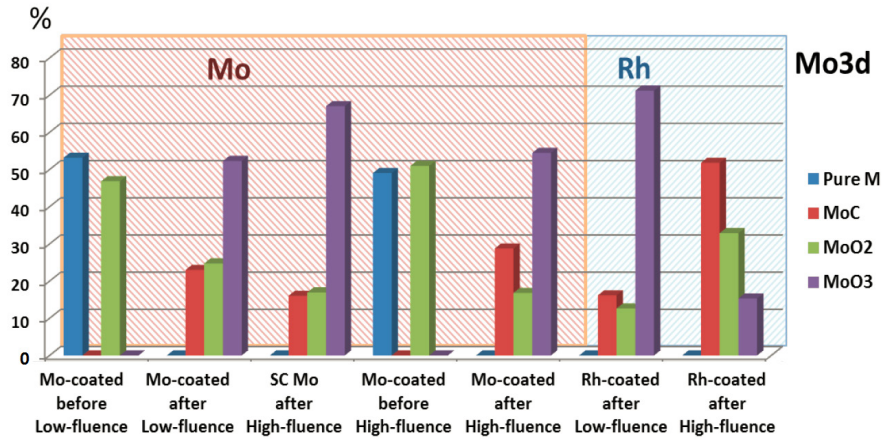

Figure 6.32. Surface composition of mirrors before and after the low-fluence and high-fluence exposures, based on XPS measurements of the Mo $3d_{5/2}$ core level.

XPS measurements of the large SC Mo mirror after the exposure were performed with a PHI ESCA 5600 system at IPP Garching. The photo-ionization process was induced by an Al Kα X–ray source. The resulting spectra were recorded with a hemispherical energy analyser. Survey spectra were recorded with a pass energy of 187.85 eV and core level spectra with a pass energy of 23.50 eV. The energy axis of the system was calibrated with respect to the Au $4f_{7/2}$ core level at a binding energy of 84.0 eV. The linearity of the energy axis was verified using the Cu $2p_{3/2}$ signal at 932.7 eV and the Ag $3d_{5/2}$ signal at 368.3 eV. All three reference core levels are reproducible with an uncertainty of 0.1 eV. To remove surface adsorbates, Ar^+ ions with a kinetic energy of 10 keV were used. The total fluence on the measurement spot was 2.3×10^{15} Ar^+/cm^2. The scheme of the measurements and the particle fluences accumulated during the exposure in TEXTOR and corresponding to locations of measurements are shown in Figure 6.33.

Measurement results show that part of molybdenum on the surface is in form of MoO_2; no MoO_3 signals were resolved (Figure 6.34 as compared to Figure 6.31). The difference with measurements done on the Mo-coated and SC Mo mirrors after the low-fluence and high-fluence exposures can be explained by pre-sputtering of the large SC Mo mirror surface before measurements to remove the surface adsorbates. This is indicated by the shoulder of the peak corresponding to the MoO_3 shift that was present on the survey spectra of the large SC Mo mirror collected before the bombardment of the mirror surface with Ar^+ ions.

In the spectrum of the Mo $3d_{5/2}$ core level, three doublets can be found which correspond to boride Mo_2B_5 at 227.2 eV, carbide Mo_2C at 228.2 eV and oxide MoO_2 at 229.1 eV. The differences between the found binding energies and the corresponding literature data do not exceed 0.1 eV: for Mo_2B_5 and MoO_2, for which the binding energies of 227.3 eV and 229.1 eV are expected [Wagner 1979]. For Mo_2C binding energy of 228.1 eV is expected [Reinke 1999].

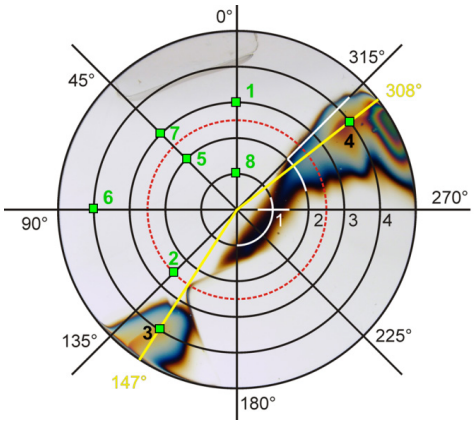

Measurement	Coordinate	Fluence, 10^{24} cm^{-2}
1	(3, 0°)	4.75
2	(2.5, 135°)	2.32
3 (Deposition)	(4, 147°)	1.80
4 (Deposition)	(4, 308°)	3.54
5	(2, 45°)	3.94
6	(4, 90°)	3.63
7	(3, 45°)	4.66
8	(1, 0°)	3.36

Figure 6.33. Scheme of XPS measurements of the large SC Mo mirror after the exposure and accumulated particle fluences corresponding to locations of measurements.

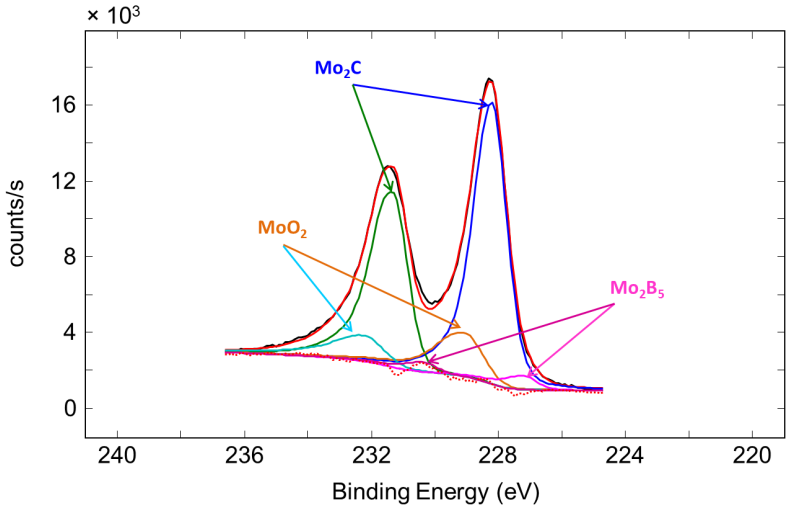

Figure 6.34. XPS measurements of Mo $3d_{5/2}$ core level made on the large SC Mo mirror after the exposure. An exemplary measured spectrum after subtraction of satellites (black line) for measurement point #1 is shown. Colour lines correspond to three surface components, with the red line representing the resulting envelope. Red dotted line is residuum. Similar signals were measured at all investigated locations within the erosion zone on the mirror surface.

The resulting surface composition obtained from the Mo $3d_{5/2}$ core level spectra evaluation is presented as a histogram in Figure 6.35. The presence of oxide was detected on all the measurement locations except point #3 where the strong surface contamination by the deposited carbon layer lead to almost complete absence of the Mo signal. At point #4 weak Mo signal was detected, which could be explained by re-deposition from near-by erosion locations during the mirror exposure in TEXTOR. The thickness of the deposited a-C:H layer at locations #3 and #4 of more than 100

nm would not allow to see the Mo $3d_{5/2}$ signal originating from the mirror surface itself since the XPS technique allows to resolve only first 5 – 7 nm of the surface. Traces of Ti were found at all the measured locations in the erosion-dominated zone (#1, #2, #5, #6, #7, and #8) indicate re-deposition of particles sputtered from the mirror holder and a fixation system made of the TZM alloy. Since Mo is the main component of TZM, its re-deposition over the mirror surface can be also expected and thus explains the presence of a weak Mo $3d_{5/2}$ signal even at location within the deposition-dominated area of the mirror surface (Figure 6.35, location #4). No Mo signal found at location #3 is explained by a rather distant location of this point with respect to the protruding fixation clamp of the mirror holder.
The presence of Mo_2B_5, which is also shown in Figure 6.35, was also supported by measurements of the B 1s core level spectra. Formation of molybdenum boride is justified by the boron implantation due to its presence in the plasma of TEXTOR, as it was discussed in section 6.3.2.2.

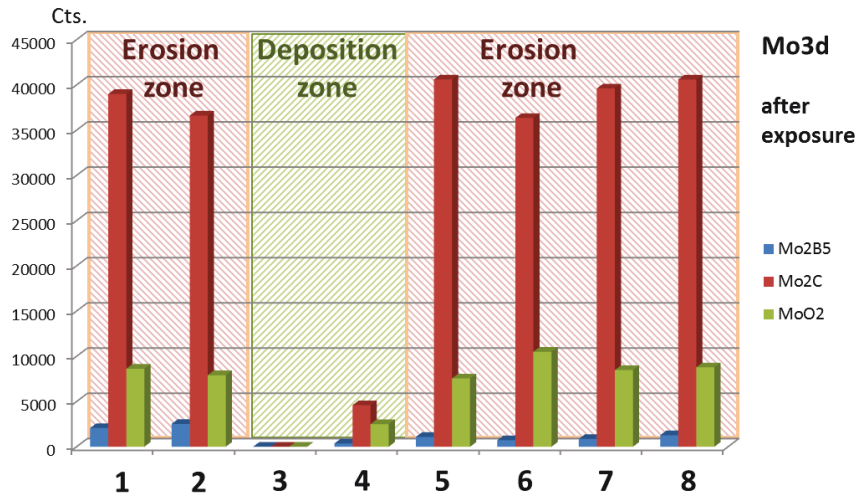

Figure 6.35. Surface composition of the large SC Mo mirror after the exposure, based on XPS measurements of the Mo $3d_{5/2}$ core level.

In summary, the formation of molybdenum oxides was detected on all the mirrors used for the exposures under erosion conditions. The presence of MoO_3 was detected after the exposures only on those mirrors, which were not pre-sputtered before XPS measurements. Thus the formation of MoO_3 could be attributed to the air storage. The formation of MoO_2 was found on all Mo mirrors before and after the exposures. The presence of Mo_2B_5 and boron oxides was detected on the large SC Mo mirror after the exposure. Boron originates from the background plasma impurity in TEXTOR, and therefore should be similarly present on all other Mo mirrors. However, measurements of the B 1*s* core level for the mirrors after the low-fluence and high-fluence exposures were not performed. Although no B 1*s* signal can be detected, presence of low amounts of B cannot be completely excluded due to the low signal to noise ratio at the position of the B 1s peak on the survey spectra and the low photo-ionization cross-section of B.

6.4.2 Carbidization of molybdenum mirrors

For all Mo mirrors used in the experiments under erosion-dominated conditions (section 5.1), a similar decrease of the specular reflectivity of about 4 % in the IR wavelength range was observed, regardless of the amount of material eroded during the exposures (Figure 5.7a, Figure 5.10, Figure 5.14b, Figure 5.19, Figure 5.23b, Figure 5.24f). The most probable mechanism leading to such a reflectivity change in the studied cases is the change of the surface elemental composition in the presence of carbon impurities. A similar behaviour of the specular reflectivity of Mo-C co-deposits was observed in [De Temmerman 2005] (Figure 3.6).

As it was shown in section 6.3.2, the implantation mechanism under TEXTOR conditions ensures the presence of carbon atoms up to the depth of about 10 nm into the mirror surface. The solubility of C in Mo is very low, which is reflected in the phase diagram in Figure 6.36. For example, the solubility at room temperature is $\sim 10^{-4}$ at%C [Semenenko 2008], and the maximal solubility of 0.2 at%C could be reached at temperatures of about 2500 K.

The amount of Mo atoms per 1 cm^2 surface area within the implantation depth of 10 nm is equal to 6.4×10^{17}, which is derived from the molar volume of Mo of 9.4 cm^3/mol. The maximum amount of carbon atoms which could be dissolved in this volume (0.2 at%) is then equal to 12.8×10^{14}. Assuming that the SOL in TEXTOR contains in average about 3% carbon impurity in the plasma flux, the amount of carbon atoms coming to the mirror surface can be estimated as 1.4×10^{17} $cm^{-2}s^{-1}$ in the low-fluence exposure and 1.7×10^{17} $cm^{-2}s^{-1}$ during the high-fluence exposure. This means that all the vacant places for interstitial carbon atoms in Mo will be occupied already after about 9×10^{-3} seconds. Incoming carbon atoms in excess of the solubility limit will contribute to the molybdenum carbide formation. On the time scales of less than 10^{-2} seconds, the diffusion process can be neglected. Thus, depending on the carbide stoichiometry (MoC or Mo_2C) 3.2×10^{17} or 6.4×10^{17} carbon atoms are required for full carbidization of molybdenum within the carbon implantation zone. Such an amount of carbon atoms comes to the mirror surface during 2-4 seconds of plasma, which is less or comparable with the typical duration of one TEXTOR discharge. From these simplified calculations it can be concluded that the carbidization of the surface of molybdenum mirrors placed under erosion conditions in TEXTOR could be expected.

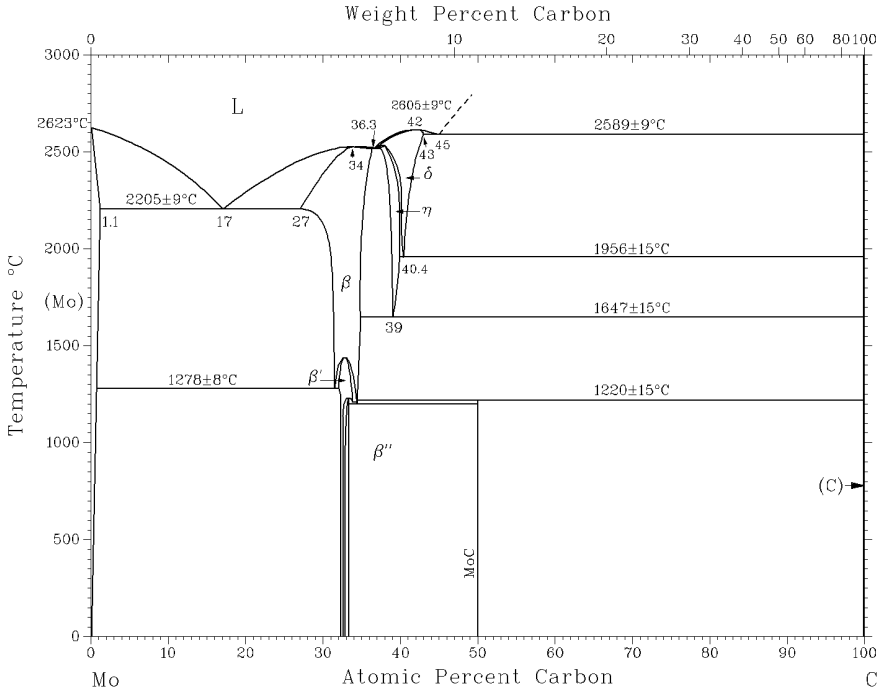

Figure 6.36. The phase diagram of a Mo/C system [BAPD].

6.4.2.1 Low-fluence and high-fluence exposures

XPS measurements performed on the plasma-exposed samples after their storage on air revealed the presence of the molybdenum carbide peak on all Mo-coated and SC Mo mirrors (Figure 6.37). As expected, no molybdenum carbide was detected on Rh-coated mirrors. To fit the measured XPS spectra, the binding energy range was set to 284.2-284.3 eV for pure graphitic C, 285.2 eV for disordered C, and 283.0 -283.2 eV for Mo_2C [Reinke 1999, Reinke 2000, Luthin 2001]. Following the same literature data, the shift of the core C 1*s* level due to carbide formation should be 1.1 - 1.2 eV. This shift was found in all the XPS measurements of Mo mirrors. In Figure 6.37, the left peak denoted as C-O- is attributed to adsorbates, which are unavoidable on the surface of the sample and influence the shape of C 1*s* peak. The binding energy of the fitted C-O- peak lies in the range of 287.8 - 288.5 eV, which is in a good agreement with the literature data for binding energies of carbon oxide (287.7 eV or 290.2 eV) and dioxide (291.8 eV) [Wagner 1979].

The graphitic (ordered) as well as disordered carbon atoms were detected on Mo and on Rh surfaces. The fitted binding energy of graphitic C was found to be in the range 284.5 - 284.8 eV, which deviates a bit from the literature data due to a biased calibration of the system. However, the difference between ordered and disordered peaks of 1.0 eV confirms the correct identification of graphitic and disordered carbon components. These two states of carbon could be attributed to implanted carbon atoms, part of which could agglomerate and form small ordered inclusions in the Mo

or Rh matrixes, and to small fraction of carbon atoms at the surface, which most probably were deposited during the ramp-down phase of the last discharge.

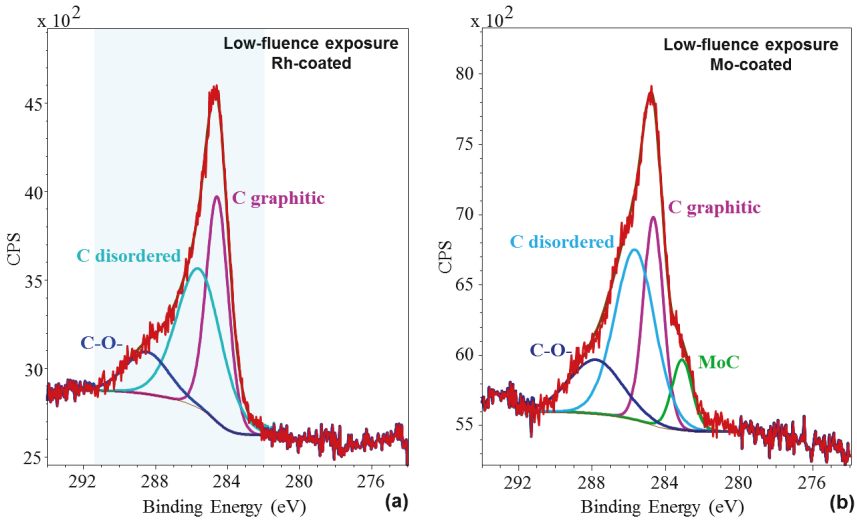

Figure 6.37. XPS measurements on the Rh-coated (a) and Mo-coated (b) mirrors after the low-fluence exposure. The C 1*s* core level peak is shown. The red line shows the measured spectrum after the subtraction of satellites. Other colour lines show different fitted components with the brown line (invisible behind the red line) representing the resulting envelope. The shape of the right shoulder of the peak indicates the presence of molybdenum carbide on the Mo-coated mirror, and its absence on the Rh-coated mirror. Similar signals were measured for coated mirrors after the high-fluence exposure, as well for SC Mo mirror.

Figure 6.38 summarizes the surface composition of all types of investigated mirrors based on the C 1s core level after the low-fluence and high-fluence exposures. The signal of disordered C (deposited carbon) prevails over graphitic C because in XPS the signal is exponentially higher for near-surface atoms.

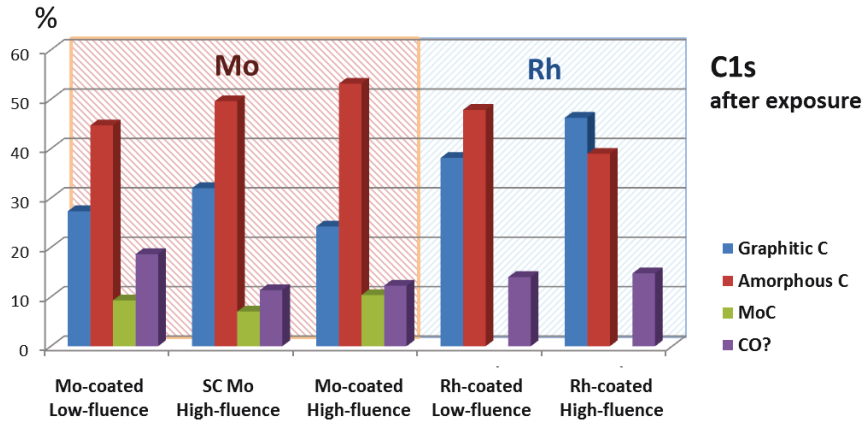

Figure 6.38. Surface composition of mirrors after the low-fluence and high-fluence exposures, based on XPS measurements of the C1s core level.

The presence of molybdenum carbide on Mo mirrors is in agreement with XPS measurements of the Mo $3d_{5/2}$ core level presented in section 6.4.1.3. Molybdenum carbide could not be resolved from the C 1*s* core level spectrum on Rh-coated mirrors due to its negligible amount, but the Mo $3d_{5/2}$ spectra (see Figure 6.31 and Figure 6.32) indicate that formation of molybdenum carbide happened on all the exposed mirrors: the Rh-coated mirrors were contaminated by re-deposited Mo atoms.

6.4.2.2 Large SC Mo mirror

XPS measurements performed on the large SC Mo mirror after the exposure in TEXTOR also showed the presence of carbides. The typical shape of the C1*s* core level peak measured in the erosion-dominated zone after removal of surface adsorbates is shown in Figure 6.39. Carbon is presented mostly in the form of molybdenum carbide; but graphitic and disordered carbon states were also detected. Figure 6.40 corresponds to the measurement made in the deposition-dominated zone. There is just a tiny amount of molybdenum carbide, which should be attributed to re-deposited Mo atoms. The majority of deposited carbon is in the graphitic state; the contribution of disordered carbon is about 10 %. Figure 6.41 shows the resulting surface composition at all measured locations. The atomic ratio Mo/C in the carbide state is equal to 1.33 ± 0.05 on the eroded area and 1.52 for location #4 corresponding to the deposition zone. From the Mo_2C carbide state determined from the chemical shift of the C1*s* peak, the Mo/C ratio of 2:1 is expected. Comparison of signal intensities points to the direction of formation of a substochiometric carbide phase.

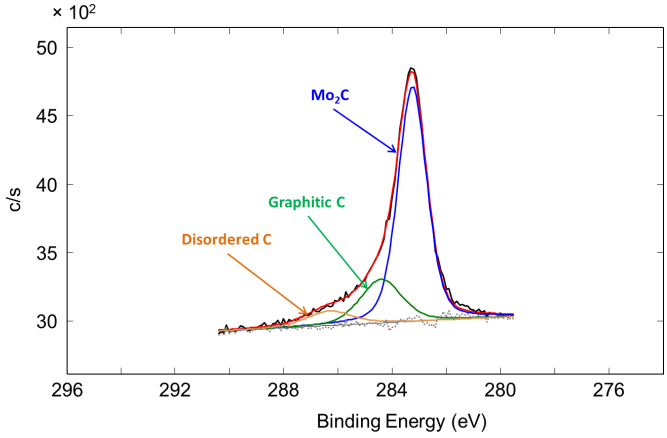

Figure 6.39. XPS measurements of the C 1*s* core level peak made on the large SC Mo mirror after the exposure. The black line shows the measured spectrum at location #1 after the subtraction of satellites. Colour lines correspond to different fitted components, with the red line representing the resulting envelope. Dotted lone is residuum. Similar spectra were measured at all locations in the erosion-dominated zone on the mirror surface.

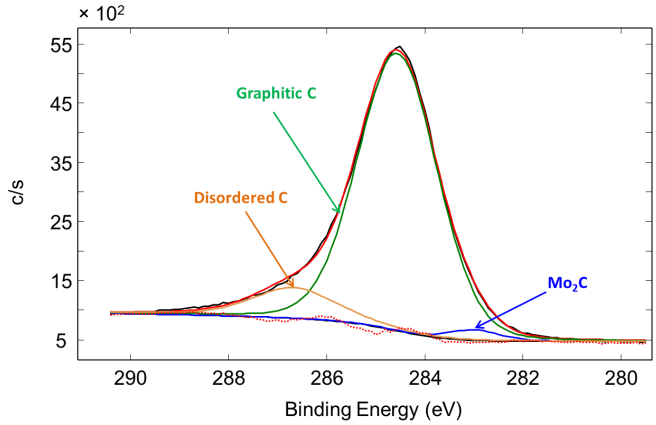

Figure 6.40. XPS measurements of the C 1*s* core level peak made on the large SC Mo mirror after the exposure. The black line shows the measured spectrum at location #4 after the subtraction of satellites. Colour lines correspond to different fitted components, with the red line representing the resulting envelope. Similar spectrum was measured at location #3 also situated in the deposition-dominated zone.

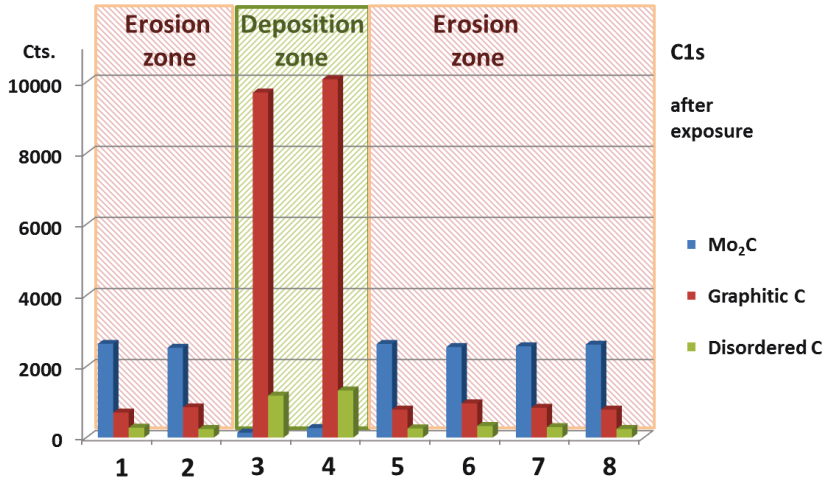

Figure 6.41. Surface composition at different locations on the surface of the large SC Mo mirror after the exposure, based on XPS measurements of the C 1*s* core level.

6.4.2.3 Periscope mirror system

XPS–measurements of the first Mo mirrors after exposures in the Periscope system with D_2 and He gas feeding were also performed at the IPP Garching. The schemes of measurements and the typical shapes of the Mo $3d_{5/2}$ core level peaks measured at locations clean from deposits after removal of surface adsorbates are shown in Figure 6.42 and Figure 6.43. In the case of the D_2 gas feeding, the shape of the peak was similar for all measured locations, and there was practically no difference between the pre-deposited areas cleaned during the exposure (locations #1 and #5) and initially clean areas where deposition was mitigated by the gas feeding (locations #2 and #6). In the case of the He gas feeding, the shape of the peak measured at location #2 was also very similar, except for a minor amount of MoO_3 detected. It should be noted, that the measurement at location #4 on the mirror after the exposure with the He feeding could not be performed and had to be excluded from the analysis.

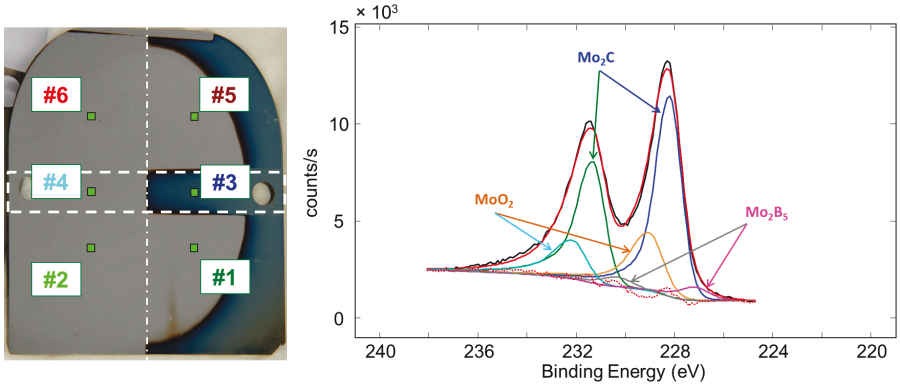

Figure 6.42. Locations of XPS measurements for the 1st mirror after exposure in the Periscope mirror system with the D_2 gas feeding (left), and the Mo $3d_{5/2}$ core level peak measured at location #6 (right). Measurements at location #6 is representative for all other erosion locations (#1,#2, #4, and #5).

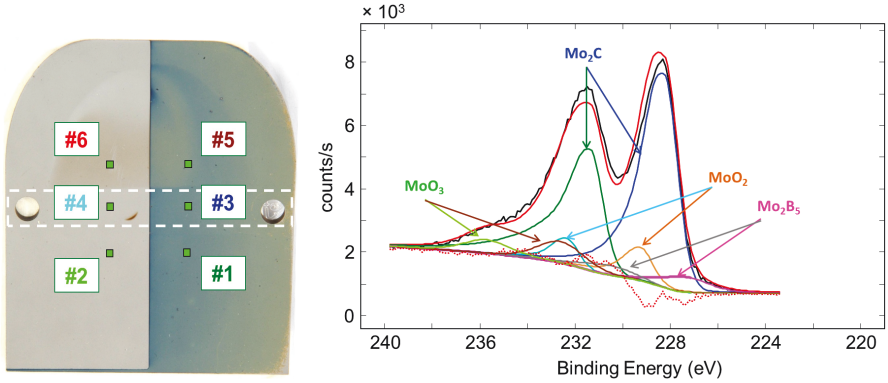

Figure 6.43. Locations of XPS measurements for the 1st mirror after exposure in the Persicope mirror system with the He gas feeding (left), and the Mo $3d_{5/2}$ core level peak measured at location #2 (right).

The surface composition resulting from the Mo $3d_{5/2}$ core level spectra evaluation is presented in Figure 6.44 for the case of the D_2 injection and in Figure 6.45 for He. The presence of molybdenum carbide was detected at all measured locations, except for location #3 in the case of the D_2 feeding, which is explained by the absence of Mo in the surface layer (pre-deposited carbon layer under the protective bar). The surface composition at location #2 after the exposure with the He feeding is very similar to results obtained for the erosion-dominated zone in the case of the D_2 feeding. This means that the mechanism of carbidization of Mo is similar in both cases and should be attributed to implantation of carbon originated from plasma, rather than to re-deposition of chemically eroded C atoms during the D_2 exposure. Much weaker Mo contribution at location #6 in Figure 6.45 is explained by the formation of a thin

deposited carbon layer on the surface, which screens the Mo substrate. Minor Mo signatures detected at locations #1 and #5 in this case should be attributed to the re-deposition process, which must have contributed to the Mo $3d_{5/2}$ core level peak also at location #6.

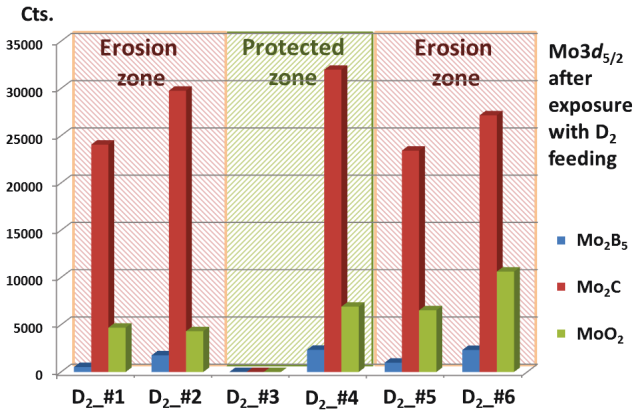

Figure 6.44. Surface composition at different locations on the surface of the 1st mirror after exposure in the Periscope system with the D_2 gas feeding, based on XPS measurements of the Mo $3d_{5/2}$ core level.

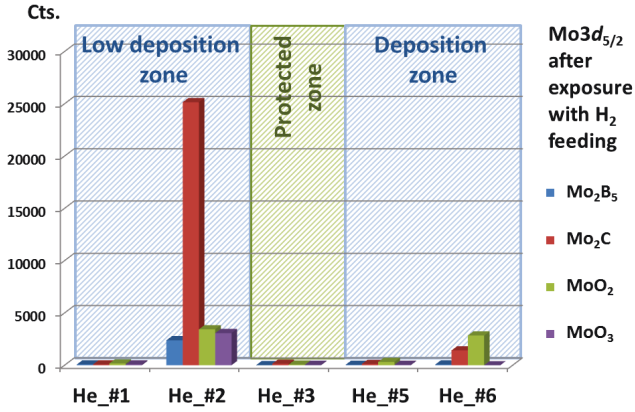

Figure 6.45. Surface composition at different locations on the surface of the 1st mirror after exposure in the Periscope system with the He gas feeding, based on XPS measurements of the Mo $3d_{5/2}$ core level.

Boron implantation into the mirror surface was detected on all areas which were not covered with the protective bar on both mirrors (locations #1, #2, #5, and #6). The presence of Mo_2B_5 was supported by measurements of the Mo $3d_{5/2}$ and B1*s* core level spectra.

The evaluation of the C 1*s* core level spectra showed that at locations free from deposited carbon layers carbon is mostly present in the form of molybdenum carbide;

graphitic and disordered carbon are also detected. An exemplary spectrum for the case of the He feeding is shown in Figure 6.46. A similar spectrum measured in the deposition zone (He feeding) is shown in Figure 6.47. There is just a tiny amount of molybdenum carbide detected, which should be attributed to re-deposited Mo atoms. The majority of carbon is in graphitic and disordered states, about 35% and 43%, correspondingly. The results with respect to the surface composition obtained from measurements at all locations at the mirror surface in both cases (D_2 and He feeding) are summarized in Figure 6.48 and Figure 6.49.

The results of measurements presented here for both 1st mirrors used for the Periscope system exposures, with the D_2 and with the He gas feeding, allow concluding that the carbidization of an initially clean Mo surface happens due to implantation of C ions originating from plasma. However, the amount of such a way formed carbide is much smaller in this case than in the case of the large SC Mo mirror (see Figure 6.41) due to mitigation of carbon implantation by the gas feeding, which eventually leads to preservation of the mirror reflectivity (see Figure 5.32b).

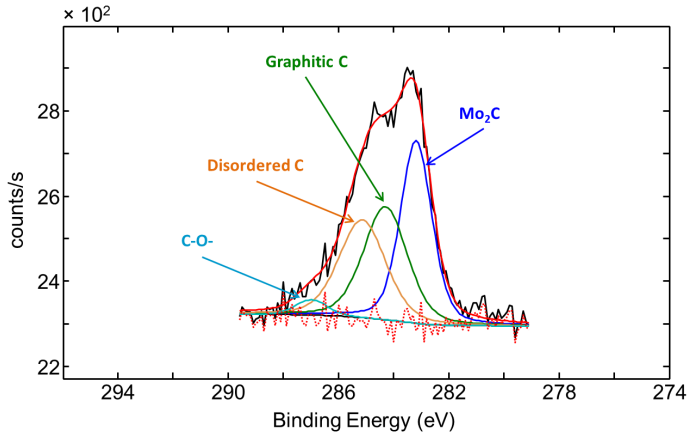

Figure 6.46. XPS measurements of the C 1*s* core level peak made on the 1st mirror after the exposure with the He gas feeding. The black line shows the measured spectrum at location #2 after the background subtraction. Colour lines correspond to different fitted components, with the red line representing the resulting envelope.

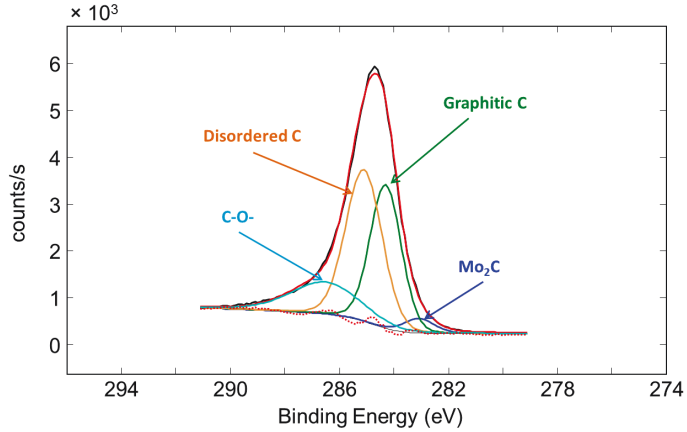

Figure 6.47. XPS measurements of the C 1*s* core level peak made on the 1st mirror after the exposure with the He gas feeding. The black line shows the measured spectrum at location #5 after the subtraction of satellites. Colour lines correspond to different fitted components, with the red line representing the resulting envelope.

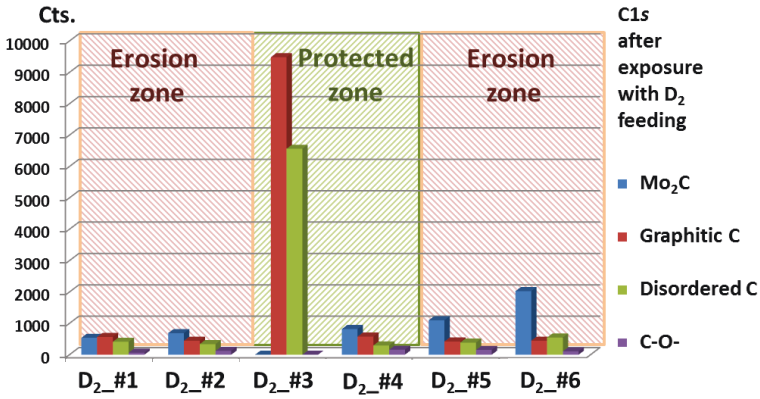

Figure 6.48. Surface composition at different locations on the surface of the 1st mirror after the exposure in the Periscope system with the D_2 gas feeding, based on XPS measurements of the C 1*s* core level.

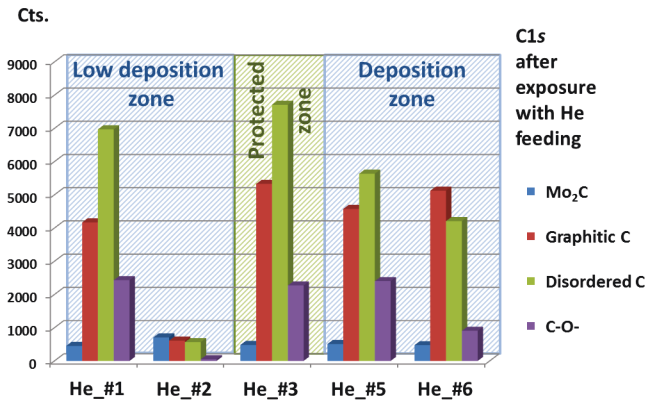

Figure 6.49. Surface composition at different locations on the surface of the 1st mirror after the exposure in the Periscope system with the He gas feeding, based on XPS measurements of the C 1*s* core level.

Chapter 7. General discussion

The results of the experiments presented and analysed in the two previous chapters are colligated here summarizing the impact of this work on general understanding of plasma-material interaction processes and related surface modifications. Conclusions with respect to roles of different physical processes in modification of the elemental composition of a material surface exposed to plasma are presented along with the discussion about their effects on optical properties of the surface.

7.1 Effects of erosion

7.1.1 Surface roughening

It was observed earlier that sputtering of polycrystalline materials leads to surface morphology changes. In general, the surface roughness increases, which is attributed to inhomogeneous sputtering of differently oriented grains of the material. It was shown in section 5.1.3 that nano-coatings, which are characterized by nanoscale-small grain sizes, behave similarly to polycrystalline materials, i.e. that they are sputtered inhomogeneously due to different orientations of crystallites. In contrast, single-crystals (SC) are shown to be sputtered homogeneously and therefore can preserve the smoothness of their surface. It has to be noted, however, that sputtering of SC surfaces in conditions of high erosion yields or high fluences when large amounts of material are removed can also lead to an increase of the surface roughness. The maximum fluences at which SC surfaces acceptably preserve their flatness and roughness still have to be determined experimentally.
The development of a surface relief has an immediate effect on the optical properties of the surface. Roughening of the surface causes a pronounced decrease of the specular reflectivity due to the fact that surface irregularities enhance the diffuse scattering of the incident light. In particular, in experiments with coated mirrors presented in the previous chapters a reduction of the specular reflectivity of Rh-coated mirrors by 10 - 25% was measured in the ultra-violet (UV) and visible (VIS) wavelength ranges (Figure 5.24). Mo-coated mirrors also demonstrated noticeable decrease of the reflectivity up to about 10% in the UV wavelength range. The experiments with SC Mo mirrors explicitly demonstrated the advantage of SC materials, namely the homogenous sputtering. The reflectivity of the mirrors was preserved in the UV and VIS wavelength ranges irrespective of the amount of eroded material, within the fluence range accessed in the experiments. This speaks in favour of SC materials not only in the case of mirrors exposed under net-erosion conditions, but also in the case of sputter cleaning of mirrors in deposition-dominated zones.

7.1.2 Removal of surface adsorbates and oxides

Surface adsorbates and oxides represent the unavoidable initial surface contamination of as-received materials. Such layers modify the electronic structure of the material and therefore have in general different reflectivity properties in comparison to clean materials. This difference in properties becomes greater, the greater is the thickness of the surface layer

subjected to the modification. This concerns, in particular, the penetration depth of light defined by the extinction coefficient of the associated electro-magnetic wave. In order to assess the properties of the material itself, the contaminated surface layers have to be removed, e.g. by physical sputtering of the material surface under erosion-dominated conditions in plasma. It was observed during this work that as-received material samples indeed can demonstrate the reflectivity properties below the literature data and that reduced reflectivity properties of initially contaminated mirrors can be improved after exposure under net erosion conditions. These effects were clearly demonstrated on the example of the Mo-coated mirror (see sections 5.1.3.1, 6.3.2.2 and 6.4.1.1).

7.2 Influence of deposition

With respect to the interaction of light with matter, thin material layers are different from thick samples due to their translucency. If there is a deposited layer on the surface of the material, the incident light rays can penetrate through the layer and therefore interact both with the layer and with the substrate material. The light passes the surface layer at least twice during the reflection process, being progressively attenuated: considering the incident ray and the one reflected from the substrate. Ultimately, the reflected light represents a superposition of light rays reflected from the layer itself and from the substrate material. The situation becomes even more complicated in the case of multiple layers involved. The reflectivity of a surface with a deposited layer on it represents a strong function of the layer thickness (section 3.2.2). For an unquantified deposition the reflectivity of the surface is unpredictable. This means that to ensure the desired reflectivity properties of the surface the thickness of the deposited layer has to be controlled or the deposition has to be mitigated completely, which can be, in particular, achieved by shifting the balance of surface processes to net erosion.
In this work it has been demonstrated that the balance between erosion and deposition processes can be shifted towards beneficial erosion by injection of gaseous impurities in the vicinity of a mirror. Such an approach has a twofold effect:

- the flux of particles capable of being deposited can be reduced;
- the injected gas can stimulate additional mechanisms for removal of deposited species, e.g. by means of the chemical erosion process (only reactive gases and certain impurity species).

In the case of experiments described and analysed in sections 5.2 and 6.1.2, both these possibilities were demonstrated on an example of mitigation of deposition of carbon by means of injection of different gases. In the case of injection of the He gas, which is non-reactive and does not lead to chemical erosion of carbon, deposition of carbon layers was significantly mitigated, although no complete mitigation was achieved. Introduction of the D_2 gas was, in turn, capable of complete mitigation of deposition and even cleaning of pre-deposited layers on the mirror surface. Such a substantial effect is attributed to chemical erosion of carbon layers by D ions, which are present in plasma itself and the amount of which was increased after ionization of injected D_2 molecules, thus leading to stronger chemical erosion of carbon. It has to be noted, however, that the effectiveness of this technique for mitigation of deposition of high-Z impurities (e.g. tungsten) still has to be demonstrated along with estimates and analyses of maximum expected concentrations of such impurities in the plasma flux to the mirror surfaces.

7.3 Effects of particle implantation

Implantation of energetic particles into the surface implies collision cascades and material mixing in the damaged surface layer, which lead to changes of the elemental surface composition. As it can be concluded from SDTrimSP simulations described in section 6.3.2.2, carbon and oxygen impurity ions from TEXTOR plasma get implanted up to 8 – 13 nm deep in the mirror surface. However, continuous dynamic recession of the surface due to physical sputtering processes may reduce the effective penetration depth of implanted impurities. According to SDTrimSP simulations (Figure 6.15) and SIMS measurements (Figure 6.17) the resulting effective penetration depth of carbon into Mo remains almost constant during the exposures. Optical characteristics of mirrors, which are very sensitive to the surface composition, also appear to be very similar for all SC Mo mirrors in the performed erosion experiments. This fact supports the SDTrimSP and SIMS results and suggests that the balance between ion implantation, diffusion and erosion processes was achieved such that similar thicknesses of thin carbide layers could be established on the surfaces of mirrors in all erosion experiments, being independent from the fluence of eroding particles in the fluence range achieved.
The fact that optical characteristics of all SC Mo mirrors in performed erosion experiments appear to be very similar supports the SDTrimSP and SIMS results about same thicknesses of carbide layers formed on Mo mirrors in all erosion experiments where mirrors were exposed to different fluxes of particles.
Dedicated laboratory experiments [Eren 2011 and Eren 2013] showed possible minor changes of the reflectivity of Mo due to accumulation of implanted D in the near-surface region. Such mechanism may play a role for laboratory experiments with pure D plasma and low sample temperatures. In TEXTOR exposures (section 6.3.3.), however, these conditions are not relevant. High mirror temperatures must have led to immediate evacuation of D from the implantation zone due to thermo-desorption. The measured reflectivity changes are at least twice higher than reported in [Eren 2011] and [Eren 2013], thus suggesting that unavoidable implantation of impurity ions from plasma, such as carbon and oxygen is decisive for the reflectivity changes.

7.4 Influence of diffusion processes

Diffusion of implanted or deposited particles can lead to impurity transport deeper into the bulk, thus increasing the thickness of the affected surface layer. Diffusion process also can drive the formation of distinct chemical phases. Two effects can slow down the volume diffusion of impurities:

- slower diffusion from the surface or interface into the bulk;
- slower diffusion through already formed chemical phases, e.g. carbides or oxides.

In the experiments with the Periscope mirror system, an assumption of the simple volume diffusion of C in Mo results in almost two orders of magnitude larger expected diffusion depth of carbon than the measured thickness of the carbon interlayer formed between the deposited layer and Mo substrate during the experiment (section 6.3.2.1). Slower diffusion of carbon from the interface into the bulk [Gall 2002] and slower diffusion of C through the Mo carbide [Semenenko 2008] are known in the literature and thus may explain the observed discrepancy, although the interface between the pre-deposited carbon layer and the substrate material cannot be treated as an open Mo surface.

Formation of molybdenum carbide on the mirror surface takes place already during the plasma exposure when carbon is deposited on the surface or implanted in the near-surface layer [Reinke 2000]. Diffusion of carbon in carbides goes slower than that in pure metals [Semenenko 2008]. Quantitatively, the difference in the diffusion coefficient of carbon in pure metals and in corresponding metal carbides can exceed 10^3 (see section 6.3.2.1). The same effect of slowing down the oxygen diffusion in Mo oxides was discussed in section 6.3.2.3. The difference in diffusion coefficients of oxygen in pure metals and corresponding metal oxides can exceed 10^5 [Elyutin 71]. Thus carbidization and oxidation of the Mo surface can inhibit strongly the diffusion of C and O atoms into the Mo bulk.
However, volume diffusion can be also enhanced. In particular, in this work the effect of fast diffusion along grain boundaries [Landolt-Boernstein] was found to exist in the case of O diffusion in polycrystalline Mo (section 6.1.2.3.).

7.5 Effects of the surface chemistry

Implantation and diffusion of impurity atoms in the material may lead to formation of chemical compounds with electronic and optical properties different from that of the initial material. In the case of tokamak exposures described in this thesis, formation of compounds with the main surface contaminants, carbon and oxygen, can be expected. A carbidized surface, e.g. Mo_2C, has different optical properties compared to Mo (Figure 3.6). In particular, the extinction coefficient shows different wavelength dependence, and so does the skin depth (Figure 7.1). It can be seen from Figure 7.1 that light penetrates more than 9 nm under a Mo_2C surface in the wavelength range 250-1700 nm, which is deeper than the thickness of the carbon-containing layer observed in the erosion experiments (see e.g. Figure 6.17 (b)). This means that the light reflected from such a contaminated mirror represents a superposition of waves reflected from the carbide layer and from the underlying Mo. This effect explains the measured change of the optical characteristics of SC Mo mirrors (sections 5.1.3. and 6.4.2.). Because of similar effective implantation depths of carbon ions in the range of studied plasma parameters according to SDTrimSP simulations (Figure 6.15), similar thicknesses of carbide layers were established (Figure 6.17) - a result of simultaneous implantation/carbidization at slow diffusion and erosion of the surface. This conclusion is also supported by SIMS measurement. The attainment of a stationary value of the reflectivity of about 4% below the handbook data was characteristic for all SC Mo mirrors exposed under erosion-dominated conditions. Such a moderate degradation regardless of the amount of the eroded material supports the finding that similar elemental and chemical composition of studied samples was achieved for the range of particle fluences covered by the experiments.

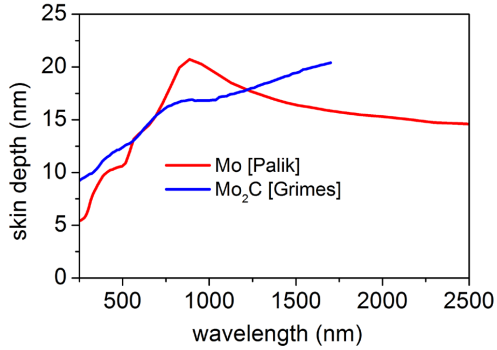

Figure 7.1. The skin depth as a function of the wavelength, as calculated from the extinction coefficient data for Mo [Palik] and Mo_2C [Grimes 2004].

It should be noted that surface roughening of SC Mo in presence of carbon in the plasma flux can happen as a result of inhomogeneous sputtering due to non-homogeneous carbidization. This effect was observed in [Bardamid 2002] for the case of sputtering of 5 μm of the SC Mo surface by 5×10^{24} D^+/m^2 and wide energy spectrum of 0.1-1.5 keV. MoC_2 inclusions formed on the surface had lower sputtering rates then non-carbidized surface areas and therefore started to protrude above the surface. The range of conditions in which non-homogeneous carbidization can take place has to be identified since installation of SC Mo mirrors at such locations may lead to faster degradation of their reflectivity.
In contrast to the effect of surface carbidization in plasma, strong surface oxidation of mirror samples exposed in DIII-D during the thermo-oxidation experiment (no plasma) described in section 5.3 was confirmed by SIMS analyses. A significant drop of the mirror reflectivity of up to 50% for Mo mirrors and up to 90% for Cu mirrors was measured, which was attributed to oxidized surface layers (section 6.3.2.3.). Surface oxidation was found to be non-homogeneous with deep oxidation channels formed, presumably, due to diffusion of oxygen along grain boundaries.

7.6 Summary

In this work it was demonstrated that a variety of physical processes may influence the reflectivity of metallic surfaces in the plasma environment of a tokamak. Ultimately, there can be two global effects leading to changes in the reflectivity properties of a material.
The first global effect is related to the surface morphology and represents modification of the surface relief. Surface roughening leads to a reduction of the specular reflectivity due to diffuse scattering of the incident light off an uneven surface. When the wavelength of the probing light is comparable with the typical length scale of the surface relief, diffuse reflection involves also purely physical effect of light diffraction. It was illustrated earlier in this thesis that the typical mirror surface relief can be characterized by a mean root square roughness of few tens of nm at maximum (Section 6.1.3). Therefore, for the range of wavelengths of interest starting from 250 nm, the light diffraction processes can be neglected. The main reason for modification of the surface relief of a surface exposed to plasma or any other source of energetic particles is the non-homogeneous sputtering of the surface. In the case of polycrystalline materials, the surface is composed by a series of differently oriented crystallites, or grains, which are sputtered with their own rates depending on their crystal orientation. It was shown in this work that coatings with nano-sized crystallites behave similarly to polycrystalline materials and that the resulting increase of the surface roughness can lead to a significant drop of the specular reflectivity. In the case of experiments described in this thesis, a 25% decrease of the reflectivity of Rh-coated mirrors was measured in the UV wavelength. Noticeable degradation of the reflectivity was observed also for Mo-coated mirrors. SC Mo mirrors are expected to exhibit homogeneous sputtering. Indeed, the reflectivity of SC Mo mirrors studied in this work was preserved in the UV and VIS wavelength ranges irrespectively of the amount of eroded material. It should be noted, however, that sputtering of SC mirrors in conditions of high erosion yields or high fluences when large amounts of the material can be removed can also lead to an increase of the surface roughness, although with a much weaker rate as compared to that of polycrystalline materials.
The second global effect is of chemo-physical nature and represents the modification of the elemental composition of the material surface. The underlying physical and chemical phenomena are related to the modification of the electronic structure of the material: the penetration depth of the incident light is affected due to changes of the extinction coefficient for the associated electromagnetic wave. There can be various reasons for changes of the

surface elemental composition, among which the following interrelated processes and conditions can be mentioned:

- Presence of surface adsorbates and oxidized layers on the initial surface;
- Implantation of energetic particles from plasma into the surface;
- Formation of deposited layers on the surface;
- Diffusion of implanted and deposited atoms;
- Formation of chemical compounds, such as carbides or oxides, at the surface and in the bulk during and after the plasma exposure.

In all these cases, changes of the reflectivity are the stronger, the greater is the thickness of the surface layer subjected to modification of the elemental composition. This can be illustrated on the example of oxide formation in the experiment with thermo-oxidative wall conditioning presented in this thesis. The actual penetration depth of light also represents an important parameter. It was calculated that in the case of carbidized layers formed on the mirror surface during erosion experiments, the probing light could penetrate deeper than the thickness of the affected surface layer. This means that the light reflected from such a contaminated mirror surface must be represented by a superposition of waves reflected from the carbidized layer and from the underlying initial mirror material. The reflectivity of a surface with a deposited layer thus represents a strong function of the layer thickness. This means that for an unquantified deposition the reflectivity of the surface is unpredictable.
The thickness of the affected or deposited layer is actually controlled by the balance between various processes. The energy of impacting particles determines the particle implantation depth. Volume diffusion of deposited and implanted impurity atoms can stimulate the impurity transport deeper into the bulk material. The impurity transport in the material can, in turn, feed and stimulate the formation of chemical phases. It was demonstrated in this work that formation of chemical phases such as carbides and oxides can finally slow down the volume diffusion. However, fast diffusion along grain boundaries can be expected in the case of polycrystalline materials. Sputtering of the surface represents the main driver for surface roughening and is also a competing process contributing to the surface composition change. In the case of erosion experiments, similar thicknesses of carbide layers were established on all mirrors independent on the particle fluence as a result of the balance of physical processes such as simultaneous implantation, carbidization at slow diffusion and erosion of the surface.
Sputtering of the surface by plasma ions as well as chemical erosion lead to removal of surface adsorbates and deposited layers. The balance between erosion and deposition processes depends strongly on plasma parameters. It was demonstrated in this work that the erosion-deposition balance can be shifted towards erosion, which is beneficial in the sense that there is no unpredictable layer growth and therefore no undesired change in the reflectivity. The approach used for that was the injection of gaseous impurities in the vicinity of a surface. Such an approach has a two-fold effect: the flux of particle being deposited can be reduced, and the chemical erosion of already deposited species can be intensified.

Chapter 8. Extrapolation to ITER

The reflectivity of first mirrors represents a crucial parameter for reliable performance of respective diagnostics systems and future reactor devices, thus representing a critical aspect in the design of such systems, especially for ITER. Once a diagnostic system in ITER will be installed, it will not be possible to repair or exchange individual mirrors. Therefore, all measures to prevent uncontrolled degradation of the mirror reflectivity have to be implemented to ensure sufficiently long life time of mirrors and thus regular functioning of diagnostic systems.

The main goal to be achieved with respect to first diagnostic mirrors for ITER or any future reactor device is to preserve the optical characteristics of mirrors over the entire envisaged operation period of the device. On the way to achieving this goal for mirrors placed in deposition-dominated conditions, the application of deposition suppression techniques in combination with erosive plasma cleaning of deposited layers and implanted impurities should be considered.

In this work the capability of gas fuelling in the vicinity of first mirrors to mitigate deposition of impurities on the mirror surface was assessed. A significant deposition suppression was achieved with a non-reactive gas fuelling. Using fueling by chemically reactive deuterium, the complete deposition supression and even cleaning of initially pre-deposited a-C:D layer from the mirror surface was achieved due to enhancement of chemical erosion of carbon.

It is planned that ITER will start operation with the initial material mix of Be for the main wall and W for the divertor. Erosion of Be from the main chamber and its deposition elsewhere in the device are expected. Be can be eroded by deuterium chemically via formation of BeD/BeD_2 molecules [Bjorkas 2012], therefore injection of the D_2 gas could be in principle used to clean the mirrors from Be deposits, however the effectiveness of chemical erosion of Be by D atoms and ions still has to be accessed. Feeding of non-reactive gases also could be applied to increase the neutral density in front of the mirror and thus prevent impurity ions from reaching the mirror surface (as it was shown in experiments and modeling described in sections 5.2.3 and 6.1.2). These measures could be applied in the divertor region where the strongest deposition is expected under the dome region and in the vicinity of gas injection modules for the radiative cooling of plasma [Maruyama 2010]. However, as it was already mentioned in section 7.2, the effectiveness of the gas feeding technique with respect to mitigation of deposition of high-Z impurities such as tungsten still has to be demonstrated, and the knowledge about the long-range transport of W in fusion devices has to be extended [Litnovsky 2013a].

To allow and maintain the optimal mirror operation in ITER, multiple strategies to protect first mirrors from incident impurity fluxes and to limit the deposition have to be applied, including the following:

1. Use of shutters open only during measurements [Krasikov 2011];
2. Application of gas puffing in the vicinity of mirrors [Litnovsky 2011b, this work];
3. Special design and geometry of diagnostic ducts to minimize particle fluxes to the mirrors [Brooks 2008] (Figure 8.1), including shaping of diagnostic ducts to provide “traps” for incoming particles and thus reduce the amount of impurities impinging on the mirror surface [Akyiama 2012, Kotov 2011a, Litnovsky 2009];
4. *In-situ* mirror cleaning.

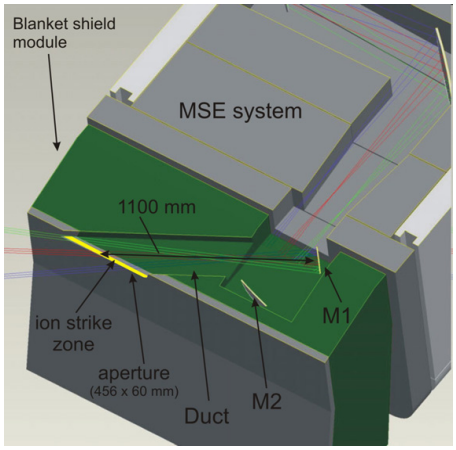

Figure 8.1. a) Motional Stark Effect (MSE) diagnostic geometry at ITER outer midplane first wall location. Optical path shown through blanket shield module (BSM) duct with first 2 mirrors (M1, M2) [Brooks 2008].

Application of protective techniques, such as shutters, will decrease particle fluences to the mirrors and therefore can prolong the mirror lifetime by orders of magnitude [Costley 2001, Brooks 2008, Kotov 2011 b]. Similarly, the geometry of diagnostic ducts can have a significant effect. Recent experiments [Akiyama 2012] and modeling [Kotov 2011a] demonstrate promising results of use of diagnostic ducts equipped with a set of diaphragms (fins). For certain geometries of diagnostic ducts, installation of fins leads to a manifold reduction of the particle flux to the mirror surface. The multi-machine experiments on the confirmation of the effect of fins are ongoing.

It has to be noted that protective techniques such as shutters and fins will be ineffective in the cases of thermo-oxidative or another reactive gas wall conditioning or air leaks, which all can drastically reduce the mirror reflectivity, as was shown in sections 5.3.3 and 6.4.1.2. For this reason, in part, the majority of first diagnostic mirrors in ITER should be equipped with *in-situ* mirror cleaning possibilities. It was demonstrated experimentally that non-destructive techniques used for mirror cleaning from deposited layers have only limited efficiency, and therefore destructive techniques such as sputtering have to be applied. Plasma sputtering is one of the promising techniques demonstrating very high efficiency of removal of deposited layers. Such *in-situ* mirror cleaning systems can be also activated against oxidized surface layers. Not only the deposits but also a thin underlying layer of the mirror surface affected by implantation, diffusion of impurities and chemical transformations can be effectively removed [Litnovsky 2011a]. An example of cleaning of an oxidized SC Mo mirror in a glow discharge in hydrogen is shown in Figure 8.2 [Litnovsky 2007b]. Two exposures 15 minutes each were sufficient to remove the oxide and to restore the mirror reflectivity. Another example of the cleaning of a Mo mirror surface from the oxidized layer is the pre-cleaning of the large SC Mo mirror before the exposure in TEXTOR described in section 5.1.3.3. The mirror reflectivity was below the reference value before cleaning in Argon (Ar) plasma, and the specular reflectivity was restored after 20 min of plasma treatment (Figure 5.21).

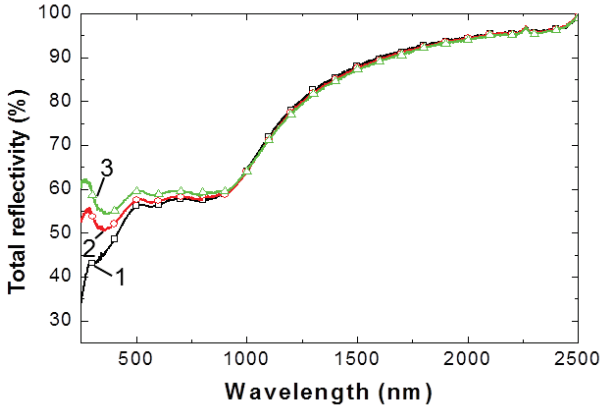

Figure 8.2. Evolution of the total reflectivity of a SC Mo mirror before and after repetitive cleaning procedures in H-glow discharge (1) – before cleaning, (2) – after 1st cleaning, (3) – after 2nd cleaning = clean mirror [Litnovsky 2007b].

To preserve the optical characteristics of mirrors placed in erosion-dominated conditions the proper material choice is important. Damage of the surface under erosion conditions depends on the accumulated particle fluence, mirror temperature, surface composition, crystal structure and mirror material itself. The experimental results obtained in this work (section 5.1) were extrapolated to ITER conditions based on predictive modelling reported in [Kotov 2011b]. The rates and time scales of erosion of first mirrors in the main chamber of ITER were estimated. In [Kotov 2011b], the fluxes of incident D (T) atoms were calculated using the kinetic Monte-Carlo transport code EIRENE [Reiter 2005]. Plasma parameters in the SOL were taken from B2-EIRENE (SOLPS4.3) simulations corresponding to the flat-top phase of a full-power ITER discharge (reference configuration F57) [Kukushkin 2009]. Core plasma was included into the model to simulate fast atoms (~1 keV), which may cause sputtering of mirror materials. Only steady-state plasma was considered.

The results of the predictive modelling from [Kotov 2011b] were compared with the amounts of the sputtered material in the cases of the low-fluence and high-fluence exposures described in this work. The results of the modelling indicate that the amount of the sputtered material for the Mo-coated mirror used for the low-fluence exposure in TEXTOR corresponds to that of a Mo mirror placed at the first wall position in an equatorial port of ITER for 15 discharges of 400 s or in an upper port not equipped with a gas fuelling system for 32 such discharges (see Table 8.1). However, it is foreseen that the first mirrors will be installed not at the first wall position but in ports farther away from plasma. For the ratio of the mirror recession from the first wall position (L) to the diameter (D) of the respective diagnostic duct L / D = 10, the same amount of the sputtered material as observed after the low-fluence exposure in TEXTOR will be reached after about 2500 for an equatorial port and 1700 for an upper port ITER discharges. In the case of the high-fluence exposure in TEXTOR, the accumulated eroding fluences correspond to those that will arrive to a mirror placed at the first wall position in ITER for 47 discharges for an equatorial port and for 101 discharges for an upper port. For mirrors installed in port plugs with a recession L / D = 10, the number of respective discharges increases to about 7800 and 5200.

The results summarized in Table 8.1 are based on the experiments described in this work and suggest that for the envisaged mirror operation time in ITER, SC Mo mirrors will preserve their optical properties, while the Mo-coated mirrors may experience degradation of the

reflectivity in the UV range as follows from the results of the high-fluence exposure (Figure 5.14).

Table 8.1. Extrapolation of experimental results to ITER conditions for mirrors installed in equatorial and upper ports at the first wall position and inside cylindrical diagnostic ducts with different aspect ratios of the duct length L to diameter D (predictive modelling with EIRENE/SOLPS). The number of 400 s long ITER discharges corresponding to the same amount of eroded material as observed in the TEXTOR experiments is given.

		Number of 400 s long ITER discharges			
		First wall position	L / D = 5	L / D = 10	L / D = 20
Low-fluence experiment 40 nm Mo eroded	Equatorial port	15	890	2480	8360
	Upper port without gas fuelling system	32	630	1660	13630
High-fluence experiment 125 nm Mo eroded	Equatorial port	47	2770	7760	26110
	Upper port without gas fuelling system	101	1970	5190	42580

However, the concept of Mo-coated mirrors has a potential as an alternative large-size mirror solution for ITER for diagnostics in the VIS and IR wavelength ranges. The Rh-coated mirrors revealed a drastic drop of the reflectivity in the UV range and their application under erosion conditions in ITER cannot be approved.

As was already mentioned, even mirrors installed in deposition-dominated zones have to be produced from erosion-resistive materials since the most promising technique for cleaning of such mirrors is plasma sputtering. This implies that the selected first mirror materials have to be resistant to erosion in the sense that their reflectivity should not degrade when surface sputtering happens during plasma operation or during cleaning from deposited layers. In contrast to surface deposits, which can be removed, the development of a surface relief, i.e. roughening of the surface, due to inhomogeneous sputtering is not possible to compensate to make the surface smooth again.

Generally, SC Mo mirrors are preferable under erosion-dominated conditions. However, the largest SC Mo mirrors available to date have a diameter of only 10 - 14 cm [Litnovsky 2009]. Therefore, efforts have to be made to increase the mirror size, and a corresponding technology is yet to be developed. At the same time, large Mo-coated mirrors manufactured at industrial level have to be tested under erosion conditions.

To recapitulate, the measures to be applied for mirror protection must include the proper material choice and application of techniques for deposition mitigation, *in-situ* mirror cleaning and *in-situ* mirror calibration.

8.1 Outlook

The studies presented in the thesis as well as investigations performed over the past few years by other researchers provided a better understanding of the evolution of optical properties of mirrors in a plasma environment. Still there is a lot of work to be done before the final solution for first diagnostic mirrors in a fusion reactor could be provided. The main topics that have to be further addressed are the feasibility of deposition mitigation techniques and the *in-situ* application of sputter-cleaning methods.

One of important steps on the way to prevent deposition of impurities on the mirror surface is minimization of fluxes of particles towards first mirrors. This may be done either by optimization of the diagnostic duct geometry [Akiyama 2012, Kotov 2011 a] or by a complete shielding of mirrors by special shutter systems open only during measurements [Walker 2004]. The equipment of diagnostic ducts with a diaphragm-like structure using fins as described in [Akiyama 2012] can significantly reduce deposition rates on the mirror surface.. In order to optimize the shape and geometrical parameters of such diagnostic ducts, further multi-machine studies of deposition in hidden areas are required, in particular addressing different lines of sight and locations within the vacuum vessel. The applicability of shutters can prevent deposition on mirrors during wall conditioning discharges; however, during the main plasma operation when diagnostics need to be operational shutters remain open and have no effect. Therefore, it is essential to identify the phases leading to the major deposition depending on the scenario of operation and the location of diagnostics in order to choose a proper deposition mitigation technique.

Gas feeding near the mirror surface represents another important concept for deposition mitigation. The results obtained during this PhD work illustrate that an essential reduction of impurity deposition and even complete deposition mitigation on the mirror surface can be achieved. However, the method should be further evaluated by engineers in terms of permissible gas injection rates and the overall design of the diagnostic duct. In particular, the amount of injected gas should not affect the machine fuelling.

It was shown in this thesis that a proper choice of the mirror material is important for mirrors subjected to erosion conditions. In addition, layers of chemical phases formed within the ion implantation zone and thus decreasing the mirror reflectivity will have to be removed by *in-situ* cleaning methods. In the opposite case of net-deposition, a certain level of deposition is likely to happen on the mirrors in many cases, despite the application of deposition mitigation techniques. Thus the necessity of sputter-cleaning of such mirrors makes the erosion strength of mirror materials important also for mirrors placed under net-deposition conditions. Studies of RF and ECRH plasma cleaning methods, in particular for mirrors coated with aluminium oxide as proxy for oxidized Be layers [Litnovsky 2013b], demonstrate certain difficulties and ask for further investigations. In particular the applicability of these methods to cleaning of reactor relevant mixed surface layers has to be assessed. The exact cleaning procedure is still to be identified, and this requires better understanding of physical processes involved.

8.2 Conclusions

The concise conclusions are the following:

- Deposition of impurity layers affects the mirror reflectivity, which shows a strong dependence on the deposited layer thickness, which usually cannot be assessed *in-situ*.
- For reliability of diagnostic signals, the mirror reflectivity should be preserved. That is not possible in deposition-dominated zone, therefore mirrors have to be installed under net erosion conditions or such conditions have to be created artificially.
- Single-crystalline materials, for example SC Mo, are the best candidates for mirrors under erosion.
- Particle implantation and surface chemistry take place even for SC mirrors placed under erosion conditions. Material mixing and chemical phase formation can lead to reflectivity changes, which are hard to predict. To remove mixed layers and restore the reflectivity, *in-situ* mirror cleaning should be applied.
- Further dedicated experiments with respect to
    - selected mirror materials,
    - expected mirror surface temperatures,
    - expected impurity species,
    - predicted fluences for different mirror locations

are of extreme importance as they are essential for assessment of the mirror performance under future reactor condition.

Acknowledgements

I would like to thank my colleagues, my friends and my family for their support during the last five years of research, writing the thesis and very interesting experiment of being a parent.

First of all, I would like to thank Prof. Dr. U. Samm for giving me the opportunity to carry out this research and to work in the outstanding research environment, as well as for being the doctoral advisor of my thesis. Thank you very much for your opinion and discussions.

I would like to extend my thank you to Prof. Dr. Willi who kindly agreed to be the second thesis examiner.

My special thank you goes to Prof. Dr. Ch. Linsmeier who helped me to consolidate and improve the structure of the thesis and provided invaluable support in the last stage of my work with his advices and long-term expertise in XPS data evaluation.

I would like to express my sincere gratitude to my scientific adviser Dr. Andrey Litnovsky who guided me through the complex process of the PhD research. Thank you for your patience and advice, for enthusiasm for science and research, for always being ready to help, share your knowledge and discuss experiments and results, and for all the support and care, which is hard to overestimate.

While working mostly as experimentalist, I appreciate the support of Andreas Kirschner, Klaus Schmidt, Dmitry Borodin and Dmitry Matveev with computer codes, which was very helpful. Thank you for your patience.

I would like to thank everyone I worked with during the past few years: Henning Stoschus for the data from the supersonic helium beam diagnostics, Andriy Romanyik for the introduction to material characterization, Till Höschen for XPS measurements, Uwe Breuer for SIMS measurements and fruitful discussions, Martin Köppen for incredible patience, support and help with XPS data analysis, Laurent Marot and Baran Eren for mirror samples and XPS measurements, Christian Schulz and Sören Möller for the pre-treatment of mirrors in the PADOS facility, Harry Reimer for his great photos, Jury Krasikov for extraordinary mirror fixation system. A special thank you goes to Peter Wienhold for fruitful discussions and his inexhaustible enthusiasm. In addition I'd like to thank the whole technical staff and the TEXTOR Team for their efforts and participation in the experiments. Without your contribution the work could not be done. Thank you very much!

I owe my thank you to all the colleagues at IEK-4 for the pleasant atmosphere, help and support during my work. A great thank you goes to all diploma and master students, and doctoral and post-doctoral fellows at the institute with whom I was chatting, drinking tea and laughing day after day. It is very important for me that I found here such nice friends as you, Jan, Henning, Nadine, Maren, Luxherta, Miro, Niels, Christian, Marko, Ruth, Sören, Martin. By the way, Maren and Martin, thank you very much for translating the abstract into German!

I would also like to thank my Russian-Ukrainian-Belarussian friends whom I met in Jülich. Thank you very much for the very pleasant and cheerful atmosphere, mutual understanding, feeling of home and lots of fun together!

I express my deepest gratitude to my parents and parents-in-law who supported me a lot during all this time. Thank you for your help, love and trust, for believing in me more than myself. Thousands of thank you I want to say to my husband Dmitry who supported me with everything: housework, baby-sitting and all other tasks, giving me a possibility to write one more page, one more chapter… And for the nights he spent reading this thesis and making remarks as the first and very strict reader. Thank you very much for all the possible support, love and care!

And, of course, I thank my son, my little man, for everyday discoveries, unexpected tasks, happiness and inspiration, and for our smiles in response to his smile, without which I cannot imagine our life.

Bibliography

[Akiyama 2012] T. Akiyama et al, *Studies of reflectivity degradation of retroreflectors in LHD and mitigation of impurity deposition using shaped diagnostic ducts and protective windows*, Nucl. Fusion 52 (2012) 063014

[Alimov 2008] V.Kh. Alimov et al., *Surface modifications and deuterium depth profiles in molybdenum irradiated with low-energy D ions*, J. of Nucl. Mater 381 (2008) 267–270

[Allen 2010] S. L. Allen et al., *Particle Control and Transport Experiments in the DIII-D Tokamak with Graphite Walls*, Proc. 23rd Fusion Energy Conference, Daejeon, Korea, October 11–16, 2010, International Atomic Energy Agency (2010)

[BAPD] Binary Alloy Phase Diagrams, Software from ASM International, The Materials Information Society

[Baranova 1968] V.I. Baranova, S.A. Golovin, M.A. Krtishtal, M.I.Lerner, Phisics and Chemisrtryof Materials Treatment, (in russian), 1968, No2, pp. 61-65

[Bardamid 2002] A. F. Bardamid et al., *Behaviour of Mo mirrors under bombardment by ions of deuterium plasma*, 15th international conference on physics of radiation effects and radiation materials, Alushta, June 2002.

[Behrisch 2003] R. Behrisch et al., *Material erosion at the vessel walls of future fusion devices*, Journal of Nuclear Materials 313–316 (2003) 388–392

[Belyansky 1994] M. Belyansky, M. Trenary and C. Ellison, *Boron Chemical Shifts in B_6O*, Surf. Sci. Spectra 3, 147 (1994)

[Benenson 2002] W. Benenson, J. W. Harris, H. Stocker, h. Lutz, *Handbook of physics,* 2002 Springer-Verlag New York, Inc. ISBN 0-387-95269-1

[Bennett 1961] H.E. Bennett, J.O. Porteus *Relation between Surface Roughness and Specular Reflectance at Normal Incidence*, J. Opt. Soc. Am.–1961.–V.51.–№2.–P.123-129

[Bennett 1999] J. M. Bennett and L. Mattsson, *Introduction to Surface Roughness and Scattering,* Second Edition (Optical Society of America, Washington, D.C., 1999)

[Biel 2011] W. Biel et al., *Overview on R&D and design activities for the ITER core charge exchange spectroscopy diagnostic system*, Fusion Engineering and Design 86 (2011) 548–551

[Bjorkas 2009] C. Bjorkas et al., *Chemical sputtering of Be due to D bombardment*, New J. of Physics 11 (2009) 123017

[Bjorkas 2012] C. Bjorkas et al., *Multiscale modeling of BeD release and transport in PISCES-B*, J. Nucl. Mater. 438 (2013) S276

[Bohdansky 1984] J. Bohdansky, *A universal relation for the sputtering yield of monatomic solids at normal ion incidence*, Nucl. Instr. and Meth. in Phys. Res. B2 (1984) 587-591

[Born&Wolf] M. Born and E. Wolf, *Principles of Optics: Electromagnetic theory of propagation, interference and diffraction of light*, 6th edition, reprinted with corrections, Oxford: Pergamon Press, 1986, ISBN: 9780080264820

[Borodin 2013] D. Borodin et al., *Determination of Be sputtering yields from spectroscopic observations at the JET ILW based on 3D ERO modelling*, 14th International Conference on Plasma-Facing Materials and Components for Fusion Applications, May 13-17, 2013, Forschungszentrum Juelich, Germany

[Brewer 1980] L Brewer, R.H. Lamoreaux, A. Ferro. *Molybdenum: Physico-Chemical Properties of its Compounds and Alloys*, Atomic Energy Review.Special lssue No. 7., Vienna, International Atomic Energy Agency (1980) 309

[Brooks 2008] J.N. Brooks and J.P. Allain, *Particle deposition and optical response of ITER motional Stark effect diagnostic first mirrors*, Nucl. Fusion 48 (2008) 045003

[Burylev 1969] B. P. Burylev, *Диаграммы состояния систем родия и иридия с углеродом*, Известия высших учебных заведений, цветная металлургия (Nonferrous metallurgy transaction. News of higher schools) 5 (1969)

[Costley 2001] A.E. Costley, D.J. Campbell, S. Kasai, K.E. Young, and V. Zaveriaev, *ITER R&D: Auxiliary Systems: Plasma Diagnostics*, Fus. Eng. Des. 55 (2001) 331-346

[Davis 2009] J. W. Davis and A. A. Haasz, *Oxidation of carbon deposits as a fuel removal technique for application in fusion devices*, Journal of Nuclear Materials 390–391 (2009) 532–537

[Davis 2011] J. W. Davis et al., *Thermo-Oxidation of DIII-D Codeposits on Open Surfaces and in Simulated Tile Gaps*, J. Nucl. Mater., 415, S789 (2011)

[De Temmerman 2005] G. De Temmerman et al., *Study of optical properties of Mo_xC_{1-x} films*, J. Nucl. Mat. 337–339 (2005) 956–959

[De Temmerman 2006] G. De Temmerman, *On the lifetime of the First Mirrors in the diagnostic systems of the International Thermonuclear ExperimentalReactor*, PhD thesis, Basel University (2006)

[De Temmerman 2007] G. De Temmerman et al., *Beryllium deposition on International Thermonuclear Experimental Reactor first mirrors: Layer morphology and influence on mirror reflectivity*, J. Appl. Phys. 102, 083302 (2007)

[Ding 2010] R. Ding et al., *Modelling of local carbon deposition from methane and ethane injection through graphite and tungsten test*

limiters in TEXTOR, Plasma Phys. Control. Fusion 52 (2010) 045005

[Doerner 2009] R. Doerner et al., *The role of beryllium deuteride in plasma-beryllium interactions*, J. of Nucl. Mater. 390-391 (2009) 681-684

[Donne 2002] A.J.H. Donne et al*, Physics R&D in Support of ITER/BPX Diagnostic Development*, Proc. of the 19th IAEA Fusion Energy Conference, Lyon, France, paper CT/P-10 (2002)

[Droste 2008] S. Droste et al., *Modelling of $^{13}CH_4$ injection experiments with graphite and tungsten test limiters in TEXTOR using the coupled code ERO-SDTrimSP*, Plasma Phys. Control. Fusion 50 (2008) 015006

[Eckstein 1991] W. Eckstein, *Computer simulation of ion-solid interaction*, Springer Series in Material Science, Vol. 10, Springer, 1991.

[Eckstein 1993] W. Eckstein et al., *Sputtering Data,* Tech. Report IPP MPI, IPP 9/82 (1993)

[Eckstein 2002] Eckstein, W., *Calculated Sputtering, Reflection and Range Values*, Report IPP 9/132, Max-Planck-Institut für Plasmaphysik (2002)

[Eckstein 2003] W. Eckstein and R. Preuss: *New fit formulae for the sputtering yield*, J. of Nucl. Mater. 320 (2003) 209 – 213

[Eckstein 2007] W. Eckstein, R. Dohmen, A. Mutzke and R. Schneider, *SDTrimSP: A Monte-Carlo Code for Calculating Collision Phenomena in Randomized Targets*, Report IPP 12/3, Max-Planck-Institut für Plasmaphysik (2007), URL: http://edoc.mpg.de/display.epl?mode=doc&id=287291&col=33&grp=1311#cb

[Eckstein 2011] W. Eckstein, *Sputtered Energy Coefficient and Sputtering Yield*, IPP report 17/29, Dezember 2011

[Elyutin 71] V. P. Elyutin, T. G. Lenskaya, Yu. A. Pavlov, V. P. Polyakov, *Определение коэффициентов диффузии кислорода в окислах металлов методом ЭДС*, Dokl. Akad. Nauk SSSR, (in russian), 199 (1971) 62-65

[EPMA-Aachen] Central Facility for Electron Microscopy (Gemeinschaftslabor für Elektronenmikroskopie - GfE) at RWTH-Aachen, URL: http://www.gfe.rwth-aachen.de/seiteninhalte/untersuchung_esma.htm

[Eren 2011] B. Eren et al, B. Eren et al, *Reflective metallic coatings for first mirrors on ITER*, Fusion Engineering and Design 86 (2011) 2593–2596

[Eren 2011] B. Eren et al., *The effect of low temperature deuterium plasma on molybdenum reflectivity*, Nucl. Fusion 51 (2011) 103025

[Eren 2013] B. Eren et al., *Roughening and reflection performance of molybdenum coatings exposed to a high-flux deuterium plasma*, Nucl. Fusion 53 (2013) 113013

[Fitzpatrick 2010] B. W. N. Fitzpatrick et al., *Assessment of Collateral Effects of Thermo-Oxidation on DIII-D In-Vessel Components in Preparation for In Situ Oxidation in DIII-D*, Fusion Sci. Technol. 58 (2010) 603

[Freeman 1974] R. L. Freeman and E. M. Jones, *Atomic Collision Processes in Plasma Physics Experiments: I*, UKAEA rep. No. CLM-R 137, Culham Laboratory, Abingdon, England 1974

[Frese 1987] K. W. Frese, *Calculation of surface binding energy for hydrogen, oxygen and carbon atoms on metallic surfaces*, Surface Science 182 (1987) 85-97, North-Holland, Amsterdam

[Fujiwara 2007] H. Fujiwara, *Spectroscopic ellipsometry: principles and applications*, (2007) John Wiley and Sons, Ltd.

[Gall 2002] N.R. Gall, E.V. Rutkov, A.Ya. Tontegode *Carbon diffusion between volume and surface (100) of Mo*, J. Tech. Phys. (2002) 72-4

[Gil 2007] C. Gil et al., *Retro-reflected channels of the Tore Supra FIR interfero-polarimeter for long pulse plasma operation*, Fusion Engineering and Design 82 (2007) 1238–1244

[Grimes 2004] J. Grimes et al., *Optical characterization of polished Mo2C foil*, Annual APS Meeting, March 3-7, 2003; Austin Convention Center; Austin, TX, URL: http://flux.aps.org/meetings/YR03/MAR03/baps/abs/S2550015.html (data from private communication)

[Gurler 1991] R. Gurler, J.N. Pratt; *Some constitutional studies on the molybdenum-rhodium system*, J. Alloys & Compounds 177 (1991) 321-330

[Guzmán 2013] F. Guzmán, former ADAS-EU Research Fellow, private communications

[Haasz 1996] A. A. Haasz et al., *Thermo-Oxidative Erosion of Amorphous Hydrogenated Carbon Films*, J. Vac. Sci. Technol., A, 14, 184 (1996)

[Haasz 1998] A. A. Haasz et al., *Atomic and Plasma-Material Interaction Data for Fusion*, Volume 7A, IAEA, Vienna (1998)

[Haasz 2007] A.A. Haasz et al., *Thermo-Oxidation of Codeposits from DIII-D Divertor Tiles*, Phys. Scr., T128, 55 (2007)

[Heitjans 2005] P. Heitjans, J. Kärger, *Diffusion in condensed matter*: *Methods, Materials, Models*, Springer 2005

[Heumann 1992] Th. Heumann, *Diffusion in Metallen*, 1992, p. 234

[Hollas 2010] J. M. Hollas, *Modern Spectroscopy*, fourth edition, (2010) John Wiley and Sons, Ltd, ISBN 13: 978-0-470-84416-8 (P/B)

[Hoshihira 2009] T. Hoshihira et al., *A study of hydrogen blistering mechanism for Molybdenum by Tritium radio-luminography*, Journal of Nuclear Materials 390–391 (2009) 1029–1031

[Hu 2006] J. S. Hu et al., *Thermo-Oxidation to Remove Re-Deposited Layers and to Release Trapped Hydrogen Isotopes in HT-7 Superconducting Tokamak*, J. Nucl. Mater., 349, 160 (2006)

[Huber 2000] A. Huber et al., *Spectroscopic measurements of the ion temperature profile in front of a limiter in TEXTOR-94*, Plasma Phys. Control. Fusion 42 (2000) 569-578

[IAEA 1958] L. A. Artsimovich, *Research on controlled thermonuclear reactions in the USSR*, Proc. United Nations Second Conference on the Peaceful Uses of Atomic Energy, Session 4 P/2298, September 1958

[ITER 1999] *ITER physics basis*, Nucl. Fusion, 39/12 (1999) 2541

[ITER ITA 2006] ITER ITA Newsletter No.27, January 2006, IAEA, ISSN 1727-9852

[ITER] ITER project home page, URL: http://www.iter.org

[Kny 1988] E.Kny, J. Winter, U.Littmark, *Thermal shock and thermal cycling behaviour of amorphous a-C:H films on Mo substrates*, J. Nucl. Mater. 155-157 (1988) 273-277

[Konovalov 2001] V.G. Konovalov et al., *On the problem of material for the in-vessel mirrors of plasma diagnostics in a fusion reactor*, Fusion Engineering and Design 56–57 (2001) 923–927

[Konovalov 2012] V. G. Konovalov et al., *Specular and diffusive reflectance of stainless steel mirrors sputtered with Ar^+ ions*, VANT 6 (2012) 82

[Kotov 2011 a] V Kotov et al, *Passive protection of the ITER diagnostic mirrors*, Phys. Scr. T145 (2011) 014071

[Kotov 2011 b] V. Kotov et al., *Numerical estimates of the ITER first mirrors degradation due to atomic fluxes*, Fusion Engineering and Design 86 (2011) 1583–1586

[Krasikov 2011] Yu. Krasikov et al., *Development of design options for the port plug components of the ITER core CXRS diagnostic*, Fusion Engineering and Design 86 (2011) 2055–2059

[Krasikov 2012] Yu. Krasikov et al., *First Mirror Design Options for the ITER core CXRS diagnostisc,* at 27th Symposium on Fusion Technology (SOFT-27), September 24-28, 2012, Liege, Belgium

[Kruezi 2012] U. Kruezi, *Supersonic helium beam diagnostic for fluctuation measurements of electron temperature and density at the Tokamak TEXTOR*, Rev. Sci. Instrum. 83, 065107 (2012)

[Kuestner 1998] M. Kuestner et al., *The inluence of surface roughness on the angular dependence of the sputter yield,* Nucl. Instr. and Meth. in Phys. Res. B 145 (1998) 320-331

[Kukushkin 2009] A. S. Kukushkin, H. D. Pacher et al., *Analysis of performance of the optimized divertor in ITER*, Nuclear Fusion 49 (2009) 075008

[Laengner 2009] M. Laengner, *Untersuchung zur Wiederherstellung der optischen Eigenschaften diagnostischer Spiegel durch Elektron-Zyklotron-Resonanz geheizte Plasmen für zukünftige Fusionsreaktoren*, Diploma work, Bonn University (2009)

[Landolt-Boernstein] Landolt-Boernstein, *Numerical Data and Functional Relationships in Science and Technology*, New Series, Group III: *Crystal and Solid State Physics*, Vol. 26, *Diffusion in Metals and Alloys*, Springer-Verlag, Berlin, 1990, DOI: 10.1002/bbpc.19930970725

[Lipa 2006] M. Lipa et al., *Analyses of metallic first mirror samples after long term plasma exposure in Tore Supra*, Fusion Engineering and Design 81 (2006) 221–225

[Litnovsky 2005] A. Litnovsky et al., *Direct comparative test of single crystal and polycrystalline diagnostic mirrors exposed in TEXTOR in erosion conditions*, presented by G. De Temmerman at 32nd EPS Conference on Plasma Phys., Tarragona, 27 June - 1 July 2005, ECA Vol.29C, P-4.099 (2005), URL: http://epsppd.epfl.ch/Tarragona/pdf/P4_099.pdf

[Litnovsky 2007a] A. Litnovsky et al., *Diagnostic mirrors for ITER: A material choice and the impact of erosion and deposition on their performance*, Journal of Nuclear Materials 363–365 (2007) 1395–1402

[Litnovsky 2007b] A. Litnovsky et al., *Investigations of single crystal and polycrystalline metal mirrors under erosion conditions in TEXTOR*, Fusion Engineering and Design 82 (2007) 123–132

[Litnovsky 2008] A. Litnovsky et al., *First tests of diagnostic mirrors in a tokamak divertor: An overview of experiments in DIII-D*, Fusion Engineering and Design 83 (2008) 79–89

[Litnovsky 2009] A. Litnovsky et al., *Progress in research and development of mirrors for ITER diagnostics*, Nucl. Fusion 49 (2009) 075014

[Litnovsky 2011a] A. Litnovsky et al., *Development of in situ cleaning techniques for diagnostic mirrors in ITER*, Fusion Engineering and Design 86 (2011) 1780–1783

[Litnovsky 2011b] A. Litnovsky et al., *Active control over carbon deposition on diagnostic components and in remote areas of ITER*, Journal of Nuclear Materials 417 (2011) 830–833

[Litnovsky 2012] Litnovsky et al., *Impact of Thermo-Oxidative Wall Conditioning on the Performance of Diagnostic Mirrors for ITER*, Fusion Science and Technology, vol. 62, July-Aug. 2012

[Litnovsky 2013a] A. Litnovsky, M. Matveeva et al., *First studies of ITER diagnostic mirrors in a tokamak with all-metal interior: results of the first mirror test in ASDEX Upgrade*, Nucl. Fusion 53 (2013) 073033

[Litnovsky 2013b] A. Litnovsky, L. Buzi, Final report on Service Contract *"Development and Validation of Be-Cleaning Techniques for*

ITER Diagnostic First Mirrors Using Be-Proxies", contract number – ITER/CT/12/4300000546

[Luthin 2001] J. Luthin and Ch. Linsmeier, *Influence of oxygen on the carbide formation on tungsten*, J. Nucl. Mater. 290-293 (2001) 121-125

[Luxon 2002] J. L. Luxon, *A Design Retrospective of the DIII-D Tokamak*, Nucl. Fusion 42 (2002) 614

[Manhard 2013] A. Manhard, G. Matern and M. Balden, *A step-by-step analysis of the polishing process for tungsten specimens*, Practical Metallography 2013/01, Page 5-16

[Marchuk 2007] O. Marchuk, M. Z. Tokar, *Modeling of supersonic plasma flow in the scrape-off layer*, J. Comp. Phys. **227** (2007) 1597-1607

[Marot 2007] L. Marot et al., *Rhodium coated mirrors deposited by magnetron sputtering for fusion applications*, Rev. Sci. Instrum. 78 (2007) 103507.

[Marot 2008] L. Marot et al., *Characterization of magnetron sputtered rhodium films for reflective coatings*, Surf. Coat. Tech. 202 (2008) 2837

[Marot 2013] L. Marot et al., *Synergistic effects of hydrogen plasma exposure, pulsed laser heating and temperature on rhodium surfaces*, J. of Nucl. Mater. 432 (2013) 388–394

[Maruyama 2010] S. Maruyama et al., *ITER Fuelling System Design and Challenges. Gas and Pellet Injection and Disruption Mitigation*, 23rd IAEA Fusion Energy Conference, Daejon, Republic of Korea, 11-16 October 2010, contributed paper ITR/P1-28, URL: http://www-pub.iaea.org/mtcd/meetings/PDFplus/2010/cn180/cn180_papers/itr_p1-28.pdf

[Matsunami 1984] N. Matsunami et al., *Energy dependence of the ion-induced sputtering yields of monatomic solids*, Atomic data and nuclear data tables 31, l-80 (1984)

[Matveeva 2008] M. Matveeva, *Investigation of the capability of ECRH discharge to clean the mirrors of ITER diagnostics*, Master's thesis, Ghent University (2008)

[Matveeva 2011] M. Matveeva et al., *Active control over carbon deposition by gas feeding for protection of diagnostic mirrors in ITER*, Phys. Scr. T145 (2011) 014072

[Miyamoto 2005] K. Miyamoto, *Plasma Physics and Controlled Nuclear Fusion*, Springer (2005) ISBN 3-540-24217-1

[MTDATA] MTDATA – Phase Diagram Software from the National Physical Laboratory, URL: http://resource.npl.co.uk/mtdata/phdiagrams/crh.htm

[Mukhin 2009] E. Mukhin et al, *Progress in the development of deposition prevention and cleaning techniques of in-vessel optics in ITER*, Nucl. Fusion 49 (2009) 085032

[Mukhovatov 2003] V. Mukhovatov *et al*., *Overview of physics basis for ITER*, Plasma Phys. Control. Fusion 45 (2003) A235–A252

[Nishijima 09] D. Nishijima et al., *Erosion yields of deposited beryllium layers*, J. of Nucl. Mater. 390-391 (2009) 132-135

[Nordlund 06] K. Nordlund, *Atomistic simulations of plasma-wall interactions in fusion reactors*, Physica Scripta T124 (2006) 53

[Nordlund 11] K. Nordlund et al., *Interatomic Potential for the Be-C-H System and Simulation of BeD Molecule Formation*, Part of IAEA CRP(2007-2011): *Data for Surface Composition Dynamics Relevant to Erosion Processes*

[Ogorodnikova 2009] O.V. Ogorodnikova, *Ion-driven deuterium retention in high-Z metals*, Journal of Nuclear Materials 390–391 (2009) 651–654

[Palik] *Handbook of optical constants of solids*, ed. E.D. Palik, Acad. Press, 1985 and 1991

[Pastewka 2011] L. Pastewka et al., *Anisotropic mechanical amorphization drives wear in diamond*, Nature Materials, vol. 10, January 2011

[Petrova 2009] N. V. Petrova, I. N. Yakovkin, *Binding energies for oxygen on transition metal surfaces*, Surface Review and Letters, Vol. 16, No. 2 (2009) 291–296

[Philipps 1999] V. Philipps et al., *Removal of Redeposited Layers and Hydrogen Release by Oxygen Ventilation of TEXTOR-94*, J. Nucl. Mater., 266–269, 386 (1999)

[Philipps 2003] V. Philipps et al., *Chemical erosion behaviour of carbon materials in fusion devices*, J. Nucl. Mater. 313–316 (2003) 354

[Piel 2010] Piel, A: Plasma physics. *An Introduction to Laboratory, Space, and Fusion Plasmas*, Springer (2010) ISBN 978-3-642-10490-9

[Pisarev 1984] A. A. Pisarev, V.N. Tsyplakov, *Absorption parameters of deuterium ions in molybdenum*, Soviet Atomic Energy Vol. 57, No. 2 (August, 1984), pp. 534-539

[Plansee] Source: Plansee AG;

[Pospieszczyk 1993] A. Pospieszczyk, *Diagnostics of Edge Plasmas by Optical Methods*, Atomic and Plasma-Material Interaction Processes in Control. Thermonucl. Fusion (1993) 213-242

[Reinke 1999] P. Reinke, P. Oelhafen, *Early stages of carbon film growth: carbide interface formation on molybdenum*, Diamond and Related Materials 8 (1999) 155-159

[Reinke 2000] P.Reinke, P. Oelhafen, *The Mo-C interface: formation and electronic structure of the carbide layer*, Surface Sci. 468 (2000) 203-215

[Reiter 2005] D. Reiter, M. Baelmans and P.Boerner, *The EIRENE and B2-EIRENE Codes*, Fus. Sc. Tech 47, 172 (2005) and URL: www.eirene.de

[RF ITER 2005] Summary report of Russian Federation Home Team on R&D in support of ITER diagnostic design: *"Development of first mirrors, perform irradiation tests on candidate optical components and prototype diagnostic elements"*. ITA 55-07. WBS. No. N 55 TD 17 FR, March 2005.

[Roth 1996] J. Roth and C. Garcia-Rosales: *Analytic description of the chemical erosion of graphite by hydrogen ions*, Nuclear Fusion 36 (1996) 1647; Corrigendum: Nuclear Fusion 37-6 (1997) 897

[Roth 1999] J. Roth, *Chemical erosion of carbon-based materials in fusion devices*, J. Nucl. Mater. 266-269 (1999) 51-57

[Roth 2004] J. Roth et al., *Flux dependence of carbon chemical erosion by deuterium ion*, Nucl. Fusion 44 (2004) L21–L25

[Rubel 2009] M. Rubel, *An overview of a comprehensive First Mirror Test for ITER at JET*, Journal of Nuclear Materials 390–391 (2009) 1066–1069

[Rubel 2010] M. Rubel et al., *First Mirrors Test in JET for ITER: An overview of optical performance and surface morphology*, Nuclear Instruments and Methods in Physics Research A 623 (2010) 818–822

[Rut'kov 2011] E. V. Rut'kov, A. V. Kuz'michev, and N. R. Gall', *Carbon Interaction with Rhodium Surface: Adsorption, Dissolution, Segregation, Growth of Graphene Layers*, Physics of Solid State Vol. 53 No. 5 2011

[Ruzic 1990] D.N. Ruzic, *The effects of surface roughness characterized by fractal geometry on sputtering*, Nucl. Instr. and Meth. in Phys. Res B47 (1990) 118-125

[Salanov 1992a] A.N. Salanov and V.I. Savchenko, *Analysis of thermal desorption spectra of oxygen desorbed from phodium*, React. Kinet. Catal. Lett., Vol. 48, No. 2, 357-365 (1992)

[Salanov 1992b] А. Н. Саланов и В. И. Савченко, *О влиянии примесей бора и углерода на взаимодействие кислорода с родием*, Кинетика и Катализ, том 33, вып. 2, 1992

[Samm 2005] U.Samm, *Plasma–Wall Interaction: Status and Data Needs in Nuclear Fusion Research. Understanding Plasma-Surface Interactions*, Springer-Verlag (2005), ISBN 3-540-23038-6

[Schlueter 2008] M. Schlueter et al., *Temperature dependence of the chemical sputtering of amorphous hydrogenated carbon films by hydrogen*, J. of Nucl. Mater. 376 (2008) 33–37

[Schmitz 2008] O.Schmitz et al., *Application of advanced edge diagnostics for transport studies in the stochastic boundary of TEXTOR-DED*, AIP Conf. Proceedings 993 (2008) 135-142

[Schweer 2005] B. Schweer et al., *Limiter Lock Systems at TEXTOR: Flexible Tools for Plasma-Wall Investigation*, Fusion Sci. Technol. 47 (2005) 138

[Semenenko 2008] V.E. Semenenko, N.N. Pilipenko, *Dispersive hardening of alloys Mo-Zr-C*, Quest. of Atom. Sci. and Tech.(2008) 1 (17) 205-210

[Sharpe 2009] J.P. Sharpe et al., *Retention behavior in tungsten and molybdenum exposed to high fluences of deuterium ions in TPE*, Journal of Nuclear Materials 390–391 (2009) 709–712

[Shu 2009] W.M. Shu et al., *Deuterium retention, blistering and local melting at tungsten exposed to high-fluence deuterium plasma*, J. of Nucl. Mater. 390–391 (2009) 1017–1021

[Shunk 1969] F.A. Shunk, H. McGraw; *Constitution of Binary Alloys*; Second Supplement (1969) 648-649.

[Smolik 2000] G. R. Smolik, D. A. Petti, S. T. Schuetz, *Oxidation, volatilization, and redistribution of molybdenum from TZM alloy in air*, Idaho National Engineering and Environmental Laboratory, INEEL/EXT-99-01353, January 2000

[Stangeby 2000] P. C. Stangeby, *The Plasma Boundary of Magnetic Fusion Devices*, Institute of Physics (IoP) Publishing Ltd. (2000) ISBN 0 7503 0559 2, URL: http://stacks.iop.org/0741-3335/43/i=2/a=702

[Sugie 2004] T. Sugie et al., *Irradiation test of Mo- and W-mirrors for ITER by low energy deuterium ions*, Journal of Nuclear Materials 329–333 (2004) 1481–1485

[Sugie 2007] T. Sugie, A. Costley, A. Litnovsky, *Update of the first mirror table*, a presentation at 12th Meeting of the ITPA Topical Group on Diagnostics, 26 – 30 March 2007, PPPL. Princeton USA

[Tanabe 1994] T. Tanabe et al., *High-Z MO-limiter test in TEXTOR. Impurity fluxes, thermal response and post-mortem analysis of Mo-limiter head*, Journal of Nuclear Materials 212-215 (1994) 1370-1375

[Tokunaga 2005] K. Tokunaga et al., *Blister formation and deuterium retention on tungsten exposed to low energy and high flux deuterium plasma*, J. of Nucl. Mater. 337–339 (2005) 887–891

[Tsui 2008] C. K. Tsui et al., *Deuterium Removal During Thermo-Oxidation of Be-Containing Codeposits from JET Divertor Tiles*, Nucl. Fusion, 48, 035009 (2008)

[UN documents] United Nations: *World Population Prospects: The 2008 Revision*, *Volume 1: Comprehensive Tables*, and United Nations: *World Population Prospects: The 2008 Revision, Highlights*, doi:10.1111/j.1728-4457.2010.00368.x

[van der Heide 2012] P. van der Heide, *X-ray Photoelectron Spectroscopy: An introduction to Principles and Practices*, Wiley (2012), ISBN: 978-1-118-06253-1

[Vasil'ev 1982] N. N. Vasil'ev, A. V. Nedospasov, M. Z. Tokar', *Theoretical analyses of a turbulent plasma blanket for a tokamak reactor*, Fiz. Plazmy 37-44 (Jan.- Feb. 1982)

[Vietzke 1987a] E. Vietzke et al., *The reaction of atomic hydrogen with plasma deposited a-C:H films*, in: P. Koidl, P. Oelhafen (Eds.), Amorphous Hydrogenated Carbon Films, E-MRS Symposia Proceedings, vol. XVII, LesE´ ditions de Physique, Les Ulis, 1987, p. 351

[Vietzke 1987b] E. Vietzke, *Chemical erosion of amorphous hydrogenated carbon films by atomic and energetic hydrogen*, Journal of Nuclear Materials 145-147 (1987) 443-447

[Voitsenya 1999] V.S. Voitsenya et al., Some problems of the material choice for the first mirrors of plasma diagnostics in a fusion reactor, Rev. Sci. Instr. 70 (1999) 790–793.

[Voitsenya 2001a] V. Voitsenya et al., *Some problems arising due to plasma-surface interaction for operation of the in-vessel mirrors in a fusion reactor*, J. Nucl. Mater. 290–293 (2001) 336-340

[Voitsenya 2001b] V. Voitsenya et al., *Diagnostic first mirrors for burning plasma experiments*, Rev. Sci. Instrum., Vol. 72, No. 1, January 2001

[Voitsenya 2005] V. S. Voitsenya et al., Effect of exposure inside the Large Helical Device vessel on the optical properties of stainless steel mirrors, Plasma Device Oper. 13 (4) (2005) 291-300

[Voitsenya 2013a] V.S. Voitsenya et al., Effect of sputtering on self-damaged recrystallized W mirror specimens, Journal of Nuclear Materials 434 (2013) 375–381

[Voitsenya 2013b] V.S. Voitsenya et al., Development of surface relief on polycrystalline metals due to sputtering, Nuclear Instruments and Methods in Physics Research B 302 (2013) 32–39

[Vukolov 2004] K. Vukolov et al., *Exposure of stainless steel mirrors in T-10 tokamak*, Plasma Device Oper. 12 (3) (2004) 193

[Wagner 1979] C. D. Wagner, *Handbook of X-ray photoelectron spectroscopy*, Physical Electronics Division, Perkin-Elmer Corp., 1979, DOI: 10.1002/sia.740030412

[Walker 2004] C.I. Walker, et al, *ITER diagnostics: Integration and engineering aspects*, Rev. Sci. Instrum., 75 (2004) 4243.

[Wesson 2004] Wesson, J. A: *Tokamaks*, Clarendon Press, Oxford [u.a.], third edition (2004) ISBN 0-19-850922-7

[Wienhold 1989] P. Wienhold et al., *Determination of the carbon redeposition rate in the scrape-off layer of TEXTOR by a new, time integrated collection technique*, J. Nucl. Mater. 162-164 (1989) 369-375

[Wienhold 2005] P. Wienhold et al., *Exposure of metal mirrors in the scrape-off layer of TEXTOR,* Journal of Nuclear Materials 337–339 (2005) 1116–1120

[William 1971] William et al., *X-ray photoelectron spectroscopy of molybdenum compounds. Use of electron spectroscopy for chemical analysis (ESCA) in quantitative analysis*, Analytical chemistry, VOL. 43, NO. 13, NOVEMBER 1971

[Wong 1998] C. P. C. Wong et al., *Divertor Material Evaluation System (DiMES)*, J. Nucl. Mater., 258–263, 433 (1998)

[Yamamura 1983] Y. Yamamura, Y. Itikawa, and N. Itoh, Report IPPJ-AM-26, Nagoya (1983)

[Yamamura 1996] Y. Yamamura, H. Tawara, *Energe dependence of ion-induced sputtering yields from monatomic solids at normal incidence*, Atomic data and nuclear data tables 62, 149–253 (1996), article No. 0005

[Ying-liang] M. Ying-liang, Chir. Shu Hsueh Pao 7, Nr. 1, 1964, 68/76; UCRL- Trans- 10103

[Ziegler 2006] J. F. Ziegler, *SRIM-2006 computer code*, URL: http://www.srim.org, 2006

Band / Volume 248
Stoffliche Charakterisierung radioaktiver Abfallprodukte durch ein Multi-Element-Analyseverfahren basierend auf der instrumentellen Neutronen-Aktivierungs-Analyse – MEDINA –
A. W. Havenith (2015), 311 pp
ISBN: 978-3-95806-033-3

Band / Volume 249
Quantitative Two-Layer Inversion and Customizable Sensor-Array Instrument for Electromagnetic Induction based Soil Conductivity Estimation
A. T. Mester (2015), viii, 119 pp
ISBN: 978-3-95806-035-7

Band / Volume 250
Partial Neutron Capture Cross Sections of Actinides using Cold Neutron Prompt Gamma Activation Analysis
C. Genreith (2015), vii, 166, XXXII pp
ISBN: 978-3-95806-036-4

Band / Volume 251
Long Term Aerosol Composition Measurements at the CESAR Tower at Cabauw, NL
P. Schlag (2015), iii, 228 pp
ISBN: 978-3-95806-037-1

Band / Volume 252
Modellbasierte Spezifikationsmethodik zur effizienten Systementwicklung von Brennstoffzellenantrieben
R. Biurrun Sotelo (2015), 255 pp
ISBN: 978-3-95806-038-8

Band / Volume 253
Three-dimensional ray-tracing simulations of convective gravity waves
S. Kalisch (2015), iii, 183 pp
ISBN: 978-3-95806-040-1

Band / Volume 254
First-Principles Study on Pyrites and Marcasites for Photovoltaic Application
T. Schena (2015), 206 pp
ISBN: 978-3-95806-041-8

Band / Volume 255
Glass-Ceramic Sealant Reinforcement for High-Temperature Applications
B. Cela Greven (2015), xi, 119 pp
ISBN: 978-3-95806-042-5

Band / Volume 256
Entwicklung planarer $Ba_{0,5}Sr_{0,5}Co_{0,8}Fe_{0,2}O_{3-\delta}$-Membranmodule zur Sauerstoffabtrennung und Analyse ihres Transportverhaltens
P. Niehoff (2015), VIII, 134 pp
ISBN: 978-3-95806-044-9

Band / Volume 257
Extension of the Reactor Dynamics Code MGT-3D for Pebble-bed and Block-type High-Temperature-Reactors
D. Shi (2015), x, 162 pp
ISBN: 978-3-95806-045-6

Band / Volume 258
Failure Analysis of Thin Film Solar Modules using Lock-in Thermography
M. Siegloch (2015), XIII, 131 pp
ISBN: 978-3-95806-047-0

Band / Volume 259
Relation between growth rate, material quality, and device grade condition for intrinsic microcrystalline silicon:
From layer investigation to the application to thin-film tandem solar cells
S. Michard (2015), vi, 184 pp
ISBN: 978-3-95806-048-7

Band / Volume 260
Quantitative analysis of spatially resolved electroluminescence of Cu(In,Ga)Se_2 and a-Si:H thin-film solar cells and modules
T. Tran (2015), iii, 161 pp
ISBN: 978-3-95806-050-0

Band / Volume 261
Influence of the surface composition and morphology on the reflectivity of diagnostic mirrors in a fusion reactor
M. Matveeva (2015), 158 pp
ISBN: 978-3-95806-051-7

Weitere ***Schriften des Verlags im Forschungszentrum Jülich*** unter
http://wwwzb1.fz-juelich.de/verlagextern1/index.asp

Energie & Umwelt /
Energy & Environment
Band / Volume 261
ISBN 978-3-95806-051-7